MR-based Attenuation Correction for PET/MR Hybrid Imaging

MR-basierte Schwächungskorrektur für PET/MR Hybrid Bildgebung

Der Technischen Fakultät
der Friedrich-Alexander-Universität
Erlangen–Nürnberg

zur

Erlangung des Doktorgrades Dr.-Ing.

vorgelegt von

Bharath K. Navalpakkam

aus

Bangalore, Indien

Als Dissertation genehmigt
von der Technischen Fakultät
der Friedrich-Alexander-Universität Erlangen-Nürnberg

Tag der mündlichen Prüfung:	15.12.2016
Vorsitzende des Promotionsorgans:	Prof. Dr.-Ing. Reinhard Lerch
Gutachter:	Prof. Dr.-Ing. Joachim Hornegger
	Prof. Dr. rer. med. Harald H. Quick

Abstract

The recent and successful integration of positron emission tomography (PET) and magnetic resonance imaging (MRI) modalities in one device has gained wide attention. This new hybrid imaging modality now makes it possible to image the functional metabolism from PET in conjunction with MRI with its excellent soft tissue contrast. Besides providing specific anatomical detail, MRI also eliminates any ionizing radiation from eg. computed tomography (CT) examinations that is otherwise performed in standard PET/CT hybrid imaging systems. However, an unsolved problem is the question of how to correct for the PET attenuation in an PET/MR system. In this respect, the knowledge of the spatial distribution of linear attenuation coefficients (LAC) of the patient at the PET energy level of 511 keV is required. In standalone PET systems, transmission scans using radioactive sources were used for PET attenuation correction (AC) and if needed were scaled to the PET photon energy level. While in PET/CT systems, the CT information was scaled to PET energies for the same purpose. However, in PET/MR hybrid imaging systems, this approach is not feasible as MR and CT measure aspects of proton and electron densities respectively. Therefore alternate approaches to extract attenuation information have to be pursued. One such approach is to use MR information to estimate the distribution of attenuation coefficients within the imaging subject. This is done by using a simple limited class segmentation procedure to delineate air, soft tissue, fat and lung classes and subsequent assignment of their respective attenuation coefficients at PET energy of 511 keV. This way of generating attenuation maps (μ-maps) is however far from ideal as the most attenuating medium such as cortical bone is ignored. They are instead replaced by the attenuation coefficient of a soft tissue. While this approximation has been widely accepted for PET quantification in whole-body research, it has severe underestimation effects for brain studies.

In this thesis, we propose an improved MR-based μ-map generation approach. We demonstrate that dedicated MR sequences such as ultrashort echo time sequences (UTE) are useful for the purpose of attenuation correction. From a multitude of MR images, we generate μ-maps that include cortical bone and contain continuous Hounsfield units (HU) akin to a patient CT. These are then compared against segmentation based approaches. The efficacy of continuous valued μ-maps towards PET quantification is analyzed against different μ-maps such as patient CT, segmented patient CT with bone and segmented patient CT without bone. Results indicate that the proposed MR-based μ-maps provide a less than 5% error in PET quantification than any segmentation based μ-maps for brain studies.

Kurzfassung

Die kürzlich erfolgte Integration der Positronenemissionstomographie (PET) und Magnetresonanztomographie (MRT) in einem Gerät hat breite Aufmerksamkeit erregt. Durch das neu entstandene Hybridgerät ist es möglich den funktionellen Stoffwechsel, dargestellt durch die PET, in verbindung mit dem exzellenten Weichteilkontrast der MRT, abzubilden. Im Gegensatz zur Computertomographie (CT) ermöglicht die MRT die Darstellung von anatomischen Strukturen ohne zusätzliche ionisierende Strahlung. Dadurch ermöglicht die PET/MRT Untersuchungen mit signifikant reduzierter Strahlendosis im Vergleich zur PET/CT. Ein ungelöstes Problem ist jedoch wie die Schwächungskorrektur (AC) der PET in einem PET/MRT System realisiert wird. Grundsätzlich ist hierfür die Kenntnis der räumlichen Verteilung der linearen Abschwächungskoeffizienten (LAC) des Patienten bei Photonenenergien von 511 keV nötig. In Standalone-PET-Systemen werden hierfür Transmissionsaufnahmen mit radioaktiven Quellen eingesetzt, welche, falls nötig, auf die entsprechende Photonenenergie skaliert wurden. Analog dazu wird bei PET/CT-Systemen das CT als Quelle für die Transmissionsdaten genutzt. Auch hier werden die CT Aufnahmen auf die Photonenenergie der PET skaliert. Aufgrund der fehlenden Transmissionsdaten bei PET/MR Systemen ist dieser Ansatz jedoch nicht möglich, da, im Gegensatz zum CT, das Bildsignal hier durch die Protonen- und nicht durch die Elektronendichte bestimmt wird. Infolgedessen müssen für die Schwächungskorrektur beim PET/MRT alternative Ansätze geschaffen werden. Nach Möglichkeit sollten diese Ansätze nur Informationen der MRT benutzen um die Verteilung der Schwächungskoeffizienten innerhalb des abgebildeten Gegenstands zu schätzen. In der vorliegenden Arbeit stellen wir Methoden vor um aus MRT-Daten verbesserte Schwächungskarten zu extrahieren. Wir zeigen, dass dedizierte MRT-Sequenzen wie Ultra-Short Echo Time (UTE) Sequenzen hierfür wertvolle Zusatzinformationen liefern.

Auf Basis dieser und anderer Daten, stammend von Unterschiedlichen MRT-Sequenzen, generieren wir Karten mit kontinuierlichen Hounsfield-Einheiten. Da hier die kortikalen Knochen berücksichtigt sind, sind diese vergleichbar mit einem realen Patienten-CT. Die hierdurch erzeugten kontinuierlich-wertigen μ-maps vergleichen wir mit CT-generierten μ-maps und mit μ-maps aus segmentierten CTs mit und ohne Berücksichtigung der Knochen bezüglich der PET-Quantifizierungsgenauigkeit. Die Ergebnisse zeigen, dass die vorgeschlagenen MR-basierten μ-maps einen Fehler aufweisen, der weniger als 5% in der PET-Quantifizierung hat, im Vergleich zu allen andern segmentierungsbasierten μ-maps für Hirnstudien.

Acknowledgment

In the order of **mātā**, **pitā**, **guru** and **deivam** which in Sanskrit stands for mother, father, teacher and the almighty, I am indebted to my mother for her unconditional love, strength and patience and my father for his immense moral support throughout my life. Any attempt to describe the sacrifices they have made for my life, would only fall short of words. I thank my brother Sharath for the wonderful times we spent together in both Germany and USA and above all for having supported me all along. I am thankful to the almighty for instilling in me patience and courage during testing times.

Working in medical imaging, in particular nuclear imaging is a truly rewarding experience and each day has been a new learning experience. I sincerely would thank Prof. Dr.-Ing. Joachim Hornegger for opening up the possibility to work in this exciting field and for always encouraging me to push boundaries. A whole-hearted thanks to Prof. Dr. Harald H. Quick for welcoming me with open arms to conduct research at the Institute of Medical Physics, for his research support, supervision and for his openness towards new research ideas. I consider myself much fortunate to have been associated with the IMP and it was a sheer joy to have worked on the PET/MR scanner.

I am much indebted to Prof. Dr. Torsten Kuwert for his constant support. The insights he provided within the realm of nuclear imaging have been a great source of knowledge to me.

Many thanks to Prof. Dr.-Ing. Andreas Maier for proof reading my publications and for providing me with thought provoking ideas and comments. His encouragement towards research has been invaluable.

I had some wonderful colleagues with whom I shared great moments both on and off work. Many thanks to Harald Braun, Bassim Aklan, Daniel Paulus, Stefan Rietsch, Christopher Strohlein for the exciting kicker moments and for the amazing lunch time discussions. A special thanks to Michal Cachovan, Philipp Ritt and Susanne Ziegler for having proof read my thesis and for their valuable remarks.

I am grateful to the IMPRS for having funded me during the course of my doctoral studies. The IMPRS annual meetings were a refreshing experience that ensured both fun and scientific knowledge at some beautiful places in Germany.

I would like to thank my close acquaintances, Janani, Sami, Prasad, Archana, Darvesh, Azhar, Nitin and Verena for making Erlangen, a great place to stay.

- Bharath K. Navalpakkam

Contents

Chapter 1

Overview

1.1 Motivation

Nuclear imaging has made it possible to visualize vital functional processes in the human body. Through imaging modalities such as PET and single-photon emission computed tomography (SPECT) complex physiological (brain, heart etc.) and abnormal uptake sites such as cancer metastasis can be localized. Although rich in functional information PET/SPECT modalities lack anatomical detail. This gave birth to hybrid imaging systems wherein the anatomical information is borrowed from either CT or until recently MRI [Even 09], [Pich 08]. First PET/CT systems made its way into clinical routine in the early 2000 [Beye 00]. Due to the differences in duration of the imaging times, concerns in radiation doses, PET/CT hybrid imaging is performed only sequentially, with the CT examination being performed first followed by the long PET examination. However, in a CT examination a patient is subjected to a high energy X-ray ionizing radiation. In a view to therefore replace CT, MRI was seen as the modality of choice given the advantage of MRI to visualize soft tissue contrast by means of various image contrasts. Unlike in CT where external X-ray sources are required, MR visualizes aspects of proton densities of the imaging subject and does not therefore need ionizing radiation. However, integrating the PET detectors within an MR static magnetic field proved to be a challenge. Conventional photomultiplier tubes used in standard PET/CT were replaced by avalanche photo diodes (APDs), as the latter was found to be insensitive to the MR static magnetic field [Pich 08]. After overcoming these technical shortcomings, the first truly simultaneous PET/MR hybrid imaging scanners were introduced in 2010 [Quic 13].

On the software side, correcting for the effects due to PET photon attenuation in PET/MR hybrid imaging remains a challenging issue ever since. All the objects within the PET field-of-view (FOV) attenuate the 511 keV photons. These include hardware components used for MR signal transmission/reception, patient table, patient positioning aids as well as the human tissue. While the hardware elements are attenuation corrected using standard CT based templates with pre-defined table positions, deriving attenuation maps for human tissue from MR images is not so straightforward. This is because MR images do not contain electron density information but rather only proton densities. To circumvent this problem, the MR images are often segmented into tissue classes such as background, lung, soft tissue and fat to produce attenuation maps. Most importantly, the highly attenuating medium, cortical bone, is completely ignored due to the lack of any distinguishable information from standard MR sequences. Most clinical PET/MR systems has adopted this approach to perform PET attenuation correction. These will be referred to as product attenuation maps throughout the thesis.

Ultrashort echo time sequences have been successful in imaging tissues such as cortical bone with extremely short relaxation times. Much research has been dedicated to using UTE sequences for PET/MR attenuation correction. However, a main drawback with all of the aforementioned approaches is that image segmentation techniques are used to delineate cortical bone. As a result, a single linear attenuation coefficient (LAC) is assigned to cortical bone and other tissue classes. This method is inadequate since cortical bone is one of the highly attenuating mediums in the human body and has a wide range of densities. Therefore a single LAC would be insufficient to adequately represent it. In this thesis, this issue is addressed by means of pattern recognition techniques to model CT like attenuation maps.

1.2 Contribution to the Progress of Research

This research work proposes a novel framework for performing attenuation correction in hybrid PET/MR systems. The research objective is to achieve PET quantification improvement by means of correcting for attenuation using accurate attenuation maps. The framework itself uses tools such as image segmentation, image registration and pattern recognition algorithms. The following are the key contributions that are discussed in this research thesis:

1. **MR-based attenuation map generation:** Since in PET/MR imaging attenuation maps are required to correct for PET photon attenuation correction (PET-AC), there is a strong need for deriving attenuation maps from solely MR data. An inherent impediment to this is

that air and cortical bone share similar intensity characteristics in MR images, although they attenuate the PET photons differently. In this thesis, an algorithm pipeline is proposed that converts a set of MR images to CT-like volumes called pseudoCTs. These contain continuous HU and emulate the patient CT as closely as possible. In order to realize this, two dedicated MR sequences are used: an ultrashort echo time sequence for capturing cortical bone signal and a 3-D Dixon imaging sequence that provides water and fat information. Realistic pseudoCTs are generated by means of image segmentation and machine learning techniques.

2. **Evaluation of MR-based attenuation correction for brain imaging:** In the current clinical setting for PET/MR hybrid imaging, product generated attenuation maps that disregard cortical bone are routinely used for reconstructing PET images. We investigate the accuracy of MR generated pseudoCTs towards PET attenuation correction for patients that had no neurological clinical indication. These, when converted to PET photon energy level of 511 keV contain continuous valued LACs. The efficacy of the so derived attenuation maps is evaluated against the reference standard CT-based AC along with segmentation based attenuation maps. Results suggest the pseudoCTs with continuous LACs have the potential to estimate PET activities accurately with less than 5% error difference as against a 10%-15% difference for product based attenuation maps.

3. **Evaluation of MR-based attenuation correction on patients with fluorodeoxyglucose (^{18}F-FDG) hypometabolism:** In addition to healthy brain subjects, we extend the evaluation of the proposed MR-based pseudoCTs towards patients having a clinical question in the brain. For this purpose, patients that had ^{18}FDG-PET hypometabolism abnormalities and that had MR/PET and CT data sets were thus included in the study. PseudoCTs from MR data were generated for these patients and were compared against CT-based and product based MR-based AC (MRAC) methods. The proposed method outperformed the product based implementations and was able to achieve accurate PET quantification compared to patient CT based PET reconstructions.

The results of this thesis were published as a journal article [Nava 13c] and at the following conferences [Nava 12a], [Nava 13a], [Nava 12b] and[Nava 13b] [Nava 12c].

1.3 Thesis Organization

The thesis is structured in the following manner. Chapter 2 presents a background on the imaging techniques such as MR, PET and SPECT imaging and their respective underlying imaging physics. Since attenuation correction forms a key component of this research thesis, its principle and importance is discussed in depth. An introduction to PET/MR hybrid imaging, its technical shortcomings and solutions is presented together with an outlook on the existing problems in PET/MR attenuation correction.

Chapter 3 introduces a methodology for generating attenuation maps based on MR data alone and its extension to whole-body applications is discussed therein.

Chapter 4 presents an evaluation of the proposed MR-based attenuation correction for PET imaging. As reference standard, the CT-based attenuation correction is considered and the resulting differences are discussed in detail.

Chapter 5 discusses the impact of the current product attenuation correction method on patients that have a clinical significance in the brain regions. The PET quantification improvement achieved from the continuous valued MR-based attenuation maps is also investigated.

In the penultimate chapter, a conclusion of this research thesis is presented. In the final chapter, a discussion of future steps towards achieving accurate PET quantification in PET/MR hybrid imaging and possible extensions for MRAC are provided.

Chapter 2

Multimodality Imaging

2.1 Introduction

PET is an important and powerful tool to image bio-physiological processes in living species, most importantly in the human body. It has found wide applications related to the diagnosis of various tumors in nuclear medicine [Avri 00, Beet 94, Fisc 09, Grit 93, Ott 06]. In practice, the patients are injected with a radioactive bio-marker e.g. ^{18}F-fluorodeoxyglucose (^{18}F-FDG) that have an associated half-life time. In which case, during the waiting time of approximately one hour, the injected activity is allowed to metabolize. A radioactive decay process then takes place, where the unstable nuclei ionizes to yield positron, neutron and a neutrino. The positrons then annihilate with the surrounding electrons producing pairs of anti-parallel electromagnetic γ-photons in the process. These high energy photons are then detected by suitable PET detectors. The recorded events are later used for reconstructing the original 3-dimensional (3-D) activity source distribution. This forms the basis for PET imaging. However, an inherent problem of the non-attenuation corrected (NAC) 3-D image is that, they are often noisy and contain no accurate radiotracer quantification information. Hence, this poses a difficulty for a direct clinical interpretation. Therefore, NAC images need to be corrected for attenuation and scatter, besides other data corrections. The goal of this chapter is to provide an in-depth understanding into the process of attenuation correction, since it is a central part of this research endeavor. In the first and second sections, the physical principles behind photon attenuation correction are presented. We introduce commonly used nuclear imaging techniques and underline the importance of performing AC and further demonstrate how this improves image quality. In the third section and

fourth section, the MRI physics, different MRI sequences used in this thesis and an introduction to PET/MR hybrid imaging systems is presented.

2.2 Positron Emission Tomography

An unstable nucleus with excess protons undergoes a radioactive decay β^+ decay. Some of the positron-emitting radioactive isotopes used in PET are ^{18}F, ^{11}C, ^{13}N etc. An example of a β^+ decay is shown in Equation 2.1

$$^{18}F \rightarrow {}^{18}O + e^+ + \nu_e \tag{2.1}$$

Where, a positron e^+, neutrino ν_e and ^{18}O are produced from the disintegration of the ^{18}F radioisotope. The positively charged e^+ interacts with an electron e^- carrying a negative charge, to yield two opposite γ-photons with a total energy of 1022 keV (i.e. 511 keV for each photon). Figure 2.1 illustrates the process of annihilation and γ-photon generation. The emitted photons further interact with matter and result in scattered radiation. These interactions are mainly due to the Compton scattering phenomenon at 511 keV. Compton scattering occurs when the generated photons are deflected away from their original paths by the loosely bound outer electrons, thus causing them to loose either their original direction or energy or both. The effective energy of the photon after Compton scattering is given by Equation 2.2

$$E' = \frac{E}{1 + \frac{E(1-\cos\phi)}{m_e c^2}} \tag{2.2}$$

E represents the energy of the incident photon, E' the energy after interaction with the electron, $m_e = 9.11 \times 10^{-31}$ kg the mass of an electron and $c = 3.0 \times 10^8$ ms^{-1} and ϕ is the angle by which the photon is scattered. Compton scattering becomes predominant at energy levels exceeding 26 keV and is largely dependent on the electron density of the matter [Bush 02]. At lower energy levels in diagnostic imaging ($<$ 26 keV), photoelectric interactions gain dominance. These interactions occur when the incident photon interacts with orbital electron of an atom and ejects it from the atom. The kinetic energy of the ejected electron is the result of the incident photon energy minus the binding energy. The probability of such an occurrence is proportional to $\rho Z^3/E^3$, where Z is the atomic number, ρ is the mass density of the material in g/cm^3. At higher photon energy levels, Compton interactions are predominant especially in materials such as water, fat and soft tissue that

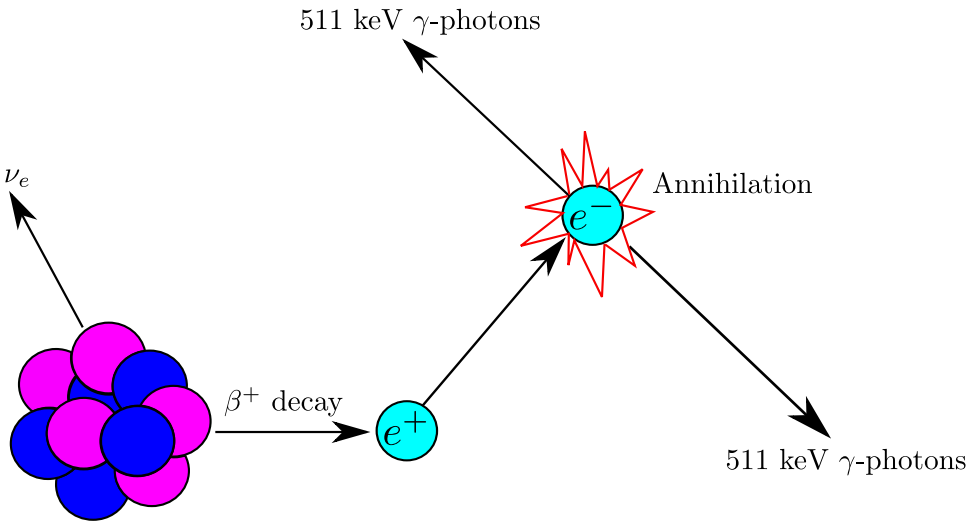

Figure 2.1: An illustration showing a positron-emitting radionuclide decaying to yield a positron e^+ and a neutrino ν_e. e^+ annihilates with an electron e^- to emit two anti-parallel γ-photons at 511 keV.

have a low Z. On the other hand, significant photoelectric interactions occur in materials with high Z at lower photon energies. Thus, both Compton and photoelectric interactions play an important role in diagnostic imaging and equally affect the extent of image contrast in both CT and PET imaging.

2.2.1 Attenuation Correction

In essence, a major contributor to photon attenuation in PET is the Compton scattering. The degree of such an attenuation for any non-uniform medium along a line of response (LOR) is defined in terms of an exponential function

$$I = I_0 e^{-\int_{\mathrm{LOR}} \mu(x)\mathrm{d}x} \tag{2.3}$$

Where, I_0 and I represent the incident photon intensities before and after interaction with the medium respectively, μ is the LAC of that medium given in cm^{-1}. The human body has varying ranges of μ value distribution. Table 2.1 enlists common tissue types along with their physical properties and LACs at 50 keV and 511 keV. The most attenuating medium in the human body is the cortical bone and therefore has the highest μ value of 0.1510 cm^{-1}. A simple calculation using Equation 2.3 tells us that the probability of photon scattering within 8 cm of soft-tissue (0.1000 cm^{-1}) in the human body is about 55%.

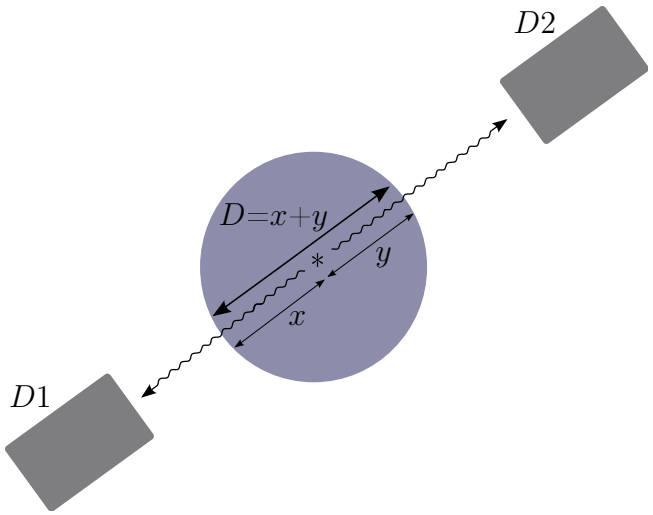

Figure 2.2: Detector pairs $D1$ and $D2$ recording an annihilation event occurred at source denoted by '*' within the object. The source is at a distance of x and y from detectors $D1$ and $D2$ respectively. The total photon attenuation along the LOR joining the two detectors is given by $I_0e^{-\mu x}{\cdot}e^{-\mu y} = I_0e^{-\mu(x+y)} = I_0e^{-\mu D}$. Thus, the count rates recorded between a detector pair for any LOR is independent of the exact event location along that LOR. This figure has been modified from [Cher 06].

Material[a]	Mass[a] density (g/cm^3)	Electron[a] density (electrons/cm^3)	μ@ 50[a] keV (cm^{-1})	μ@ 511[b] keV (cm^{-1})
Air	0.0013	3.80×10^{20}	0	0
Fat	0.91	3.04×10^{23}	0.1930	0.0854
Water	1.0	3.34×10^{23}	0.2140	0.1000
Bone	1.85	5.91×10^{23}	0.5730	0.1510

[a][Bush 02]
[b][Cata 10]

Table 2.1: Physical properties of different tissues and their linear attenuation coefficients at different photon energies. Photon attenuation increases with increase in the mass density of the material.

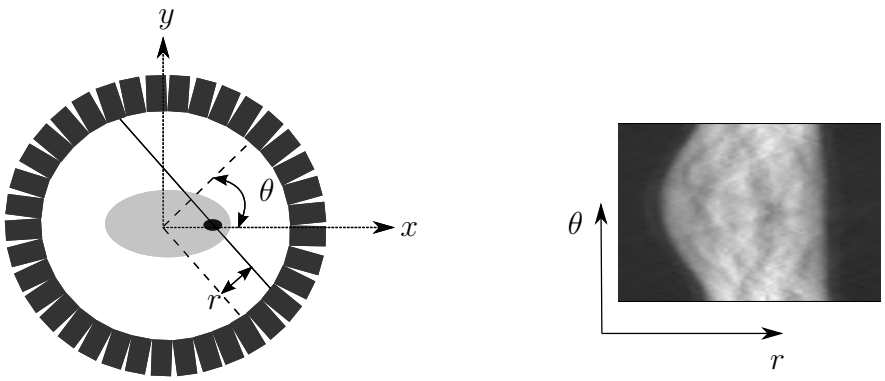

Figure 2.3: (a) Illustration of the conversion of the imaging object in cartesian (x, y) to polar co-ordinate system (r, θ), (b) example sinogram of a patient's head.

Also, another property of attenuation is illustrated in Figure 2.2. Here, it is evident that the total counts registered by a pair of detectors for any LOR depend only on the total distance traversed by the photons before reaching them. The goal here is to restore true counts along each LOR given the μ values for that LOR. The way to do this is by performing an attenuation correction. From Equation 2.3 we get

$$\frac{I_0}{I} = \frac{1}{e^{-\int_{\mathrm{LOR}} \mu(x)\mathrm{d}x}} \tag{2.4}$$

The attenuation is corrected for in each LOR using the precomputed μ values and the reciprocal of the Equation 2.4

$$\mathrm{ACF} = e^{\int_{\mathrm{LOR}} \mu(x)\mathrm{d}x} \tag{2.5}$$

$\frac{I_0}{I}$ is replaced by ACF which here stands for attenuation correction factor.

The counts recorded by the PET detectors are stored in a matrix format called sinogram, whose rows contain parallel projections of measured activities for a particular angle θ and whose columns represent radial distances r with respect to the center of scanner coordinate system. Figure 2.3 shows an example of recording and storing the data as sinograms. The relationship between the cartesian and polar coordinate system is given by Equation 2.6

$$r = x\cos\theta + y\sin\theta \tag{2.6}$$

Typically, for each LOR a corresponding ACF value is determined and this value is then multiplied with the corresponding sinogram for PET reconstruction.

As already pointed out earlier, the absence of adequate correction for photon attenuation would result in an incorrect estimation of PET activities. Consequently, this may hamper a clear clinical diagnosis due to regions in the body showing ambiguous increased or reduced PET activities. The importance of performing attenuation correction is therefore covered in the forthcoming section.

2.2.2 Effects of Attenuation Correction

When there is an absence of counts recorded across an LOR, then there is said to be an attenuation of the true PET signal. The resulting PET images without AC contain regions with spurious uptakes. This effect can be clearly appreciated from Figure 2.4 which shows two PET images-with and without AC of the National Electrical Manufacturers Association (NEMA) phantom filled with ^{18}F-fluorodeoxyglucose (^{18}F-FDG) [Karp 91]. Visually, the counts within the center of the phantom are lesser than at the periphery. This is because the photons at center undergo a greater attenuation than at the periphery. The same observation translates to human PET imaging as well. From Figure 2.5, it is evident that the brain and its surrounding regions are unlikely to represent true PET activities. The lungs which are a relatively less metabolically active site compared to the brain, show regionally increased uptakes in NAC images. Similar to the phantom periphery, the extremities exhibit a higher activity. This effect occurs because the photons on the periphery of the human body have to interact with less tissue before being recorded by the detectors. Likewise, the structures deep within the body would undergo more signal attenuation as the photons have to pass through more tissue layers indicating more tissue interactions. On the other hand, PET-AC images depict sharper contrast of uptake sites besides improving image contrast. Although, the necessity of performing AC has been rather debatable, several studies have suggested that PET-AC is necessary accurate tumor diagnosis and for a better enhancement of lesion-to-background contrast [Chan 01], [Hous 09], [Beng 97], [Bai 03].

2.2.3 Methods for Determining Attenuation Maps

The goal of any AC algorithm is to therefore accurately restore the true activity distribution of metabolically active structures especially tumors. In other words, an accurate distribution of μ-values at 511 keV of attenuating

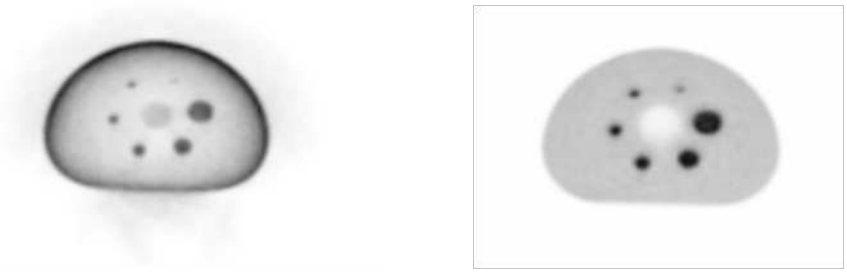

(a) (b)

Figure 2.4: PET images of a NEMA phantom filled with ^{18}F-FDG. (a) Example of NAC image. The periphery of the phantom shows erroneously high uptake values. This effect is mitigated in (b) and the "hot spots" show better contrast in the AC image.

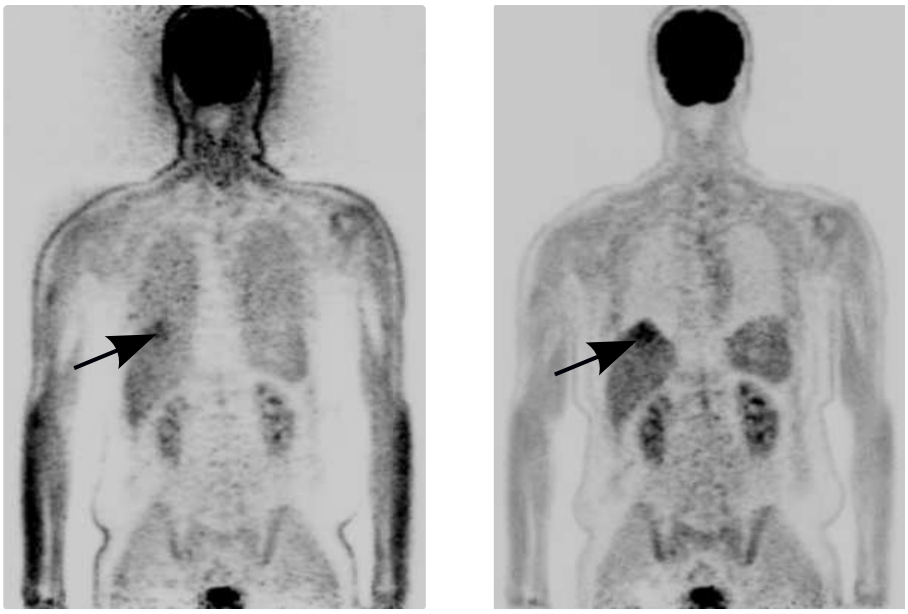

(a) (b)

Figure 2.5: Effect of performing AC. (a) Shows an example of a PET image of a patient that is not attenuation corrected. Lungs are seen to have faint increase in radioactivity and so do the extremities. A local hot spot (black arrows) in the liver region is smudged with reduced PET activity, while it appears to be prominent with restored PET activity in the corresponding attenuation corrected PET image (b).

structures such as patient positioning aids, hardware components and human tissues needs to be derived in order create a so-called μ-map. Several ways exist to determine μ-maps from various modalities. These are briefly discussed in this section.

Transmission Scans with External Sources

One of the earliest methods of deriving μ-maps in standalone PET scanners involved the use of externally rotating positron-emitting germanium-68 rod sources around a patient [Cher 06], [Naka 02], [Wu 04]. This was done in two steps:

1. Performing a "blank scan" with only the rod sources present to record I_0 photon flux
2. Transmission scan with the object present to measure I.

The ACFs were then calculated by dividing I_0 over I. The disadvantages of this approach were that it required lengthy acquisition times ranging from 20 min - 35 min and the μ-maps suffered from high statistical noise [Naka 02]. Also, ionizing radiation is used at the cost of little or no useful diagnostic information.

CT data

With the introduction of PET/CT systems, PET-AC was achieved using the CT information. Typically, a CT acquisition in a PET/CT system takes place at tube current of 165 mA, but a low-dose CT has also been investigated for AC purposes by lowering the tube current [Kame 02], [Wu 04]. In addition, CT offers high spatial resolution, relatively less scan time compared to germanium-68 based transmission scanning and most importantly yields lower statistical noise levels. Due to these reasons, μ-maps derived from CT in combined PET/CT systems are routinely used for AC. However, CT measures photon energies between 40 keV-140 keV while PET requires tissue attenuation coefficients at a much higher energy of 511 keV. This difference in energies is accounted for by using commonly used scaling procedures such as bilinear and hybrid scaling [Kina 03], [Burg 02].

MR based Image Segmentation

With the successful introduction of hybrid PET/MR systems, much research has been dedicated towards exploiting MR information for determining μ-maps. Because MR offers rich soft tissue information, it is an ideal modality

for hybrid imaging. However, since it measures proton densities and not tissue attenuation as it is done in CT imaging, converting MR images to μ-maps is non-trivial. Many groups use image segmentation techniques for this purpose. One of the earliest works involves the segmentation of segment T_1-weighted MR images into five different attenuating classes using a using fuzzy clustering technique [Zaid 03]. After segmentation, LAC values at 511 keV are assigned to their respective tissue classes. They are then fed into the pipeline for PET reconstruction.

A significant disadvantage with such approaches is that the cortical bone signal from standard T_1/T_2 based MR sequences is indistinguishable from air. The segmentation approaches therefore fail to adequately separate the two classes. A comprehensive overview of the state-of-the art algorithms is described in Chapter 3.

2.2.4 Event Types

Following an annihilation event, there can be four major event scenarios [Cher 06]. An illustration of these scenarios is shown in Figure 2.6.

- Random coincidences
- Multiple coincidences
- Scattered coincidences
- True coincidences

Random Coincidences

Annihilation events emit two anti-parallel photons simultaneously. The PET detectors should be able to correlate the two impinging photons as a coincidence event. The difference in the arrival times of these photons to still form a single coincidence event is called a timing resolution. A timing window is usually set to avoid any rejection of the produced photon-pairs from being recorded. Random coincidences are single events, where only one of the produced photons is recorded. More specifically, these events occurs when two photons originating from different annihilation sites are detected by different detectors. Therefore, these events do not contain valuable information regarding the PET tracer activities. The proportion of such events being recorded depends on the length of timing window required for the PET detectors. The longer the window, the higher is the chance of random coincidences to be recorded.

Multiple Coincidences

These scenarios occur when more than two PET detector cells participate in event detection. This makes it difficult to assign an LOR to these types of events. Therefore, multiple coincidences are normally discarded.

Scattered Coincidences

In this case, at least one of the two anti-parallel photons undergo a Compton type interaction with the medium before being recorded by the detectors. Due to this, the photon that undergoes an interaction changes it path and then impinges on a detector. As a result, the detected photon is mapped to an incorrect LOR. Such coincidences generally degrade the PET activities with the NAC PET image showing low image contrast. The degree of scattering depends also on the nature and depth of the interacting medium.

True Coincidences

In this event type, the photons escape through the object after an annihilation event. This is an ideal scenario, wherein the photons have not been scattered or have lost a part of their energies and are recorded by the PET detectors in coincidence at opposite ends.

2.2.5 PET Reconstruction

The objective of image reconstruction in PET is to recreate the distribution of positron-emitting sites within the imaging subject. In other words, the two-dimensional image $f(x, y)$ has to be recovered from the PET raw data stored in the form of a sinogram $s(r, \theta)$. There are two commonly followed approaches to perform this task.

1. Analytical reconstruction
2. Iterative reconstruction

Analytical reconstruction

In analytic reconstruction, filtered backprojection (FBP) is a commonly used technique. For the sake of simplicity lets assume a 2-D image $f(x, y)$ at hand. The set of projections $s(r, \theta)$ is obtained by integrating the activity distributions $f(x, y)$ across LORs. In 2-D, the transform that converts the image to sinogram $f(x, y) \rightarrow s(r, \theta)$ is called a Radon transform and is given by [Cher 06], [Wern 03]

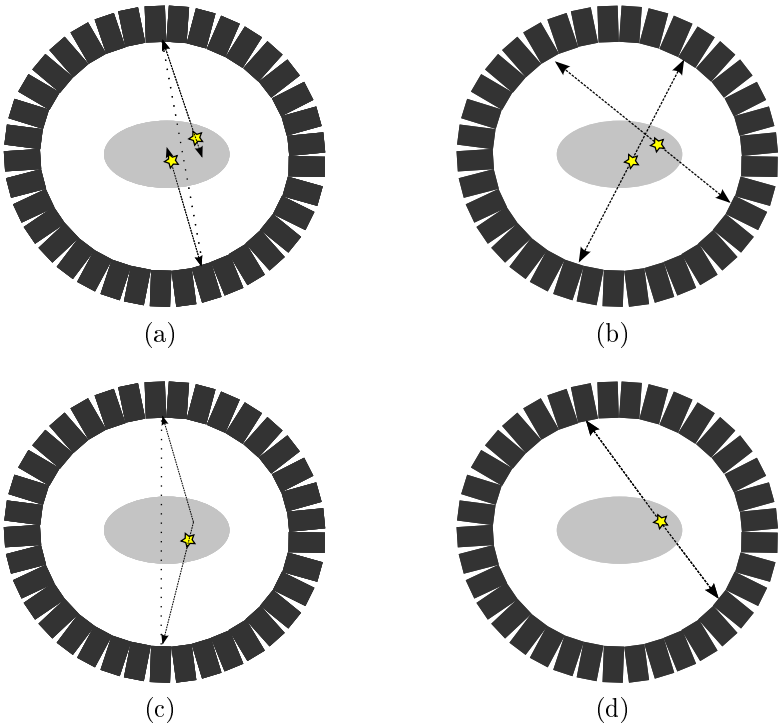

Figure 2.6: Types of events recorders by the PET detectors. (a) Random coincidence: photon detection from two different annihilation events, (b) multiple coincidence: simultaneous events are recorded, (c) scattered coincidence: photons interact with the object material and hence undergo Compton scattering before reaching the detectors and (d) true coincidence: the photons are detected from the annihilation event after they escape the object [Cher 06].

$$s(r,\theta) = \int_{-\infty}^{\infty}\int_{-\infty}^{\infty} f(x,y)\delta(x\cos\theta + y\sin\theta - r)\mathrm{d}x\mathrm{d}y \tag{2.7}$$

where δ is the Dirac delta function. Let the Fourier transform and its inverse operators be denoted as $\mathcal{F}$ and $\mathcal{F}^{-1}$. The 1-D Fourier transform is given by

$$P(\omega_r) = \mathcal{F}\{s(r)\} = \int_{-\infty}^{\infty} s(r)e^{-2\pi i\omega_r r}\mathrm{d}r \tag{2.8}$$

The image is reconstructed from its projections using the key property called the central-slice theorem. This states that the 1-D Fourier transform of sinogram data $s(r,\theta)$ for an angle θ is equivalent to a central slice of a 2-D Fourier transform of the actual image $f(x,y)$ evaluated at this angle. The image $f(x,y)$ is then reconstructed by simply taking the 1-D Fourier transform of all the rows in the sinogram data $s(r,\theta)$ followed by a 2-D inverse Fourier transform. We can deduce this property mathematically by substituting for Equation 2.7 in Equation 2.8 [Wern 03]

$$P(\omega_r,\theta) = \int_{-\infty}^{\infty}\left[\int_{-\infty}^{\infty}\int_{-\infty}^{\infty} f(x,y)\delta(x\cos\theta + y\sin\theta - r)\mathrm{d}x\mathrm{d}y\right] e^{-2\pi i\omega_r r}\mathrm{d}r \tag{2.9}$$

which after rearranging leads to

$$P(\omega_r,\theta) = \int_{-\infty}^{\infty}\int_{-\infty}^{\infty} f(x,y)\left[\int_{-\infty}^{\infty}\delta(x\cos\theta + y\sin\theta - r)\mathrm{e}^{-2\pi\mathrm{i}\omega_\mathrm{r}\mathrm{r}}\mathrm{d}\mathrm{r}\right]\mathrm{d}x\mathrm{d}y \tag{2.10}$$

Using the property of the Dirac delta functions, $\int_{-\infty}^{\infty}\delta(x-x_0)g(x)dx = g(x_0)$, the term within the square brackets simplifies to $e^{-2\pi i\omega_r(x\cos\theta + y\sin\theta)}$. On simplification we get

$$P(\omega_r,\theta) = \int_{-\infty}^{\infty}\left[\int_{-\infty}^{\infty} f(x,y)\mathrm{e}^{-2\pi\mathrm{i}\omega_\mathrm{r}(\mathrm{x}\cos\theta + \mathrm{y}\sin\theta)}\right]\mathrm{d}x\mathrm{d}y \tag{2.11}$$

Equation 2.11 now resembles the 2-D Fourier transform given by

$$\mathcal{F}(\omega_x,\omega_y) = \int_{-\infty}^{\infty}\int_{-\infty}^{\infty} f(x,y)e^{-2\pi i(x\omega_x + y\omega_y)}\mathrm{d}x\mathrm{d}y \tag{2.12}$$

Simplifying, Equation 2.11 yields

$$P(\omega_r,\theta) = \mathcal{F}(\omega_r\cos\theta, \omega_r\sin\theta) \tag{2.13}$$

which can also be written as

$$P(\omega_r, \theta) = \mathcal{F}(\omega_x, \omega_y)|_{\omega_x = \omega_r \cos\theta, \omega_y = \omega_r \sin\theta} \tag{2.14}$$

We started with the 1-D Fourier transform of the projection data at an angle and found it to be equal to a central slice of 2-D Fourier transform of the activity distribution at the same angle. Equation 2.14 hence substantiates the central-slice theorem. However, the image reconstructed via backprojection would appear blurred although the activity distribution would be visible. To counter this effect, a ramp filter is convolved with the projections in the Fourier domain prior to the backprojection step. Hence the name filtered backprojection. This operation, while enhancing the high frequency components also suppresses the low frequencies. Equation 2.15 refers to the sinogram after filtering $s'(r, \theta)$ by a ramp filter $H(\omega) = |\omega|$ in the frequency domain [Cher 06].

$$s'(r, \theta) = \frac{1}{2\pi} \mathcal{F}^{-1}\{\mathcal{F}\{s(r, \theta)\}|H(\omega)|\} \tag{2.15}$$

Essentially, the backprojection step is then given by the following relation

$$f(x, y) = \int_0^\pi s'(x\cos\theta + y\sin\theta, \theta)\mathrm{d}\theta \tag{2.16}$$

While the ramp filter mitigates the $1/r$ blurring effect, it amplifies the high frequency noise in the process. Therefore a so called the cut-off frequency ω_{cutoff} is defined at the maximum frequency $\omega_{max} = 0.5/\Delta r$, where Δr is the distance between the samples. Instead of a sharp drop off in case of a ramp signal at ω_{cutoff} other filters that possess a gradual drop off at $\omega_{cutoff} < \omega_{max}$ can also be used for effective noise filtering [Butt 30], [Shep 74]. This way a trade-off between the signal to noise ratio to the spatial resolution can be achieved by suitably setting the ω_{cutoff} of the filters.

While FBP based reconstructions have been routinely used for clinical interpretations, they suffer from significant noise levels. Besides, they fail to adequately model physical effects such attenuation and scatter. Iterative algorithms have been resorted for such cases which are known to reconstruct volumes with less statistical noise.

Iterative reconstruction

In iterative reconstructions, the basic idea is to determine an image that is as close as possible to the measured image under a set of constraints.

Maximum likelihood-Expectation Maximization (ML-EM) algorithms is one of the most commonly used methods for image reconstruction in emission tomography [Shep 82], [Lang 84]. The key idea here is as follows: An initial guess of an image is generated and is forward projected to obtain an observed projection estimate. This is then compared with the measured projections with the help of a metric. These error differences are computed using the corrected projection data and this update is backprojected to obtain a new iteration of the image. This process is continued in an iterative manner for a specified number of iterations or until convergence.

In general, the ML-EM approach finds applications in those cases that involve dealing with incomplete data. The problem in emission tomography is that the precise origin of the photon emission is unknown. The photon-counting and radioactive decay phenomenon may be modeled as a random process given by the Poisson distribution [Wern 03]. Equation 2.17 describes the iterative process using maximum-likelihood expectation maximization [Cher 06], [Ales 06]

$$f_j^{n+1} = \frac{\hat{f}_j^{\,n}}{\sum_{i'} H_{i'j}} \sum_i H_{ij} \frac{s_i}{\sum_k H_{ik} \hat{f}_k^n} \tag{2.17}$$

$\boldsymbol{f}^{n+1}$ is the image at $(n+1)^{\text{th}}$ iteration. $\boldsymbol{f}^n$ is the current estimated image at any iteration n. $\boldsymbol{H}$ is the system matrix and an element H_{ij} describes the probability that a detector bin i contains the emission data from a voxel j. As an initial estimate, a uniform value of voxel intensities is assigned to the starting image. This image is then forward projected into the projection domain by multiplying it with the system matrix. The measured projections s_i and estimated projections are compared via the division operator given by $\frac{s_i}{\sum_k H_{ik} \hat{f}_k^n}$ while the summation term over i backprojects the error estimates. These error estimates are used to update $\hat{f}_j^n$ followed by data normalization. This forms one iteration of a typical ML-EM reconstruction loop. After a specific number of iterations (20-50), an estimate of $\hat{\boldsymbol{f}}^{\boldsymbol{n}}$ close to true image is determined. In comparison to FBP reconstructions, iterative methods yield a multifold signal to noise ratio improvement as is shown in Figure 2.7. Low frequency components are generated in first few iterations followed by the high frequency counterparts. On the other hand, each iteration here require one full forward and backprojection. This renders the ML-EM reconstructions particularly time consuming compared to the FBP based approach. However, an accelerated implementation of the same involves estimating only a certain set of projections or subsets at every iteration and is therefore known as ordered subsets expectation maximization (OSEM) [Huds 94]. Currently, many clinical institutions use OSEM based reconstruction methods owing to

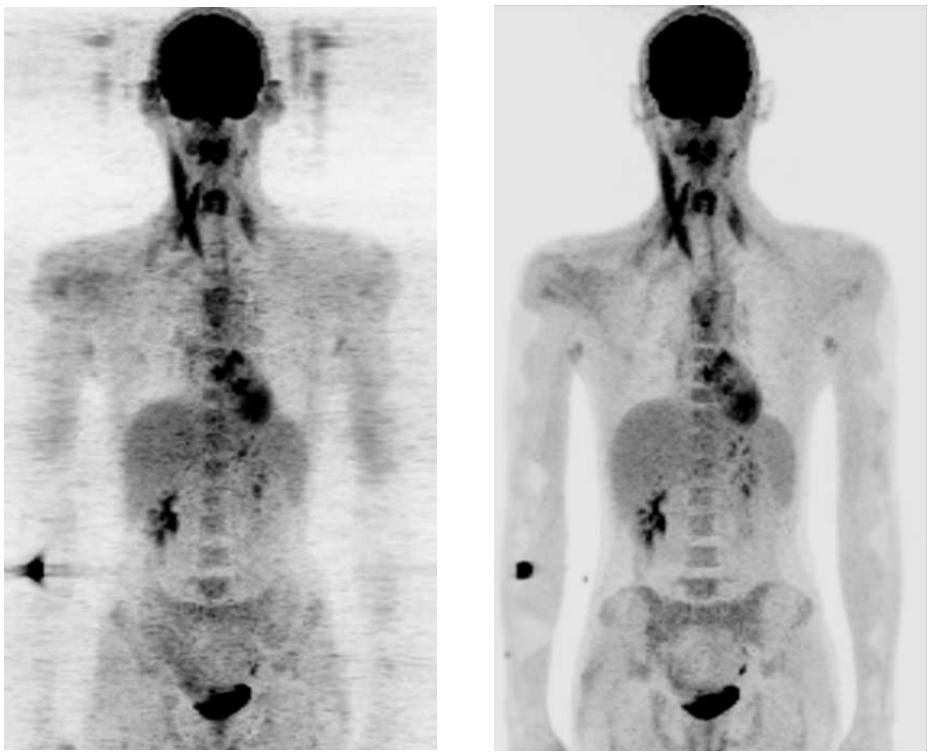

(a) (b)

Figure 2.7: Maximum intensity projection of FBP based PET reconstruction (a) and an iterative reconstruction (b). Note the significant improvement of image quality in iterative over standard FBP based reconstructions.

the introduction of many memory efficient architectures such as graphical processing units (GPU). The drawback of OSEM is that it is unknown after how many iterations the image has converged. For a detailed explanation on iterative reconstruction methods in emission tomography the reader is referred to [Wern 03].

2.3 Magnetic Resonance Imaging

The objective of this section is to introduce the working principle of MRI imaging and the different image contrasts that can be obtained. While acknowledging the usefulness of such MR images for many clinical applications, the lack of sufficient cortical bone signal from standard MR imaging sequences is highlighted. Against this disadvantage, a dedicated sequence with a shorter echo time suitable for imaging cortical bone is presented to-

gether with a discussion of its underlying physics. While only the basics of MRI are presented here, in depth understanding on the same can be found in [Brow 03].

MRI technique works on the principle of measuring proton densities within the imaging object. A major constituent of the human body is water. These molecules are proton rich and each proton carries a positive charge and an associated spin. The spins being magnetic in nature can be attributed with a magnetic moment $\boldsymbol{\mu}_m$ and are influenced by magnetic fields. In the absence of any external magnetic field ($\boldsymbol{B_0}$), these protons are oriented in a random manner and hence their magnetic moments nullify each other leading to a zero net magnetization $\boldsymbol{M}$. However, the situation is different when an external magnetic field is introduced. A fraction of the spins now orient themselves along $\boldsymbol{B_0}$ while the remaining precess in an anti-parallel direction. Figure 2.9 shows the illustration of a proton precessing around the static magnetic field $\boldsymbol{B_0}$. With the external magnetic field, the spins are now in a state of equilibrium. The net effect is that there exist more spins aligned in the direction of $\boldsymbol{B_0}$ than those that are away from it. This results in a net magnetization vector $\boldsymbol{M}$ which depends on the strength of $\boldsymbol{B_0}$ field. The frequency with which the spins precess about $\boldsymbol{B_0}$ is called Larmor frequency. This can be described by the relation

$$\omega_0 = \gamma ||\boldsymbol{B_0}|| \tag{2.18}$$

Here, ω_o is the Larmor frequency and γ is the gyromagnetic ratio for the specific nuclei. For Hydrogen protons ω_0 is equivalent to 42 MHz at $\boldsymbol{B}_0 = 1$T. It is evident from this relation that the Larmor frequency increases linearly with higher B_0 values. Figure 2.8 shows the illustration of spins from a voxel within the patient prior to and after the application of the $\boldsymbol{B_0}$ magnetic field.

In order to perturb the spins precessing in their equilibrium state, an electromagnetic radio frequency pulse (RF pulse) is applied at the resonant frequency which is the Larmor frequency. The extent to which the spins are disoriented away from the $\boldsymbol{B_0}$ axis is defined by the flip angle α. Figure 2.10 shows the effects of spin precession before and after the application of an RF pulse. For example, a 90° RF pulse would flip the spins in the x-y transverse plane. Likewise, the spins would precess in the negative z direction after applying a 180° RF pulse. These spins emit the absorbed energy through a process called relaxation to reach an equilibrium state. Depending on the nature of relaxation (longitudinal or transverse) of different tissue types, different image contrasts are obtained. This is elaborated in the forthcoming section.

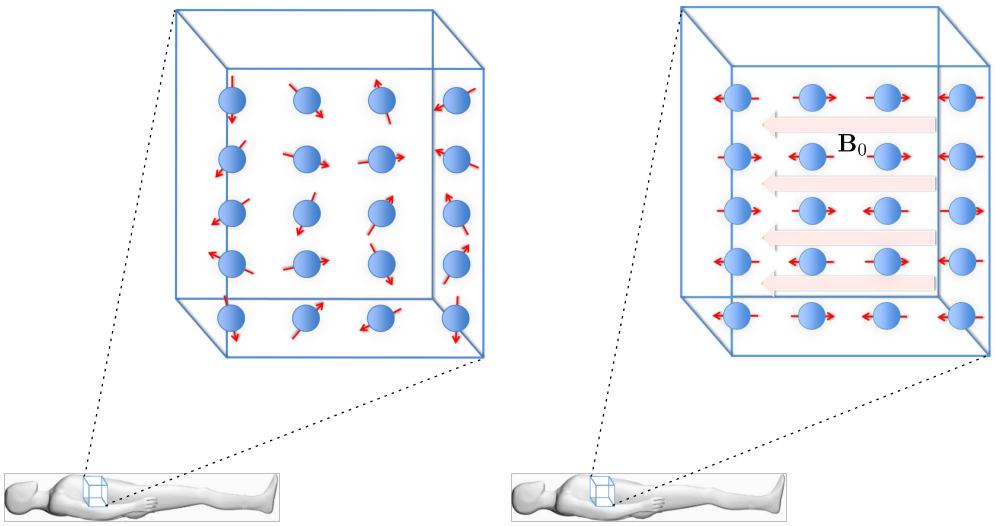

Figure 2.8: (a) Spins oriented in a random manner prior and (b) after the application of the static magnetic field $\boldsymbol{B_0}$.

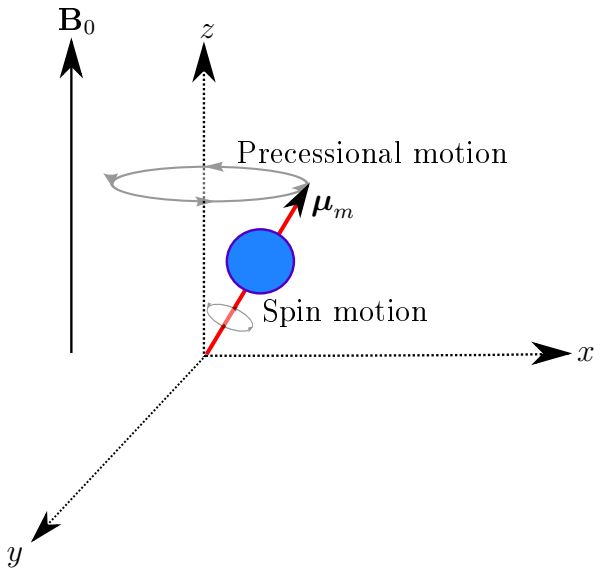

Figure 2.9: Example of a spin with magnetic moment $\boldsymbol{\mu}_m$ exhibiting both precessional and spin motions in the presence of the static magnetic field $\boldsymbol{B_0}$.

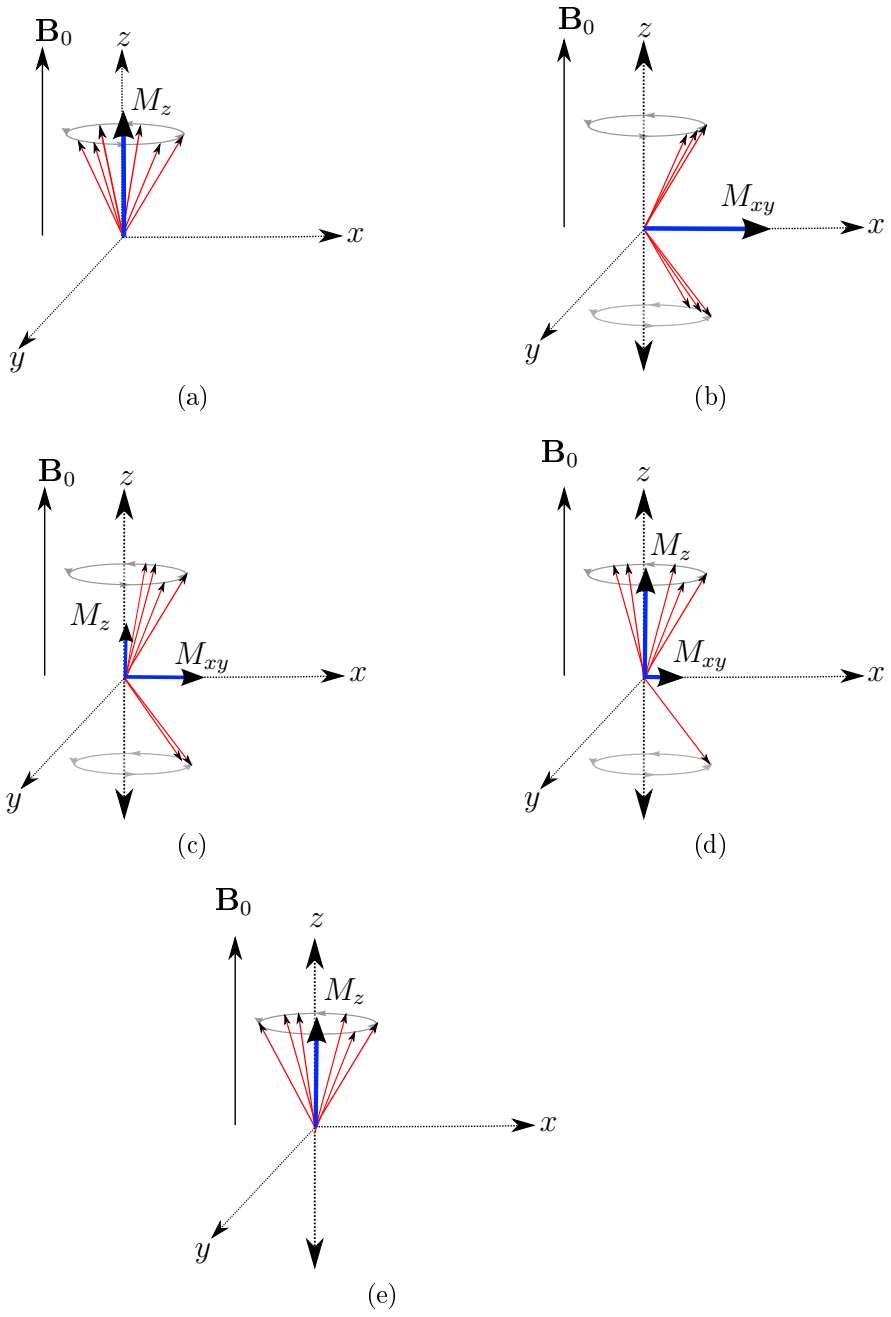

Figure 2.10: Magnetic spin characteristics before and after the application of a 90° RF pulse. (a) Magnetic spins precessing around the z axis before the RF pulse, causing the longitudinal magnetization M_z to remain dominant. (b) Spins precessing perpendicular to the z axis after the application of the RF pulse. Since the spins are flipped to the x-y plane, a growth of transversal magnetization M_{xy} occurs while the longitudinal magnetization M_z disappears. (c) and (d) show step by step processes wherein the spins loose their phase coherence and the energy acquired from the RF pulse and try to return to a state of equilibrium. This causes a regrowth M_z and an exponential decrease of M_{xy}. In (e) all the spins are completely out of phase and a full restoration of M_z occurs.

2.3.1 Longitudinal Magnetization

Once the 90° RF pulse is applied, the net magnetization vector $\boldsymbol{M}$ would be in a non-equilibrium state. The magnitudes of their components along x, y and z directions are denoted as M_x, M_y and M_z. The RF pulse flips the spins in the transverse spins x-y plane. At this stage, the spins possess what is known as the transverse magnetization M_{xy} which is the resultant of M_x and M_y. However, they quickly loose this transverse magnetization and slowly recover the longitudinal magnetization M_z. Both these processes are independent and are exponential in nature. The time taken for the collective spins longitudinal M_z component to recover 63% of the original magnetization is called a T_1 relaxation. This is described using the relation

$$M_z(t) = M_z(0)(1 - e^{-\frac{t}{T_1}}) \tag{2.19}$$

where $M_z(0)$ is the magnetization at time $t = 0$. This denotes a state of equilibrium where $\boldsymbol{M}$ is oriented towards z axis and $M_z = M_0$ and $M_{xy} = 0$. t is the time elapsed since the application of the RF pulse. Figure 2.11 shows the exponential nature of the longitudinal relaxation and the behavior of the spins prior to and after the RF pulse. Depending on the state of matter, the protons are packed by the neighboring atoms in a particular arrangement that make up a lattice. The absorbed RF energy by the spins is dissipated to this lattice through intra-molecular interactions. Hence, the energy transfer process is also known as a spin-lattice relaxation. T_1 is dependent on the rate at which proton spins of different tissue types within the human body transfer the RF energy to the lattice. This is in turn governed by the molecular structure and its mobility and in particular how the protons are bound to the molecules. For example, in case of free water, the protons have increased mobility since they are not bound to any macromolecules (lipids). The protons would therefore experience rapidly changing magnetic fields which cover a broad spectrum that includes both low and high frequencies. For an energy transfer to take place, there must exist a spectral overlap between the tumbling frequency and the Larmor frequency. In the case of free water, this overlap is minimal which means the materials with an amorphous form (Cerebrospinal fluid (CSF)) would exhibit a long T_1. On the other hand, fat and muscle tissues are intermediate in size and possess a considerable spectral overlap relative to the Larmor frequency. Hence, conducive for energy transfer, these materials exhibit short T_1. Slowly moving molecules contain less spectral overlap relative to Larmor frequency and thus contain a long T_1. This forms the source of T_1 contrast in MRI imaging. Since, the Larmor frequency is directly proportional to the field strength B_0 (Equation 2.18) and since the spectral overlap of the tumbling frequencies depend on the Larmor

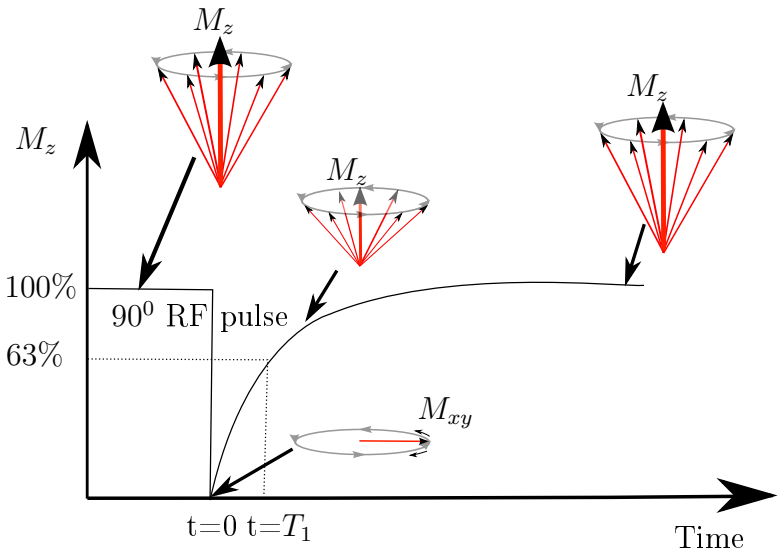

Figure 2.11: An illustration of a longitudinal relaxation process. Before the RF pulse, the longitudinal is at its maximum value where $M_z = M_0$. After the RF pulse at $t = 0$, all the spins are flipped to the $x - y$ plane where the spins are in phase coherence with each other making $M_z = 0$. Progressively, the spins dissipate their RF energy to the lattice in order to attain a state of equilibrium that causes a recovery of M_z. Image adapted from [Bush 02].

frequency, T_1 is said to be field dependent. Due to the reasons stated above, CSF appears dark while fat, muscle, white and gray matter are have elevated intensities. Table 2.2 enlists the T_1 times for common tissue types [Bott 84].

2.3.2 Transverse Magnetization

Immediately, after a 90° RF pulse has been applied, the spins precess in phase in the x-y plane. At this point, the phase coherence between the individual spins begins to fall apart and ultimately a stage is reached where all spins are out of phase with each other. This process is illustrated in Figure 2.10. A decay of the MR signal exists, which is exponential in nature and is called *free induction decay* (FID). The precessing magnetization in the transverse plane induces a current in the receiver coil placed perpendicular to the $\boldsymbol{B_0}$ magnetic field and this forms the source for the MR signal reception. The time it takes for the spins to loose its phase coherence to 37% of its original value is termed as the T_2 relaxation time. This is given by the relation

$$M_{xy}(t) = M_{xy}(0)e^{-\frac{t}{T_{2^*}}} \tag{2.20}$$

Tissues	1 Tesla	1.5 Tesla
Fat	240	260
Muscle	730	863
Gray Matter	809	917
CSF	2500	3000
White Matter	680	783

Table 2.2: T_1 constants given in ms [Bott 84].

Tissues	T_2 constants (ms)
Fat	84
Muscle	47
Gray Matter	101
CSF	1400
White Matter	92

Table 2.3: Field independent T_2 relaxation times for different tissues. [Bott 84].

Figure 2.12 shows the transverse relaxation process. The spin dephasing occurs due to extrinsic and intrinsic magnetic field inhomogeneities. Extrinsic inhomogeneities are related to the non-uniformity in the static magnetic field whereas the intrinsic inhomogeneities are due to locally varying magnetic fields experienced by the spins. Both of them contribute to spins dephasing due to spin-spin interactions. T_2 relaxation occurs when effects due to the extrinsic magnetic field inhomogeneities are neglected. However, the effective measured decay occurs at a much faster rate of T_2^* rather than T_2 due to both the extrinsic and intrinsic field inhomogeneities effects combined ($T_2 > T_2^*$). Depending on how fast the spins of tissues dephase, different tissues tend to exhibit varying T_2 relaxation times. Smaller molecules with wide range of tumbling frequencies undergo minimal spin-spin interactions and hence they possess a long T_2 relaxation. Larger, slow moving molecules such as cortical bone has hydrogen molecules bound to macromolecules and thus have a structured form. The protons in the bounding layers (also called hydration layers) influence enhanced interactions with neighboring proton spins. This results is a faster decay of the T_2 signal in cortical bone like tissue types. For the same reason, tissues such as fat and muscle have a short T_2 as compared to water-laden CSF. Table 2.3 shows the T_2 relaxation times for different tissue types.

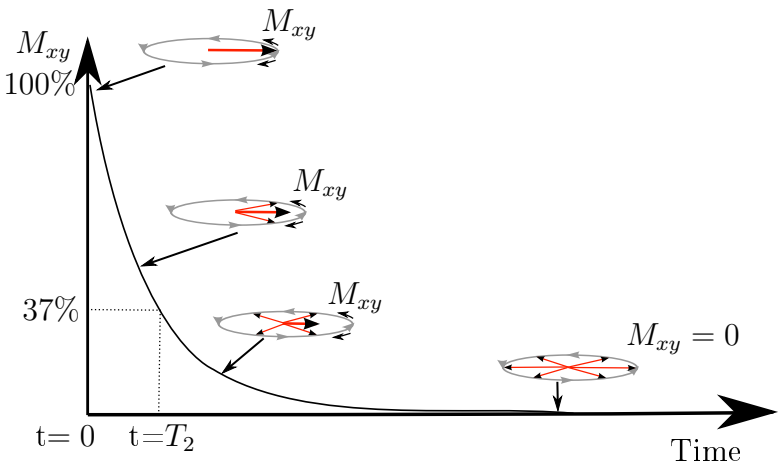

Figure 2.12: An illustration of transverse relaxation process. At $t = 0$, M_{xy} is at its maximum. Spins loose their phase coherence with time due to spin-spin interactions and this results to a loss of transverse magnetization. Image adapted from [Bush 02].

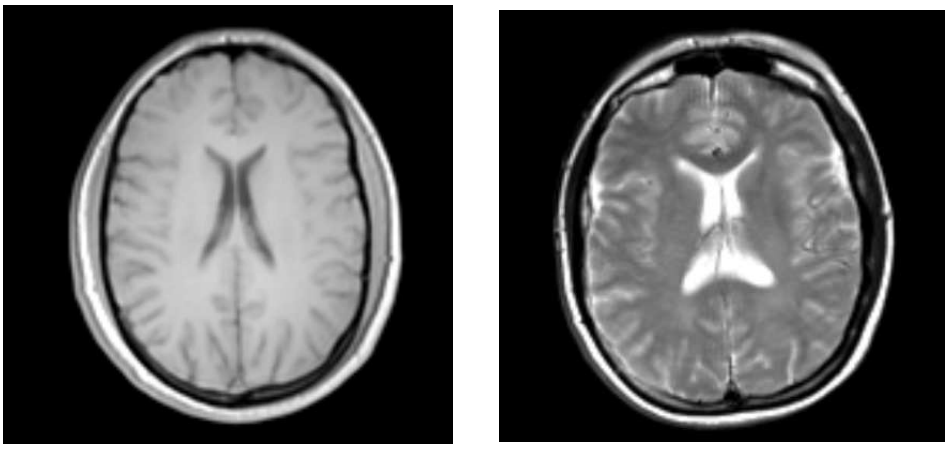

(a) (b)

Figure 2.13: Exemplar brain slices of a (left) T_1-weighted and (right) T_2-weighted sequence. The CSF regions are brighter in T_2-weighted than in T_1-weighted sequence.

2.3.3 Spatial Encoding

The FID is the source for an MRI signal reception. To be able to reconstruct an image out of the FID, the spatial location of the spins at every voxel needs to be determined. This is achieved by using gradient coils in x, y, z directions. They are basically coils that induce magnetic fields in a linear gradient fashion in all the three directions. The gradient field now is superimposed on the $\boldsymbol{B_0}$ field. Following Equation 2.18 and depending on the gradient amplitude a change in the frequency results. For example, for a patient lying in a head first-supine position, a slice selection gradient G_{S} in the z direction is switched on. An RF pulse with a bandwidth of frequencies $\Delta\omega$ resonates and excites all the spins for a particular slice in the x -y plane, along the applied gradient. Its slice thickness t can be determined by the relation

$$\Delta\omega = \gamma(t \cdot G_{\mathrm{S}}) \tag{2.21}$$

Thus, for a fixed $\Delta\omega$, a larger slice thickness requires a smaller gradient field G_{S} and vice-versa. Excitation of different spatial locations is achieved by varying the central frequencies of $\Delta\omega$. The gradient field is given in millitesla per meter (mTm^{-1}).

The next step is to perform a frequency encoding. Assume that a slice z_0 has been excited with a 90° RF pulse. The spins precessing with a frequency ω_0 experience a transverse relaxation process. A 180° refocusing pulse is then applied to bring the dephasing spins into phase coherence again. A readout gradient G_{R} in the x direction is turned on during the MR signal acquisition. The spins now precess with different frequencies in the x direction depending on the spatial location. The magnetic field strength is altered accordingly and is given by

$$B_{\mathrm{x}}(x) = ||\boldsymbol{B_0}|| + G_{\mathrm{R}}x \tag{2.22}$$

Knowing two out of three co-ordinates for MR signal detection, the last step is the phase encoding. A gradient G_{R} in the y direction is switched on. The spins that were precessing with a certain frequency ω_0 prior to the application of the phase encoding gradient, now precess with higher and lower frequencies depending upon the gradient strength along that slice. Once the y gradient field is switched off, the spins revert to their original frequencies but there exist differences in their respective phases. For a fixed G_{P} and depending on the spatial location in the phase encoding direction, different spins possess different phases. The signal produced thus forms one line of the so-called k-space. Typically, the k-space is a $N_{\mathrm{p}} \times N_{\mathrm{R}}$ sized matrix that contains both phase and frequency information. N_{P} represents the number

of phase encoding steps while N_{R} represents the samples acquired during frequency encoding. The center of k-space contains the low frequency information of the MR image while the regions away from it predominantly represent edge information. A 2-D Fourier transform is then used to recover an MR image from the acquired k-space data.

2.3.4 Standard MR Sequences

The spin echo (SE) and gradient echo (GRE) sequences are two of the most commonly used MR sequences in clinical practice. In this section, a review of their physical principles is presented. Also, various ways of obtaining a plethora of image contrasts by modifying MR acquisition parameters is highlighted.

Spin Echo Sequence

An application of a 90° RF pulse flips the spins in the transverse x-y plane. They now start to dephase slowly in the clockwise direction. At this point, at time τ after the 90° pulse, a 180° refocusing pulse returns the spins to a state of phase coherence. This forms the basis for a spin echo signal. After 2τ, the signal reaches its maximum and thus forms one echo time (TE). Similarly, many such spin echoes may be applied in succession to yield a multi-echo sequence. The echoes can be generated several times before the transverse magnetization is completely lost. The time difference between two consecutive 90° RF pulses is called the repetition time (TR). The T_2-turbo spin echo sequence (T_2-TSE) is based on this principle. A plethora of imaging contrasts can be obtained with SE sequences. Depending on the dominance of either T_1 or T_2 relaxation characteristics, images so obtained are either termed as T_1 -weighted or T_2 -weighted images. Such contrasts are generated by suitably altering both the TE and TR parameters. For example, the CSF mostly composed of water has a long T_1 (Table 2.2) and long T_2 (Table 2.3). At a short TR, only a small portion of CSF would have M_z recovered, in contrast to a larger recovery of M_z for fat and grey matter tissues. This means that a 90° RF pulse would flip only a fraction of the CSF spins that regained M_z previously to the x-y plane. Since a small fraction of the flipped spins participate in transverse relaxation process, CSF appears dark in a T_1 -weighted image. Since a majority of spins from fat and grey matter (GM) undergo substantial T_1 relaxation, they appear with relatively enhanced intensities. Therefore, by combining a short TE and a short TR, a predominantly T_1 contrast is obtained. Figure 2.13a shows an example of a T_1 -weighted image. To obtain a T_2 -weighted contrast a longer TR and a

longer TE is used. In case of a long TR, most tissues would have undergone complete T_1 relaxation. Therefore, for a long TE only the CSF tissues would have a phase coherence left, with other tissues being completely dephased. In such a case, the T_2 relaxation becomes predominant and thus the CSF would appear brighter than the other tissue types. This gives a T_2 -weighted contrast. Figure 2.13b shows a T_2 -weighted image.

A long TR and a short TE is used to obtain proton density (PD) -weighted images. At a long TR, most of the tissues would have recovered substantial M_z and the effects due to T_1 relaxation is considerably reduced. At a short TE, most spins would not have dephased as well. This sequence thus measures the net magnetized protons present in the tissues. In PD -weighted images CSF occurs brighter than fat or GM. Thus, different image contrasts are obtained by altering TE and TR values using a SE sequence. Inherently, in a SE sequence on the application of the spin echo, the spins are inverted. This negates the effects due to the extrinsic magnetic inhomogeneities due to the static magnetic field. The sampled FID is thus T_2 instead of T_2^*.

However, due to the trains of echo that need to applied, the SE sequences generally require larger TRs and thus demand larger acquisition times. A pulse sequence diagram depicting the SE sequence is illustrated in Figure 2.14 and an illustration of process of echo formation is shown in Figure 2.15.

Gradient Echo Sequence

In gradient echo sequences (GRE), the gradients with negative and positive polarity play the role of dephasing and rephasing the spins, respectively. Markedly, there are no 180° refocusing RF pulses as in a SE sequence. After the negative and positive gradient reversals, no change in spin direction takes place. Instead, the spins dephase and rephase in the same direction as before. This also means that GRE sequence is not immune to extrinsic magnetic field inhomogeneities but is rather sensitive to it. As a result, the FID sampled with a GRE sequence would decay much quicker at the rate of T_2^* and not at T_2 as in a SE sequence. One way of obtaining various image contrasts through a GRE sequence is by varying the flip angles. Also, lengthy acquisition times can be avoided by selecting low flip angles and smaller repetition times. Typically with a GRE sequence flip angles in the range of 1° to 60° can be realized. Figure 2.16 shows the pulse sequence diagram for the GRE sequence. The sequence of spin characteristics and the echo generation in a GRE sequence is shown in the Figure 2.17.

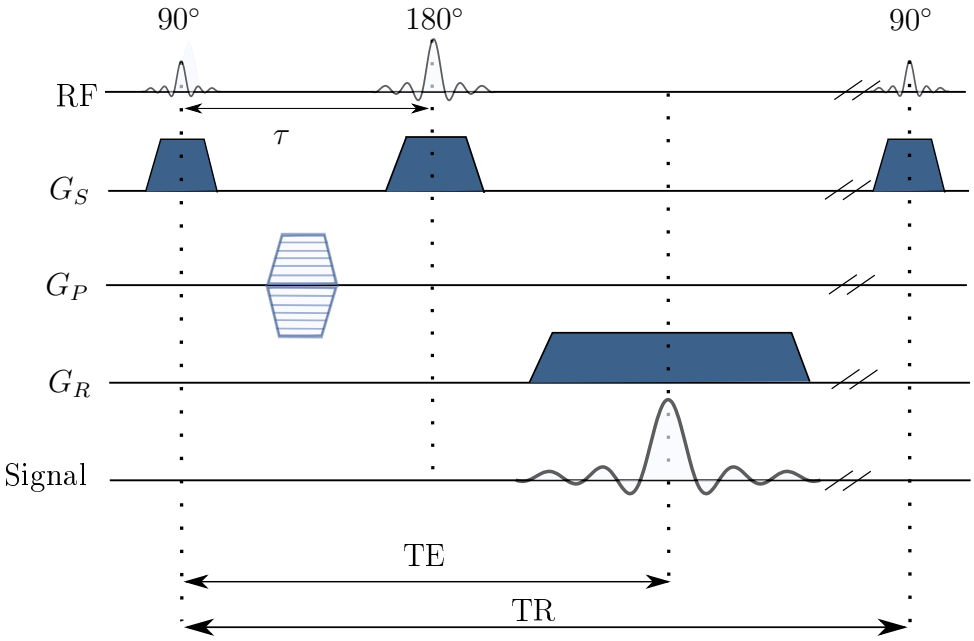

Figure 2.14: Spin echo sequence diagram. Following the 90° RF pulse, a 180° spin echo brings the spins in phase. G_s encodes the z direction and represents the slice selection gradient. G_P is known as the phase encoding and it encodes the y direction while G_R, the read out gradient encodes the x direction. TE stands for echo time and TR is the repetition time.

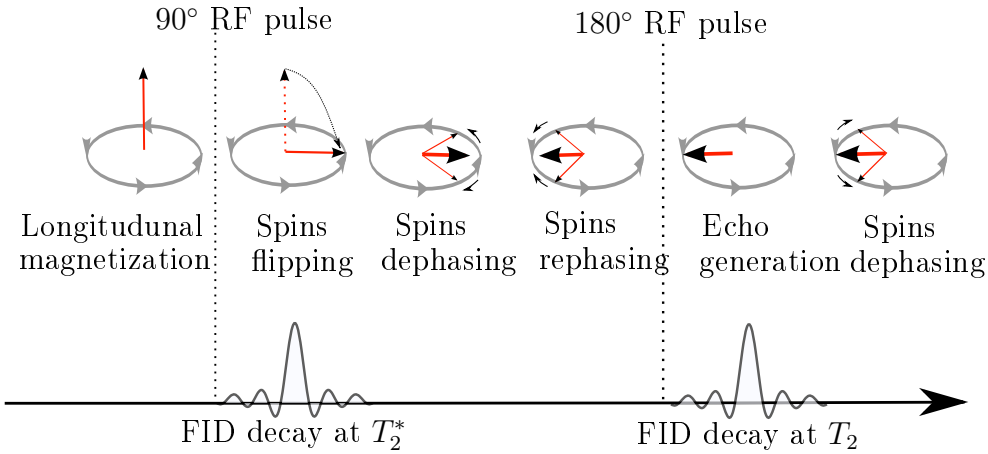

Figure 2.15: Illustration of the spin behavior and echo generation in a spin echo sequence. Prior to the 90° RF pulse longitudinal magnetization is dominant. The spins that are flipped after the 90° RF pulse begin that dephase at the rate of T_2^*. A 180° RF pulse then inverts the spins where they start to rephase to generate an echo. The echo decays at the rate of T_2 [Bush 02].

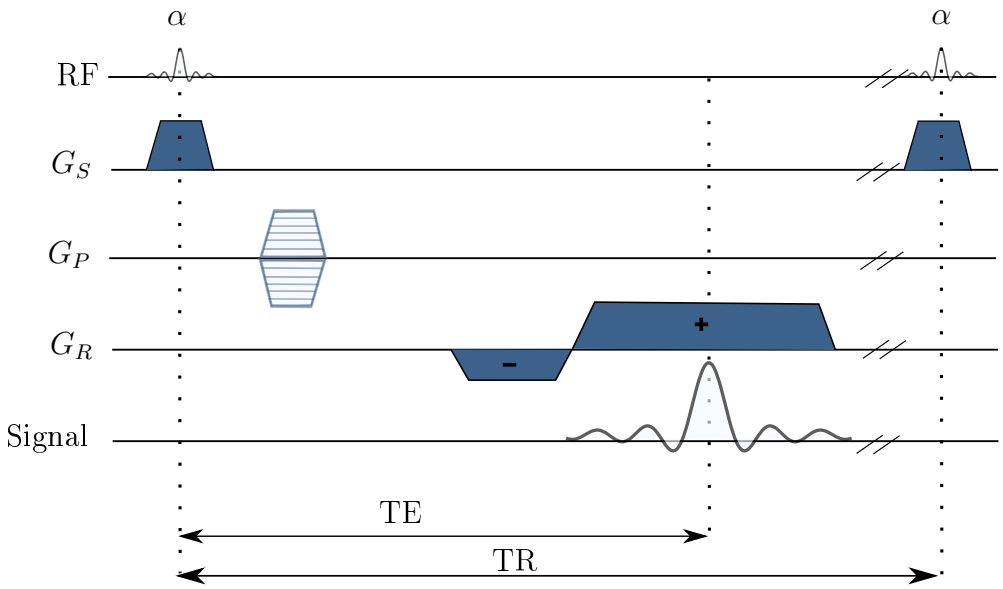

Figure 2.16: Gradient echo sequence diagram. The reversal in the gradient polarity is responsible for refocusing spins in the transverse plane. G_s represents slice selection gradient and G_P, G_R represent phase encoding and read out gradients respectively. α denotes the flip angle. TE stands for echo time and TR is the repetition time. Note the absence of 180° refocusing RF pulse.

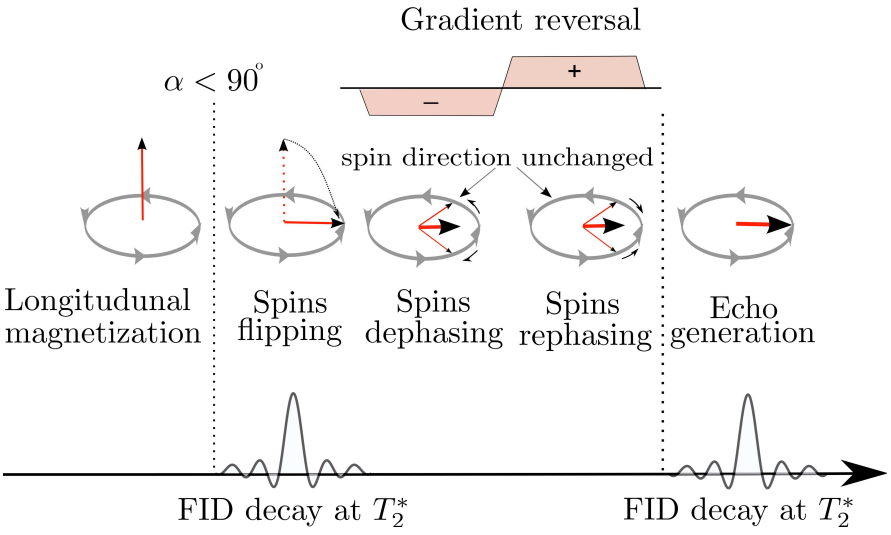

Figure 2.17: Illustration of the spin behavior and echo generation in a gradient echo sequence. The spins that are flipped to the x-y plane after an initial RF pulse with a flip angle α. A gradient with a negative polarity further dephases the spins. A positive gradient rephases the spins to generate a gradient echo signal. Note that unlike in a SE sequence, no change in the direction of the spins occurs. The FID decays at the rate of T_2^* [Bush 02].

2.3.5 Ultrashort Echo Time Sequences

In the previous section, conventional MR sequences such as the SE and the GRE sequences were discussed. However, they are inadequate to image cortical bone which forms an important attenuating class for PET-AC. The differences between the UTE and conventional SE or GRE sequence is highlighted in this section. UTE is a specialized sequence with TEs in the range of 0.05 ms-0.20 ms and is thus capable of capturing cortical bone signal that has a short T_2 of 0.42 ms-0.50 ms [Robs 03]. UTE echo times are about 20 times much shorter than those used in conventional MR sequences.

The source of the short T_2 in cortical bone is predominately due to collagen fibres [Robs 03]. Apart from cortical bone, these molecules are found in tendons, ligaments and cartilages. Typically in rigid structures such as in cortical bone, the transverse T_2 relaxation happens quickly, due to its compact structure. This situation is different in water wherein the protons are loosely bound and thus minimal spin-spin relaxation causes a long T_2 effect. Therefore, in conventional sequences, long T_2 relaxation can be measured in principle even after the application of the RF pulse. However, measuring signal from cortical bone is not straightforward as the conventional duration

of the applied RF pulse and the transverse T_2 relaxation is nearly identical. In such a scenario, the T_2 signal decays quickly before it can be sampled. Hence, there is strong need to apply RF pulses of a shorter duration or at a lower flip angle.

Unlike in SE and GRE sequences where either a spin echo or gradients are used for spin refocusing, in UTE sequences, a non-selective excitation is used. In contrast to the 2-D slice selection, in UTE sequences the entire volume is excited. Also, in UTE sequences, the FID is sampled rather than the echo as is done in a SE or GRE based sequence. Most importantly, the sampling of the FID takes place soon after the RF excitation. Simultaneously, the gradient is ramped up till it reaches a plateau. Thus, the time critical step here is determined by the switching between the transmit/ receive coils since some time must be allowed for the energy in the coil to ring down completely before its ready to receive signal. A radial trajectory is used to fill up the k-space followed by re-gridding onto cartesian points. The FID image (UTE-TE1 image) contain both short T_2 components as well as long T_2 components. A second image based on gradient echo is acquired. A reversed phase gradient is used to obtain this echo signal (UTE-TE2) [Robs 03]. The second image contains long T_2 components only. Therefore, combining UTE-TE1 and UTE-TE2 enables visualizing short T_2 components. The pulse sequence diagram for a dual echo 3-D UTE sequence is shown in Figure 2.18.

In this work, a 3-D dual echo UTE sequence that was installed in the Siemens Biograph mMR scanner (Siemens Healthcare, Erlangen) was used. More details on the the principle and imaging physics of a dual echo 3-D UTE sequence is described in [Rahm 06], [Du 11].

Figure 2.19 shows the contrast between a conventional T_2-TSE and the UTE sequence acquired in a dual-echo mode. Bone tissue is visible distinctively in the first echo of the UTE sequences, while this information is absent in the T_2-TSE sequence.

2.3.6 Two-Point Dixon Sequences

Dixon based techniques enable efficient fat/water separation and have been considered as a potential sequence for the purpose of AC [Eibe 11], [Dixo 84]. The Dixon techniques use the principle of chemical shifts i.e. the difference in resonance frequencies for fat and water components [Bern 04]. Two echoes are generated out of which in one image, the magnetization vectors for fat $\boldsymbol{F}$ and water $\boldsymbol{W}$ are in phase and are out of phase in the other image. In this thesis, this sequence used an echo time of TE=1.23 ms. At start TE=0, both vectors fat $\boldsymbol{F}$ and water $\boldsymbol{W}$ yield an in-phase vector $\boldsymbol{I}_{\text{in}}$, whereas at TE=1.23 ms, an opposed-phase vector $\boldsymbol{I}_{\text{opp}}$ is formed. The vectors $\boldsymbol{I}_{\text{in}}$ and

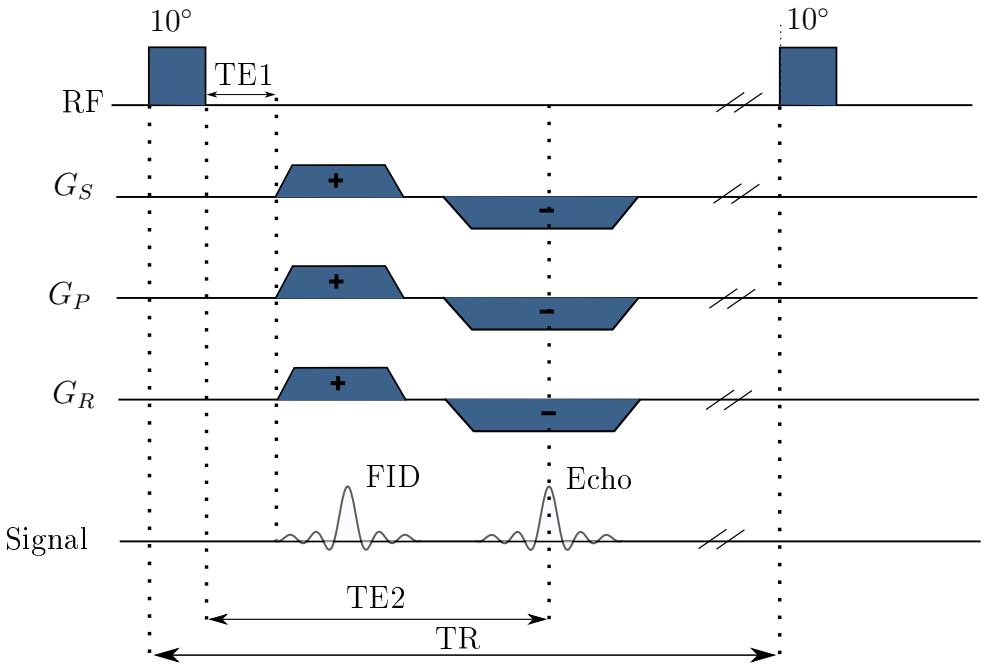

Figure 2.18: Dual echo 3-D UTE sequence diagram. A non-selective RF block pulse is first applied for volumetric excitation. The FID is then immediately sampled soon after to record the first echo image. The second image is based on a gradient echo acquisition (negative gradient). The differences between both the images is used for visualizing tissues with short T_2 [Rahm 06].

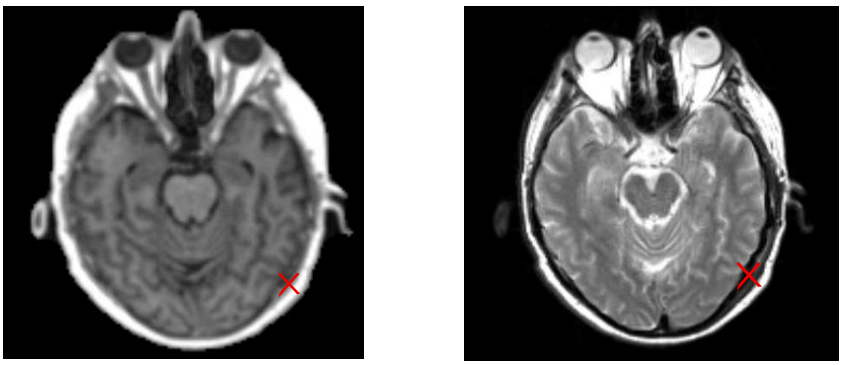

(a) (b)

Figure 2.19: (a) First echo of the UTE sequence and (b) T_2-TSE sequence. The signal from cortical bone is visible from the UTE sequence and the same is absent in the T_2-TSE sequence (red cross lines).

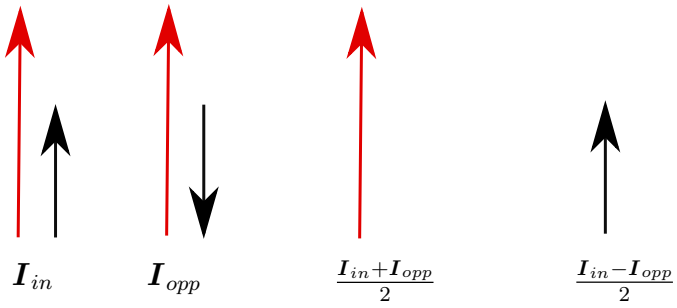

Figure 2.20: Illustration of Dixon magnetization vectors of fat $\boldsymbol{F}$, water $\boldsymbol{W}$, opposed-phase $\boldsymbol{I}_{\text{opp}}$ and in-phase $\boldsymbol{I}_{\text{in}}$ in the absence of any inhomogeneities due to the $\boldsymbol{B_0}$ field. Fat $\boldsymbol{F}$ and water $\boldsymbol{W}$ can be retrieved by the vector difference and sum of $\boldsymbol{I}_{\text{opp}}$ and $\boldsymbol{I}_{\text{in}}$.

$\boldsymbol{I}_{\text{opp}}$ are 180° out of phase in an ideal scenario where inhomogeneities due to $\boldsymbol{B_0}$ field are absent. Figure 2.20 illustrates vector representation of the fat, water separation.

The $\boldsymbol{I}_{\text{in}}$ and $\boldsymbol{I}_{\text{opp}}$ magnetization vectors are related to $\boldsymbol{F}$ and water $\boldsymbol{W}$ vectors through the relation

$$\boldsymbol{I}_{\text{in}} = \boldsymbol{W} + \boldsymbol{F} \tag{2.23}$$

$$\boldsymbol{I}_{\text{opp}} = \boldsymbol{W} - \boldsymbol{F} \tag{2.24}$$

From Equations 2.23 and 2.24, the $\boldsymbol{F}$ and water $\boldsymbol{W}$ can be separated as follows

$$\boldsymbol{W} = \frac{|\boldsymbol{I}_{\text{in}} + \boldsymbol{I}_{\text{opp}}|}{2} \tag{2.25}$$

$$\boldsymbol{F} = \frac{|\boldsymbol{I}_{\text{in}} - \boldsymbol{I}_{\text{opp}}|}{2} \tag{2.26}$$

2.4 PET/MR Hybrid Imaging

Hybrid imaging systems wherein two modalities are combined for a clinical interpretation, has gained wide interest in the recent past. The success of PET/CT and SPECT/CT systems has been well recognized in the medical community [Kapo 04], [Buck 08]. This offers enriched information due to the complementary information from the combined modalities. However, the problem with aforementioned hybrid systems is that the image acquisitions

have to be done sequentially. Typically, a PET succeeds the CT examination in a clinical routine. As far as the examination times are concerned, the CT takes about the order of seconds while PET requires 30 minutes of examination time. Although, the CT provides good anatomical localization it lacks soft tissue contrast. This was one of the motivations to integrate MR, a modality rich in soft tissue contrast together with PET, a modality that images functional processes. This marriage between these two powerful imaging modalities has also opened up several clinical studies [Wies 13], [Drze 12], [Eibe 11], [Gari 13], [Jude 13], [Lade 13], [Wett 13], [Quic 13]. In addition, it has also given rise to several distinctive gains.

1. Automatic co-registration between MR and PET
2. Possibility of performing simultaneously MR and PET examination
3. Elimination of radiation dose due to not requiring a patient CT

This also means that the MR has to substitute the role of the CT in PET/CT in order to fully complement PET imaging. Therefore, tissue attenuation information has to be derived from MR and modeled as PET LACs, in order to perform PET-AC. In this section, a review on the technical side of the PET/MR integration is presented together with some of the open challenges and existing research with regard to MR-based AC.

2.4.1 Technical Details

Several technical and software based issues had to be circumvented in order to integrate and realize a simultaneous PET and MR acquisition. The presence of a strong main magnetic field forced workarounds to determine MR-compatible PET detectors. The most important question to address was to make sure that PET and MR imaging be performed simultaneously with no compromise on either image qualities while at the same time reducing any interference between them. In that sense, the conventional PET detectors used in PET/CT hybrid imaging systems, were found to be sensitive to the static magnetic field. Many research groups have investigated guiding light through optical fibres to outside of the MR FOV [Shao 97b], [Shao 97a], [Cata 06]. Alternatively, it was found that semi-conductor based PET detectors in the form of APDs were suitable for this purpose [Pich 10], [Jude 08], [Jude 13], [Pich 08], [Pich 06]. In view of this problem, different scanner concepts were conceived which would be covered in detail in the forthcoming section. The whole-body hybrid imager as implemented by Siemens Healthcare consists of a 3.0 Tesla MR system with a 60 cm patient bore and 199

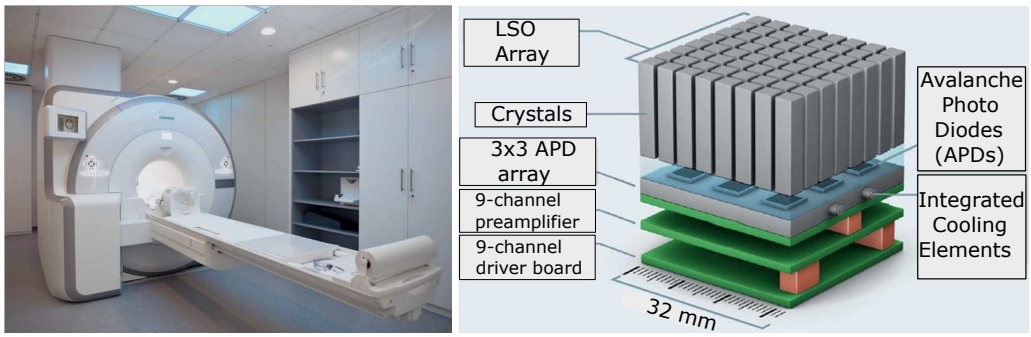

(a) (b)

Figure 2.21: (a) The Simultaneous Siemens Biograph mMR PET/MR scanner. (b) Schematic of a PET detector block used in the Siemens Biograph mMR. An 8×8 arrangement of Lutetium Oxyorthosilicate (LSO) crystals together with a 3×3 avalanche photo diodes convert light flashes to electrical signals. Image source [Quic 11].

cm system length. The MR gradient system provides a maximum gradient amplitude of 45 mT/m and a maximum slew rate of 200 T/m/s and hosts an integrated PET detector. APDs are used for PET signal read outs due to their insensitivity to electromagnetic fields. An 8×8 arrangement of (LSO) crystals and a 3×3 APD array form one PET detector block. One PET ring comprises of 56 such detector blocks and the entire PET detector unit is made up of 8 such rings. The axial FOV of the PET detector covers a length of 258 mm [Dels 11], [Quic 11]. Figure 2.21 shows the Siemens Biograph mMR scanner installed at the Institute of Medical Physics, Erlangen together with a schematic illustration of a PET detector block used.

2.4.2 Configurations

Given the difficulty in integrating the PET detectors within the MR-FOV, three different approaches have been adapted to combine PET and MR modalities in the industry. They are

- Sequential Design
- Simultaneous Design
- Tri-Modality Design.

Sequential Design

In the sequential design, the PET and MR components are separated from each other. The Philips Ingenuity TF PET/MR scanners presently use this configuration. The MR magnet is situated about 3 m away from the PET side, therefore this reduces the cost of building MR-compatible PET detectors [Kale 13]. Consequently, this has the advantage that the PET can accommodate time of flight imaging (TOF) capabilities for PET imaging due to the presence of faster detector electronics. This in principle makes it possible in TOF imaging to localize the annihilation event with the help of the arrival times of the two gamma rays. This information leads to the possibility of generating PET images with better signal to noise ratio. On the hardware front, the system is provided with a 180° pivot on the patient table to make feasible the insertion of the patient to the PET modality following an MR acquisition [Kale 13]. This movement transition may result in slight patient movements and may require post processing techniques for patient registration [Dels 09]. Also, such a design requires larger rooms typically 4.3 m × 13 m to install and house the scanner with increased examination times due to the sequential PET and MR acquisitions [Zaid 11].

Simultaneous Design

The first truly simultaneous PET/MR hybrid system is the Biograph mMR (Siemens AG, Healthcare Sector, Erlangen, Germany). Ten minutes per bed position are allocated for PET acquisition. The PET imaging is performed in the background, while different diagnostic MR sequences are run in the meantime. This design allows to simultaneously image metabolic processes in PET and MRI. Besides, offering precise PET/MR co-registration, this also opens up the possibility to exploit MR information to bin PET raw data towards reconstructing 4-D PET images. In total, examinations for 5 bed-positions can be performed that include head-neck, thorax, abdomen, pelvis, and lower extremity. As pointed out earlier, APDs are used as PET detectors instead of conventional PMTs. This technology therefore does not presently allow for TOF PET acquisitions due to an inferior timing resolution. Due to the inclusion of dedicated MR-compatible PET detectors, they are expensive to build. The advantages include reduction of space requirements and examination times since PET and MR acquisitions are performed in one session.

Tri-Modality Design

This design contains two different scanners, PET/CT and MR installed in different examination rooms. Patients undergo a PET/CT which was followed by an MR scan. This setup is made easy by use of a transport table or a shuttle that can be docked into either stations. No specific MR shielding or alternate PET detectors are necessary given separate rooms for housing the scanners. The acquired MR images can be overlaid on the PET/CT examinations using post-processing softwares for viewing purposes. On the downside, separate room requirements are needed to house these two scanners. Also, such a system does not allow simultaneous MR and PET measurements.

2.4.3 Challenges

While technical hardware complications have been solved, issues related to PET data corrections still persist. A major challenge in PET/MR imaging is AC. In principle, PET works on the concept of photon pair production due to an annihilation event. The photons interact with materials with varying thicknesses that may cause attenuation. Since, MRI measurements are derived from tissue proton densities, they cannot be directly incorporated for PET attenuation correction like it is done with CT in a PET/CT system. Therefore, a major challenge in PET/MR hybrid imaging is to derive attenuation information from MR data. In this section, some of the problems of attenuation correction are reviewed.

Soft Tissue AC

In the current product version of the Siemens Biograph mMR PET/MR scanner, a two-point 3-D Dixon VIBE (Volume Interpolated Breath-Hold Examination) sequence is used for segmenting tissue classes and to produce an attenuation map. Figure 2.22 shows the derivation of the attenuation map.

Overall, four classes (air, fat, soft-tissue/water and lungs) are identified from the in-phase and opposed-phase components of the 3-D Dixon-VIBE sequence. While the air, soft-tissue/water and fat regions are determined from a simple image based thresholding and morphological operations, lung class is segmented by identifying the largest component from a connected component analysis. Most importantly, the cortical bone class is ignored in the attenuation maps. It has therefore been a major focus of research to incorporate cortical bone information in the attenuation maps. A compre-

hensive overview on prior work on this topic is presented in the forthcoming chapter.

Hardware AC

Apart from human soft tissues, the RF coils needed for signal transmission/reception are prevalent within the PET FOV. These are placed at a close vicinity to the patient and are often required in order to obtain images with good image contrast. Examples of such coils include the head-neck RF coil, patient table with integrated spine array RF coil and the flexible RF surface coils. All of these coils potentially attenuate and scatter the 511 keV photons. The head/neck RF coil, patient table and the spine array RF coil are rigid and remain fixed for each patient examination. Therefore, their respective CT templates can be used for PET-AC, since their geometry and pre-defined table positions are know beforehand. This situation is slightly different for the flexible RF coils, as their geometries and precise positions vary across patient examinations. It is therefore imperative to locate them in a patient specific manner. The flexible RF surface coils comprise of four RF-amplifier circuits each consisting of semi-conductor electronics. Figure 2.23 shows an example of a CT template for both rigid and flexible RF coils.

Various research groups have investigated the importance of performing a hardware attenuation correction and have estimated the extent of under-estimation errors therein when the above mentioned coils are not corrected for towards PET-AC. Catana et al. showed that disregarding the RF coils causes severe under-estimation effects [Cata 10]. Although, no concrete error values have been reported by the group, the representative images from their phantom experiments show variations of up to 30%. Tellmann et al. performed brain and torso measurements using cylindrical and NEMA phantom experiments with and without the RF surface coils [Tell 11]. They reported underestimation errors of 14% and 18% on the upper and lower part of the cylindrical phantoms respectively. The experiments from Delso et al. also confirm the inclusion of the RF head/neck coil and even suggest a redesign of the same coil [Dels 10]. They analyzed the total counts and report a 17 % loss of true coincident counts when the RF head/neck coil is present but is not considered for AC. A similar error range of 18.6% was observed through analytic simulations by MacDonald et al., when the AC for the RF head/neck coil was not performed [MacD 11]. They further evaluate the RF surface coils and conclude that CT scans overestimate the PET activity concentration by 28%. They attribute this error to the metal streak artifacts of the RF surface coil electronics when scanned by a CT. As a conclusion, they suggest a

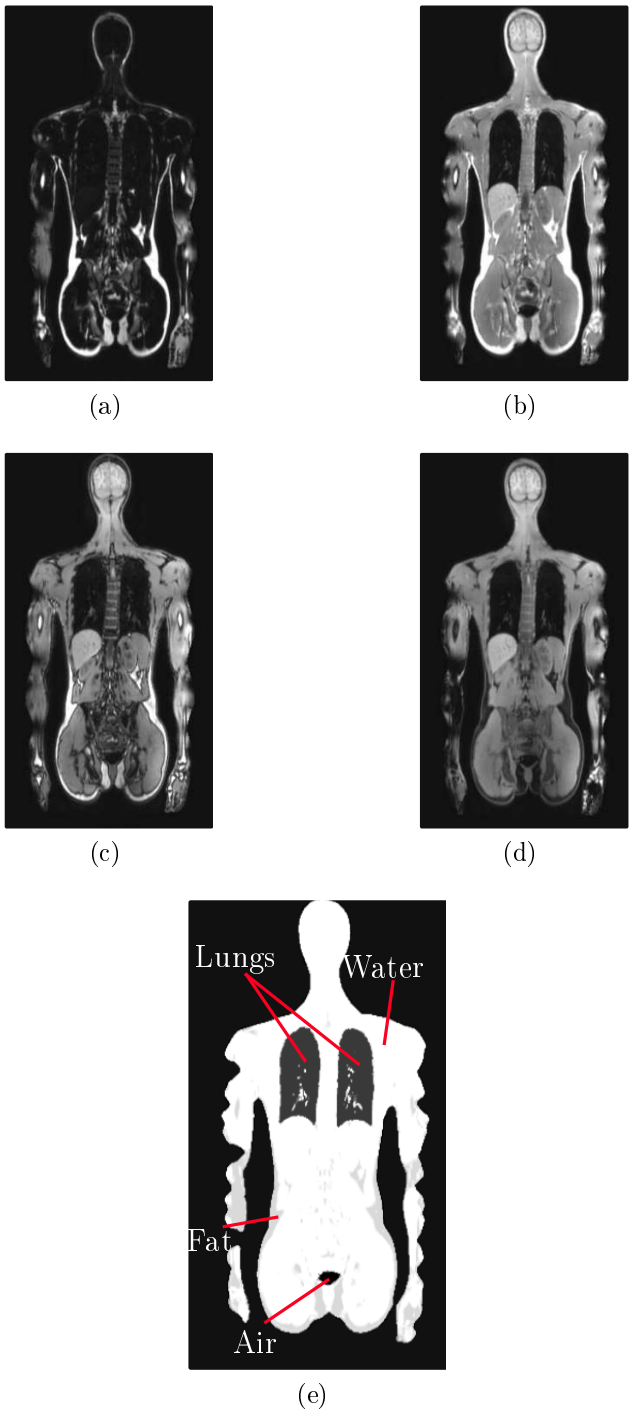

Figure 2.22: Attenuation maps used in the current product version (a) Dixon-fat, (b) Dixon in-phase, (c) Dixon opposed-phase, (d) Dixon-water and (e) Dixon μ-map images. Overall, four class (air, soft tissue/water, fat and lungs) are segmented from the Dixon in-phase and opposed-phase images. Note that cortical bone tissue is replaced by soft tissue in the attenuation map.

redesign of the coil components that are less attenuating in nature or suggest an improvement of the scaling approach from CT to 511 keV energy.

It is therefore evident that the hardware elements attenuate the PET signal considerably and therefore their corresponding attenuation maps need to be included along with those of the patient. Unfortunately, the non-appearance of these hardware elements on the MR images further complicate their localization and detection for generating an MR-based hardware attenuation map. This problem is similar to imaging cortical bone from conventional MR sequences. Since this tissue class lacks rich proton source, it often fails to yield detectable signal on most MR sequences. UTE sequences have been useful in that regard [Keer 10], [Cata 10], [Nava 13c], [Joha 11]. Some groups have even shown evidence that hardware elements could be imaged in principle [Hofm 09], [Grod 12]. However, the reliability and robustness of such an MR-based hardware segmentation approach is still an active research area. Alternate ways as suggested by Paulus et al. include the placement of landmarks that are detectable in order to perform a landmark registration between CT and MR modalities [Paul 11]. They confirm that such an approach enables the location of the RF surface coils. The authors also investigate the possible use of UTE sequence to image them. In their study, a significant attenuation was reported for the phantom regions close to the coil, where most of the attenuating electronics are found. Recently, an automatic approach was presented by Kartmann et al. wherein a non-rigid registration algorithm to generate patient specific attenuation maps for flexible RF coils was evaluated [Kart 13]. Besides the RF surface coils, patient positioning aids are used for patient comfort during long PET acquisition times. The influence of these on PET attenuation has been evaluated by Mantlik et al. and they report an under-estimation of 7.4% for patient head studies when these patient positioning aids are ignored for AC [Mant 11]. Likewise, for PET/MR mammography examinations, the RF breast coil is a known source of attenuating structure. Aklan et al. have shown that a 11% error is to be expected when the RF breast coil is not accounted for [Akla 13]. With respect to the patient table, its non-inclusion in the attenuation map has shown to have a 10% -20% loss of image counts as reported by Pal et al. [Pal 09].

Extension of the MR-FOV

Although the scanner bore size of 60 cm is sufficient to image small objects such as the head and lower extremities, problems arise when examining the torso. Due to lengthy scan times in PET/MR imaging as compared to PET/CT, patients are in practice imaged in arms down orientation. This po-

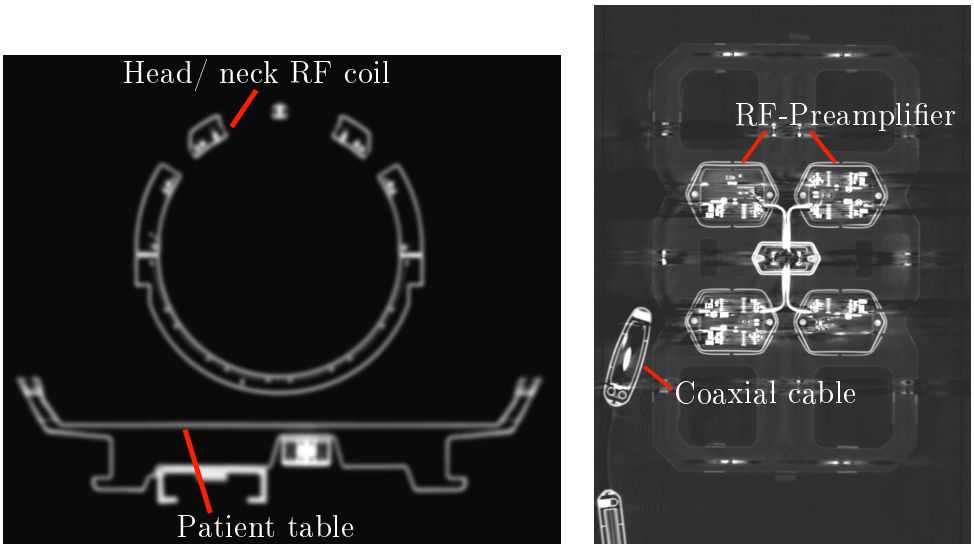

(a) (b)

Figure 2.23: CT templates of the rigid and flexible RF coils. (a) Head/neck RF coil with patient table. Due to their rigid and stationary nature, they are always accounted for PET-AC with a pre-defined table position. (b) A six-channel flexible surface RF coil. The RF pre-amplifier circuitry (arrows) are among the most attenuating material and hence pose problems for PET-AC. Both the images have been adjusted to different window/level settings for the purpose of illustrating critical components.

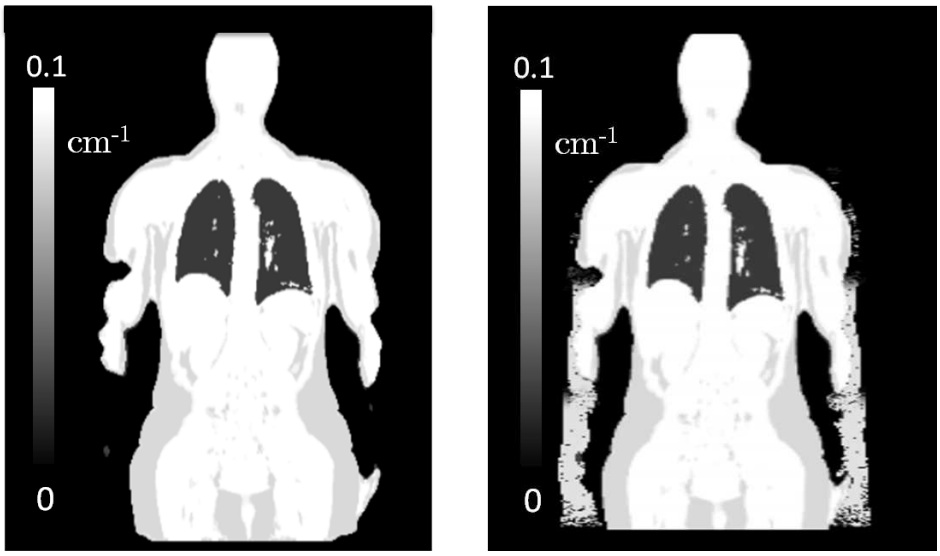

(a) (b)

Figure 2.24: Truncated attenuation map. Arms filled by the MLAA algorithm [Nuyt 13]

sitioning therefore ensures patient comfort. However, one important aspect of the simultaneous PET/MR imaging systems is that the FOV of the MR system is much less than that of its PET counterpart. Therefore the complete MR coverage of the patients' upper extremities cannot be guaranteed and may lead to unwanted truncation of the MR signal in these regions. The cause for such an effect is attributed to gradient non-linearities and magnetic field inhomogeneities [Blum 12]. These signal discontinuities in the resulting MR images also propagate to the corresponding patient attenuation maps. Figure 2.24 shows the degree of truncation observed in the patient attenuation maps. Since such incomplete attenuation maps can hamper in restoring accurate PET activities, many solutions to reconstructing the missing patient arms data have been proposed.

Many approaches exist that exploit PET emission images to complete the signal in the regions of the patients' arms. In the current Siemens Biograph mMR PET/MR product version an algorithm called maximum likelihood reconstruction of attenuation and activity (MLAA) is implemented that addresses this truncation problem [Nuyt 13]. The algorithm uses non-attenuation corrected PET images to estimate the missing data using a maximum a-posteriori condition. An option to invoke this feature can be specified by the user either during patient examination or in an offline PET recon-

struction setting. For Philips Ingenuity TF PET/MR systems this problem is mitigated by obtaining a patient contour from TOF PET NAC images [Blaf12]. Classes inside this mask are assigned with LACs corresponding to air, soft-tissue and lung and are used for PET reconstruction. However, a drawback with this approach is that the algorithm although allows recovering the patients' arms, is specific only to ^{18}F-FDG imaging. The feasibility to extract such information using the PET NAC images from other radioactive tracers has not yet been reported.

As an alternative, an MR-based approach to extending the patients' FOV has been proposed by Blumhagen et al. [Blum 12]. They do this by determining a space-dependent optimal readout gradient that minimizes the distortions due to known gradient non-linearities and main magnetic field inhomogeneities.

2.5 Summary

This chapter provided an introduction to PET and MRI imaging. PET works on the principle of detecting high energy γ-photons following an annihilation event with the body. MRI relies on the proton density information and the tissue relaxation characteristics. On the PET side, an introduction to PET photon attenuation was provided and the existing methods to performing a PET attenuation correction were discussed therein. On the MRI side, an insight into obtaining various image contrasts with standard MRI sequences was provided. The inability of standard MRI sequences to reasonably distinguish cortical bone from air was highlighted. This motivated the introduction of ultrashort echo time based sequences that are capable of imaging the cortical bone. The technical feasibility of combining PET and MRI modalities into one PET/MR hybrid imaging system was discussed and the current challenges in performing MR-based attenuation correction in such systems were reviewed. Forthcoming chapters would cover in depth methods to generate patient specific attenuation maps for human tissues using the specialized ultrashort echo time sequences.

Chapter 3

MR-based Attenuation Map Generation

Parts of this chapter contains work and results published in the following article Bharath. K. Navalpakkam, Harald Braun, Torsten Kuwert and Harald H. Quick "Magnetic resonance-based attenuation correction for PET/MR hybrid imaging using continuous valued attenuation maps", Investigative Radiology, Vol. 48, No. 5, pp. 323–32, May 2013.

In this chapter, a general framework for generating CT-like attenuation maps from MR data required to correct PET images is presented. More importantly, an algorithm outline is presented that converts a set MR images into a pseudoCT. Besides attenuation correction in PET/MR imaging, such pseudoCTs also find applications for MR-based radiotherapy, MR-based focused ultrasound and for generating realistic brain phantoms for perfusion imaging [Rank 13], [Brad 09], [Aich 13]. This chapter is structured as follows. In the first section, an overview of the existing methods to creating attenuation maps based solely on MR information is discussed. The second section presents the details on patient acquisition and image pre-processing steps. A detailed description of the pattern recognition algorithm is also presented in the same section. In the third section, we evaluate the generated attenuation maps with the patient CT as the criterion standard. Results of this evaluation strategy is presented in the fourth section. In the last two sections, we present a discussion of achieved results and conclusions of this chapter. Overall, the MRAC framework introduced in this chapter forms the basis for PET-AC that will be introduced in Chapters 4 and Chapter 5.

3.1 Introduction

The advent of hybrid PET/MR systems has opened up the possibility to combine two powerful imaging modalities in one hybrid imaging device [Pich 08], [Zaid 11]. As mentioned in section 2.4.1 MR, on the one hand, is known for its excellent soft tissue contrast by means of a plethora of imaging sequences and has the potential to provide highly specific anatomical localization. PET, on the other hand, enables highly specific metabolic imaging. In comparison to PET/CT, PET/MR offers a reduction of radiation dose. Therefore, the hybrid PET/MR system can be a highly beneficial tool for brain and whole-body studies [Drze 12], [Wies 13], [Brau 12]. However, MR-based attenuation correction (AC) for PET images still remains a problem at large. In PET/CT hybrid imaging, a simple energy scaling from CT energies (40-140 keV) to PET energy (511 keV) is sufficient to generate attenuation maps [Kina 98, Kina 03]. But such a relationship is not straightforward to achieve in PET/MR hybrid imaging as MR and PET inherently measure two different physical phenomena. The main problem in MR-derived attenuation maps is to distinguish between bone and air as these two materials offer little to no signal in most MR sequences. However, their LACs vary significantly (air: 0 cm^{-1}, bone: 0.1510 cm^{-1}) at 511 keV. A separate patient CT acquired on a different scanner can be used for AC. However, such a setup would increase patient radiation dose and complicate clinical workflow. A method to hence simulate a CT from an MR or a set of MR images would therefore be beneficial. A major impediment of conventional MR sequences (T_1-weighted/ T_2-weighted) is its inability to image cortical bone. Figure 3.1 illustrates such a scenario. This problem has motivated many a workarounds towards determining robust attenuation maps. The approaches can be broadly classified into atlas registration, image segmentation or image classification methods for both brain and whole-body applications.

For whole body imaging several different ways of handling this issue have been proposed. Martinez-Möeller et al. propose a simple image segmentation based for MR based attenuation map derivation. The authors segment a 2-point Dixon sequence into relevant tissues class such as air, fat, soft-tissue and lung. They identify the lung class through a connected-component analysis. To determine the importance of bone for PET-AC, they replace cortical bone by soft-tissue in CT-derived attenuation maps. The authors argue this method of representing cortical bone as soft tissue does not undermine the clinical value of the attenuation corrected PET images [Mart 09]. According to this study, ignoring cortical bone resulted in an 8% decrease in standardized uptake value (SUV) for osseous lesions and a 4% decrease for head and neck lesions. They note largest underestimation errors (13%) for lesions in

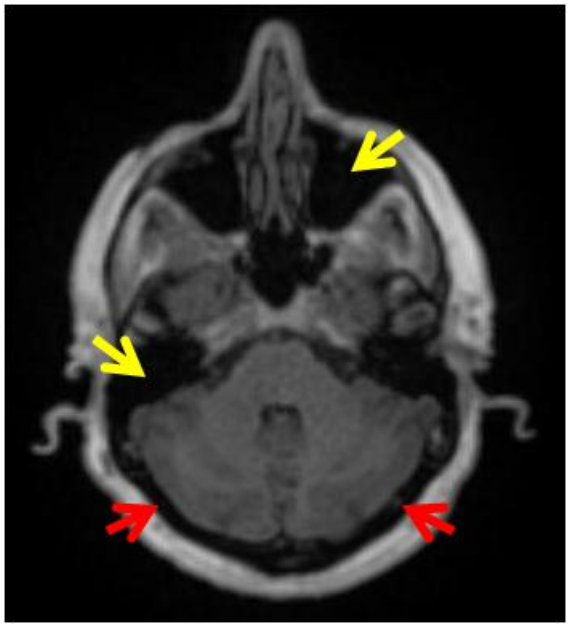

Figure 3.1: Absence of cortical bone signal from standard T_1-weighted MR sequence. The cortical bone (red arrows) and air regions (yellow arrows) have low voxel intensities and therefore these classes cannot be easily distinguished.

the pelvic region. A similar approach to the above is proposed and evaluated by Schulz et al. [Schu 11]. The authors derive 3-class segmentation (air, tissue and lung) based attenuation map from a T_1-weighted MR sequence. They use automatic thresholds and region growing approaches for the same. Accordingly, a 13.7% underestimation for bone lesions is reported when cortical bone is disregarded. However, the authors did not investigate their μ-map for brain studies. Similar approaches based on image segmentation have also been pursued [Stei 10], [Hu 10]. This has raised the question in the research community whether it is necessary or even beneficial to consider cortical bone as an additional class.

As discussed in the previous chapter, in current PET/MR hybrid systems, an attenuation map based on a 3-D Dixon sequence is commonly used. Depending upon the vendor, the μ-map in these systems mainly distinguish between two (air, soft tissue) to three classes (air, water and fat), for the head regions. For the torso region, lung is identified as an additional class. Due to relatively fast acquisition, easily integrable workflow and a simple segmentation based approach, this has found wide usage among the first clinical studies of this relatively new hybrid imaging modality. Although, the 3-D

Dixon based μ -map is generally accepted/utilized for torso studies, cortical bone omission for head studies has shown to have a significant impact on PET-AC [Sama 12], [Cata 10], [Nava 13c].

While most of the recent research focuses on the effect on PET-AC when including or disregarding a class [Sama 12], [Keer 11], very few MR-based AC implementations that consider bone exist, that can be of potential use in a clinical environment for i.e. with sufficiently fast acquisition and processing times. Several groups have investigated the inclusion of cortical bone as an attenuating class for brain PET-AC from atlas registration or from the previously introduced dedicated MRI sequences such as UTE sequences. These sequences are capable of visualizing cortical bone and other structures with very short T_2^* [Hofm 08, Cata 10, Berk 12, Keer 10]. Using UTE, Keereman et al. proposed a three class (air, soft tissue, cortical bone) segmentation approach from relaxation maps derived from UTE sequences and reported a 5% mean error across brain regions [Keer 10]. The authors use region growing and simple threshold based segmentation to produce attenuation maps. Simulations from Catana et al. also confirm the need for at least three classes - air, water, and cortical bone - due to differences in quantification for GM, white matter (WM) and CSF regions [Cata 10]. However, in their study the authors do not perform a thorough statistical analysis of the obtained results. Instead of using one image contrast, Berker et al. propose a triple echo based MR acquisition to identify cortical bone, water and fat classes from one sequence [Berk 12]. From this sequence, the authors segment cortical bone, adipose tissue (fat), soft-tissue and air. For PET-AC, they evaluate the results by manually positioning 8 volumes of interest (VOI) on CT volumes. They report error deviations from -4.8% to 7.6% for these VOIs. Fei et al. also generate attenuation maps including cortical bone from a T_1-weighted MR sequence [Fei 12]. They compare their results to patient transmission scans and obtain 6.5% error deviations. Error discrepancies for specific anatomical regions were evaluated and reported by Malone et al., who used a non-rigid brain template atlas registration approach [Malo 11]. A similar non-rigid registration approach is proposed by Schreibmann et al. [Schr 10]. The authors propose a three step registration approach to warping an atlas CT to the patient MR. However, they report the evaluation of their registration algorithm on only one PET image.

Other innovative approaches to deriving attenuation maps include PET-TOF information. Since, the attenuation maps are directly derived from PET emission data, they may be useful for both standalone PET scanners and PET/MR hybrid imaging systems [Salo 11], [Nuyt 13]. However, the efficacy of such attenuation maps have not been evaluated for PET/MR imaging.

An inherent drawback of all of the above mentioned MR based approaches is that they compare their segmentation results to a segmented patient CT. This approximation might hold true for attenuating classes like air, GM, WM or fat, the wide range of CT voxel values of 300-2000 HU however indicates the need for more than one class for the representation of cortical bone. Catana et al. analyzed specific LAC values (0.1360 cm^{-1}, 0.1430 cm^{-1}, 0.1510 cm^{-1}, 0.1710 cm^{-1} and 0.1800 cm^{-1}) to be assigned to the cortical bone class [Cata 10]. They conclude that of the investigated values, 0.1510 cm^{-1} offered the best trade-off between the bias and variability in PET reconstructions. With this LAC value, they notice a 5% difference to the scaled CT based PET reconstructions. Furthermore, a discrete assignment of μ-values as is done in a limited class segmentation approach, would not represent adequately the bone densities as they vary vastly across patients and also across regions in the body [Keer 11].

Along this line of thought, few attempts have been made to predict μ-values on a continuous scale from MR images. Hofmann et al. propose pattern recognition methods by incorporating local neighborhood information from MR images in addition to an atlas registration step [Hofm 11], [Hofm 08]. They generate their model based on feature extraction from T_1-weighted spin echo sequences. They have, however not evaluated their approach on UTE sequences. Johansson et al. have derived substitute CTs from multiple MR acquisitions (two UTE and one 3-D SPACE) per patient using Gaussian Mixture Model regression [Joha 11]. They evaluate their results for ^{18}F-FLT (^{18}F-3'-fluro-3'-deoxy-L-thymidine) PET-AC and report a 1.9% error deviation for brain [Lars 13]. In a further publication, they show that the two UTE sequences at different flip angles are sufficient for a substitute CT generation [Joha 12]. Although their results look promising, an acquisition time of 6 minutes only for the purpose of AC may not be suitable for PET/MR applications. In the present study, a similar approach is followed i.e. to emulate a CT from a UTE and a 3-D Dixon sequence and subsequently to evaluate its efficacy on PET attenuation by comparing it to a patient CT as the gold standard.

In this research work, besides the 3-D Dixon-VIBE based attenuation correction sequence, only an additional UTE sequence was required overall for the purpose of PET-AC. This, therefore reduced the overall acquisition time to 2 minutes.

3.2 Material and Methods

3.2.1 Patient Examinations

Ten patients (4 female, 6 male, age: 50.6 ± 10.6 Y, weight 70.5 ± 9.1 kgs) underwent a PET/CT scan on a Biograph 64, (Siemens AG, Healthcare Sector, Erlangen, Germany) followed by a PET/MR examination on a Biograph mMR (Siemens AG, Healthcare Sector, Erlangen, Germany) 137.2 ± 43.0 minutes after the PET/CT examination. All patients were administered ^{18}F-FDG as a radiotracer (maximum 246 MBq, minimum 126 MBq). No additional tracer or radiation dose was administered due to the PET/MRI examination. The clinical routine used for simultaneous PET/MR acquisitions for head scans includes a three plane localizer, a 3-D Dixon sequence, anatomical T_1-TSE and T_2-TSE sequences as well as an echo-planar-diffusion weighted sequence. All patients had a clinical investigation in the whole-body and no abnormalities in the brain regions. Additionally, for the purpose of this work a UTE sequence was acquired. The PET acquisition time per bed position was set to 10 minutes. Due to the simultaneous acquisition of PET and MR data on the Biograph mMR system and the 10 minutes PET acquisition time, the overall acquisition time was not prolonged by the additional UTE sequence. Altogether, the 3-D Dixon and the UTE sequence were used for the purpose of deriving MR based attenuation maps. The UTE sequence was acquired with the following parameters: TE1 = 0.07 ms, TE2 = 2.46 ms, flip angle of 10°, TR = 11.94 ms and FOV= 300×300 mm^2, slice thickness 1.56 mm, acquisition matrix size 192×192, TA = 99 seconds. The images were then reconstructed to a matrix size of 192×192×192 voxels with an isotropic voxel size of 1.56×1.56×1.56 mm^3. No apparent differences due to geometrical distortion or scaling were noted between the 2 echoes. Second, a two-point Dixon sequence in 3-D mode was acquired with voxel dimensions of 192×126×128 and a voxel size of 2.6×2.6×2.23 mm^3, TR = 3.6 ms, TE = 1.23 ms, FA = 10°, TA = 19 seconds. For patient examinations, an approval from the Institutional Review and Ethical Board was obtained. All patients gave their informed and written consent.

3.2.2 Continuous Valued μ-Map Generation

Each of the 10 patients had one CT, and two MR sequences (UTE and 3-D Dixon sequence) and the MR/CT pairs contained identifiable air, cortical bone, water and fat information available. Thus, a regression model was trained to learn this mapping between the two modalities considering the CT as the reference. The idea was to use the trained model to predict a

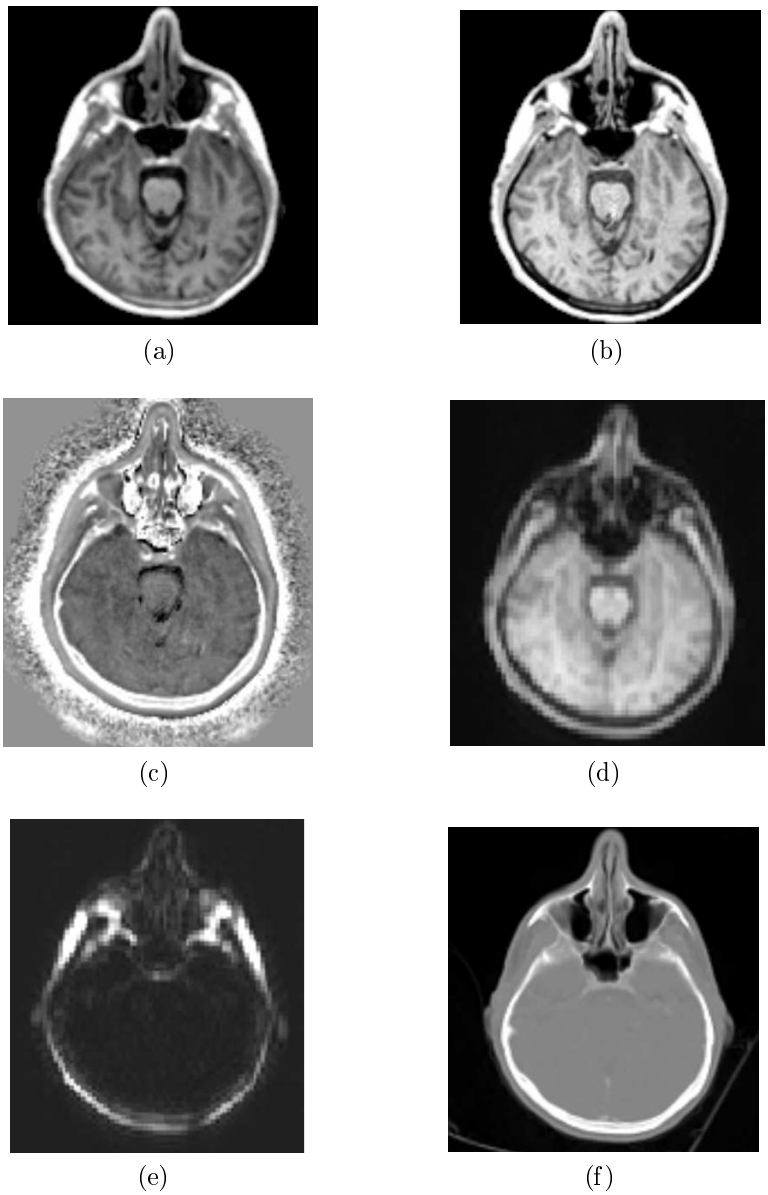

Figure 3.2: MR sequences and patient CT used for MR-based attenuation correction. (a) $I_1(x, y, z)$:UTE-TE1, (b) $I_2(x, y, z)$:UTE-TE2, (c) difference image $S(x, y, z) = lnI_1(x, y, z) - lnI_2(x, y, z)$. (d) 3-D Dixon-water, (e) 3-D Dixon-fat. Note that the cortical bone is clearly visible in (c) as compared to (d) or (e). (f) Patient CT.

pseudoCT from the two MR sequences for a new patient, thereby making obsolete the need for a patient CT. Two sets were created for regression training/validation and testing respectively. Each set contained 5 patients and the model training was done on the training/validation set and the model was tested on real world data using the testing test. No part of the testing data set was used for training and therefore no bias towards model selection was introduced. Also, the patients had no clinical question in the brain but did so for the rest of the body.

Since voxel intensities are to be learnt between the MR data and the corresponding CT, a pre-requisite therefore for an optimal model training is a properly registered CT/MR data. Misalignments between the modalities is therefore crucial and may lead to overfitting or incorrect learning if not accounted for. After the image registration step, an air mask is calculated. Further, to better visualize cortical bone a difference map is calculated using the relation $S(x, y, z) = lnI_1(x, y, z) - lnI_2(x, y, z)$ where $I_1(x, y, z)$ and $I_2(x, y, z)$ represent UTE-TE1 and UTE-TE2 image intensities respectively. This relation is similar to the relaxation maps used by Keereman et al. [Keer 10]. The authors segment these tissue classes using pre-defined thresholds to generate attenuation maps. While in our approach, using them we estimate attenuation maps by a pattern recognition algorithm. The advantage of the relaxation maps is that, they are quantitative MR images and provide information on tissue relaxation properties. Therefore, robust pseudoCTs can be generated using relaxation maps rather than training on voxel intensities of UTE-TE1 and UTE-TE2. Altogether, the air mask, together with CT, difference map, 3-D Dixon fat and 3-D Dixon water images are used to train the regression model. An illustration of the used MR sequences and the corresponding patient CT is shown in Figure 3.2. A flow diagram is illustrated in Figure 3.3.

3.2.3 Image Pre-Processing

The following were the image pre-processing steps that were performed prior to the model training step. The complete pipeline required to generate MR-based attenuation maps was automatic. A manual intervention was only necessary for ensuring a fair comparison between MR and CT based attenuation maps. The following are the key steps involved prior to regression training.

Rigid Registration

A rigid transformation model was applied for two reasons.

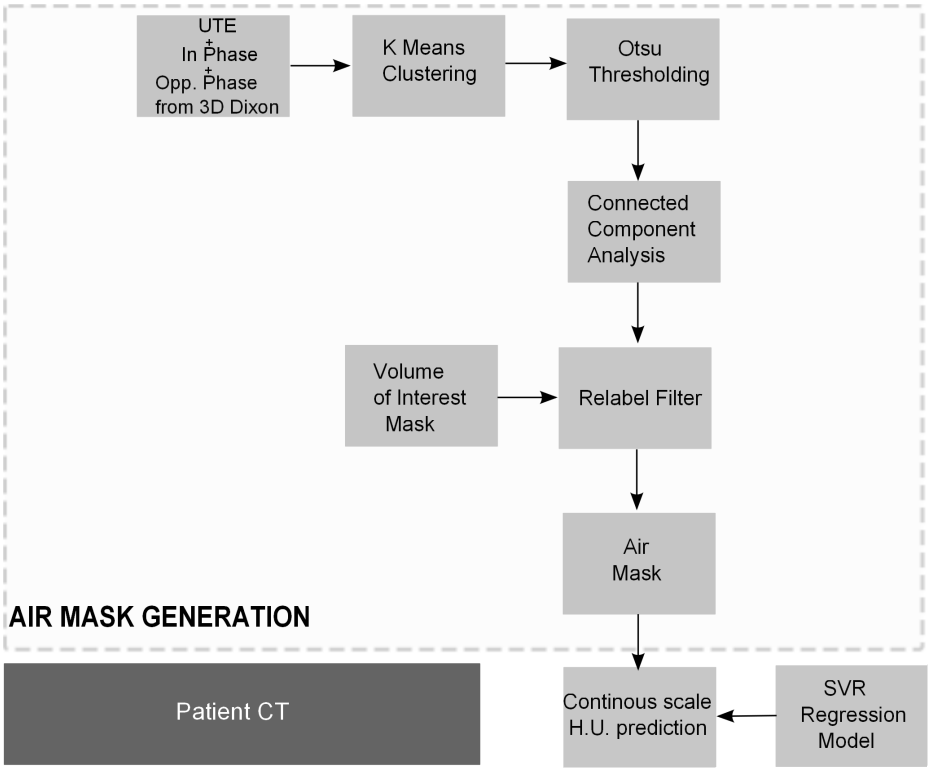

Figure 3.3: Framework for generating MR-based pseudoCTs for PET-AC. An air mask derivation allows for prediction of fat, water and cortical bone class from MR sequences.

- Alignment of different MR sequences to each other. This is important since, MR sequences are acquired simultaneously during long PET examinations. Thus, certain patient head movements are inevitable.

- Transformation of the patient CT to the MR space. The CT and MR datasets are acquired on different scanner geometries. This step therefore aligns CT datasets to the MR space.

Since MR and CT data sets originate from the same patient and the focus was on the head region, a simple rigid transformation was sufficient to map the voxel correspondence. Furthermore, patients in PET/CT are imaged in an arms up position and in PET/MR in an arms down position. Additionally, the patient table as well as certain positioning aids not used in PET/MR are visible in the CT images. Therefore, as a pre-processing step, the patient bed and positioning aids as well as the patients' arms were excluded from the CT volume in order to preserve the head alone to achieve better registration results. This exclusion of patient aids was done manually. This cropped CT was then rigidly registered to the UTE-TE1 image using mutual information as the similarity measure. Mutual information was chosen since the modalities at hand are different and there exist no linear intensity distribution between them. Also, the UTE-TE1 was used here as opposed to UTE-TE2 or any of the 3-D Dixon-VIBE components. The reason for this was that UTE-TE1 contains cortical bone information and so does the patient CT. Hence, this information would aid in better registration between the two modalities. Subsequently, to eliminate the influence of possible patient motion between the acquisition of UTE-TE1 and the 3-D Dixon-water images, these two images were also rigidly registered and the obtained transformation parameters were used in bringing the UTE-CT registered pair to the 3-D Dixon space. The feature extraction was performed at the resolution of the 3-D Dixon-VIBE volumes which is $2.6\times2.6\times2.23$ mm^3. All registrations were performed using elastix [Klei 10]. In a patient setup, however, the registration is not necessary as the CT images are only needed for the initial training.

Morphological Closing Operation

A volume of interest mask is necessary for the following reasons

- To restrict the training to only fat, soft-tissue and cortical bone classes.

- To assist in segmenting air regions inside the head.

To achieve this, a morphological closing operator with a 9mm spherical kernel was run on the UTE-TE1 volume. Since our main interest was to analyze the PET quantification effects on the brain regions, the VOI mask was manually cropped to preserve only those regions above the nose.

Voxelwise Addition

Following the closing operation, voxelwise intensities are added from three different MR volumes. These include in-phase, opposed-phase components of the 3-D Dixon-VIBE sequence and the UTE-TE1. This is done as a preparation step for the air mask segmentation. The rationale behind this step is that individually, each of these volumes have air intensities but the cortical bone intensities are present only in UTE-TE1. Moreover, as the UTE-TE1 is obtained by sampling the FID soon after RF excitation, it contains high background noise. Thus, any segmentation algorithm performed directly on UTE-TE1 is prone to yield erroneous results especially at the air-soft-tissue and soft-tissue interfaces. The resulting image from this additive intensity operation yields a good image contrast between air and other tissue classes. This aids in a reliable air mask segmentation.

Air Mask

The composite volume from the previous step is then subjected to a scalar K-means classification with the within-cluster sum of squared errors metric [Macq 67]. K-means is an unsupervised technique used widely for cluster analysis. The algorithm identifies discrete classes within a dataset and assigns them a membership to their closest centroids. The input to the algorithm is the data that needs to be clustered, number of classes and their initial centroids. The algorithm then iteratively associates each data point to its nearest centroid and recomputes the means for each class. Two steps are involved here namely the assignment and update steps. In the assignment step, the data points are assigned a centroid close to it. In the update step, cluster centroids are computed by updating the new means for all the cluster members within that group. The two steps alternate until none of the clusters move. Let the data set be given as $\mathcal{X} = \{\boldsymbol{x}_1, \boldsymbol{x}_2, ...\boldsymbol{x}_n\}$, $\boldsymbol{x}_i \in \mathbb{R}^d$, the objective of k-means algorithm is to partition the data into $k(\leq n)$ disjoint sets $\mathcal{S} = \{S_1, S_2....S_k\}$, k is the number of clusters specified and n is the number of data points. The objective function minimizing the within-cluster sum of squared differences is then given by

Algorithm 3.1 k-means

input : $\mathcal{X} = \{\boldsymbol{x}_1, \boldsymbol{x}_2, ...\boldsymbol{x}_n\}$, $\boldsymbol{x}_i \in \mathbb{R}^d$, the number of clusters k and their initial cluster centers

output: $\mathcal{S} = \{S_1, S_2...S_k\}$ along with their centroids $\{\boldsymbol{m}_1, \boldsymbol{m}_2...\boldsymbol{m}_k\}$

repeat
  for $j \leftarrow 1$ **to** k **do**
    $S_j \leftarrow \emptyset$
    Assignment Step:
    for $i \leftarrow 1$ **to** n **do**
      $\mathcal{A}(\boldsymbol{x}_i) = \underset{1 \leq j \leq k}{\operatorname{argmin}} ||\boldsymbol{x}_i - \boldsymbol{m}_j||^2$
      $S_{\mathcal{A}(\boldsymbol{x}_i)} \leftarrow S_{\mathcal{A}(\boldsymbol{x}_i)} \cup \{\boldsymbol{x}_i\}$
    end
  end
  Update Step:
  for $j \leftarrow 1$ **to** k **do**
    $\boldsymbol{m}_j = \frac{1}{|S_j|} \sum_{\boldsymbol{x}_i \in S_j} \boldsymbol{x}_i$
  end
until *none of the centroids change or when maximum number of iterations is reached*;

$$\underset{\mathcal{S}}{\operatorname{argmin}} \sum_{j=1}^{k} \sum_{\boldsymbol{x_i} \in S_j} ||\boldsymbol{x}_i - \boldsymbol{m}_j||^2 \tag{3.1}$$

Here, $\boldsymbol{m}_j$ represents the centroid of cluster j. The data point $\boldsymbol{x}_i$ is assigned to the cluster S_j closest to it. The cluster centers are then recomputed in the update step

$$\boldsymbol{m}_j = \frac{1}{|S_j|} \sum_{\boldsymbol{x}_i \in S_j} \boldsymbol{x}_i \tag{3.2}$$

The algorithm pseudocode is shown in Algorithm 3.1.

Altogether, 30 clusters were specified as an input to the algorithm together with initial cluster mean estimates starting from 0 to maximum voxel value.

Otsu Thresholding

The Otsu thresholding was performed on k-means clustered image to obtain a binary image [Otsu 79]. Otsu's method works by analyzing the his-

togram data and determining that threshold which minimizes the intra-class variance. The output is a binary image that has separated foreground from background intensities. Let the image under consideration have N gray levels $[1, 2, ..., N]$ and let n_i be the number of pixels at any level i. The normalized probability distribution is given by

$$p_i = \frac{n_i}{L} \tag{3.3}$$

$$p_i \geq 0, \sum_{i=1}^{N} p_i = 1 \tag{3.4}$$

and L is the total number of pixels in the image.

The goal is to separate the image into two disjoint classes C_B, C_F denoting the background and foreground pixels, respectively. C_B has pixel levels $[1, .., l]$ while C_F has $[l + 1, .., N]$. The corresponding class occurrence probabilities are given by

$$\omega_B = P(C_B) = \sum_{i=1}^{l} p_i = \omega(l) \tag{3.5}$$

$$\omega_F = P(C_F) = \sum_{i=l+1}^{N} p_i = 1 - \omega(l) \tag{3.6}$$

The class mean levels are then defined as

$$\mu_B = \sum_{i=1}^{l} i \cdot P(i|C_B) = \sum_{i=1}^{l} \frac{i \cdot p_i}{\omega_B}$$

$$\mu_B = \frac{\mu(l)}{\omega(l)} \tag{3.7}$$

where

$$\mu(l) = \sum_{i=1}^{l} i \cdot p_i \tag{3.8}$$

$$\mu_F = \sum_{i=l+1}^{N} i \cdot P(i|C_F) = \sum_{i=1}^{l} \frac{i \cdot p_i}{\omega_F}$$

$$\mu_F = \frac{\mu_T - \mu(l)}{1 - \omega(l)} \tag{3.9}$$

where

$$\mu_T = \mu(N) = \sum_{i=1}^{N} i \cdot p_i \tag{3.10}$$

μ_T represents the total mean. For any selection of the threshold l, the following relation holds good

$$\omega_F \mu_F + \omega_B \mu_B = \mu_T \tag{3.11}$$

$$\omega_F + \omega_B = 1 \tag{3.12}$$

The respective class variances for classes C_B and C_F are given by

$$\sigma_B^2 = \sum_{i=1}^{l} \frac{(i - \mu_B)^2 p_i}{\omega_B}$$

$$\sigma_F^2 = \sum_{i=l+1}^{N} \frac{(i - \mu_F)^2 p_i}{\omega_F}$$

Further, in order to determine how well the threshold value l has performed, a *goodness* of fit measure is defined [Fuku 90]

$$\lambda = \frac{\sigma_{inter}^2}{\sigma_T^2} \tag{3.13}$$

σ_{inter}^2, σ_{intra}^2 and σ_T^2 represent inter-, intra-class and total variances and are defined as

$$\sigma_{intra}^2 = \omega_B \sigma_B^2 + \omega_F \sigma_F^2$$

$$\sigma_{inter}^2 = \omega_B (\mu_B - \mu_T)^2 + \omega_F (\mu_F - \mu_T)^2 \tag{3.14}$$

Substituting Equation 3.11 in Equation 3.14 we get

$$\sigma_{inter}^2 = \omega_B (\mu_B - \omega_F \mu_F - \omega_B \mu_B)^2 + \omega_F (\mu_F - \omega_F \mu_F - \omega_B \mu_B)^2 \tag{3.15}$$

$$= \omega_B (\mu_B (1 - \omega_B) - \omega_F \mu_F)^2 + \omega_F (\mu_F (1 - \omega_F) - \omega_B \mu_B)^2 \tag{3.16}$$

Using Equation 3.12 we get

$$\sigma^2_{inter} = \omega_B(\mu_B\omega_F - \omega_F\mu_F)^2 + \omega_F(\mu_F\omega_B - \omega_B\mu_B)^2 \tag{3.17}$$

$$= \omega_B[\omega_F(\mu_F - \mu_B)]^2 + \omega_F[\omega_B(\mu_F - \mu_B)]^2 \tag{3.18}$$

$$= (\omega_B\omega_F^2 + \omega_B^2\omega_F)(\mu_F - \mu_B)^2 \tag{3.19}$$

$$= \omega_B\omega_F(\omega_F + \omega_B)(\mu_F - \mu_B)^2 \tag{3.20}$$

Substituting the value of $\omega_F + \omega_B$ from Equation 3.12 in Equation 3.20

$$\sigma^2_{inter} = \omega_B\omega_F(\mu_F - \mu_B)^2 \tag{3.21}$$

$$\sigma^2_T = \sum_{i=1}^{N}(i - \mu_T)^2 p_i$$

The optimal threshold then corresponds to that which maximizes the inter-class variance σ^2_{inter} or the parameter λ from Equation 3.13. Thus, for each l value $\lambda(l)$ is calculated

$$\lambda(l) = \frac{\sigma^2_{inter}(l)}{\sigma^2_T} \tag{3.22}$$

The dependency of Equation 3.21 on l can be seen by substituting the values for μ_B, μ_F and $\omega_B + \omega_F$ from Equations 3.7, 3.9, and 3.12

$$\sigma^2_{inter}(l) = [\omega(l)(1 - \omega(l))]\left[\frac{\mu_T - \mu(l)}{1 - \omega(l)} - \frac{\mu(l)}{\omega(l)}\right]^2 \tag{3.23}$$

$$= \omega(l)(1 - \omega(l))\left[\frac{\omega(l)\mu_T - \omega(l)\mu(l) - \mu(l)(1 - \omega(l))}{\omega(l)(1 - \omega(l))}\right]^2 \tag{3.24}$$

Simplifying Equation 3.24, we obtain the objective function to be maximized which is given by the relation

$$l^* = \underset{l}{\operatorname{argmax}}\ \frac{(\mu_T\omega(l) - \mu(l))^2}{\omega(l)(1 - \omega(l))} \tag{3.25}$$

where l^* is the desired threshold. The pseudocode for Otsu's thresholding is illustrated in Algorithm 3.2.

To remove any stray segmentations that are not air, a connected component analysis was performed on the binary image. A relabeling filter then

Algorithm 3.2 Otsu thresholding

input : Image histogram $\mathcal{H}$, gray levels $[1, 2..., N]$
output: Optimal threshold value l^*
Calculate p_i, $\forall i$;
Initialize $\omega(0)$, $\mu(0)$;
for $l \leftarrow 1$ **to** N **do**
  Compute $\omega(l)$, $\mu(l)$;
  Compute $\sigma^2_{inter}(l)$;
end
return : $l^* = \underset{l}{\operatorname{argmax}}\ \sigma^2_{inter}(l)$

sorted the identified components according to their weights in a descending manner. From this, the labels with the largest components greater than 1000 voxels were assigned to the air class. Finally, the air mask is obtained by multiplying the identified air class with the VOI mask (Figure 3.4).

The air mask is vital for consideration because of three reasons

- The LAC for air is 0 cm^{-1}. Therefore its contribution for PET attenuation is relatively insignificant as compared to the other tissue classes.
- The segmented air mask also reduces the computational burden for the regression model by not including the air voxels in the training/testing process.
- High PET uptakes are observed inside of the air mask. Any spurious air prediction in the middle of the brain would lead to severe under estimation for that voxel. The air mask therefore ensures all voxels inside are classified either as cortical bone, fat or soft-tissue classes.

To evaluate the generated air-mask, pre-defined volumes of interest (VOI's) were placed and evaluated on commonly identified air regions on both CT and MR volumes as shown in Figure 3.5. All software processing was done using algorithms from Insight Toolkit [Iban 05].

3.2.4 Epsilon-Insensitive Support Vector Regression Training

Prior to pseudoCT estimation, a model generation step is necessary to learn the mapping between the associated classes from the extracted MR feature vectors to their corresponding CT HU. A pattern recognition based approach namely epsilon-insensitive support vector regression (ϵ-SVR) is used for this

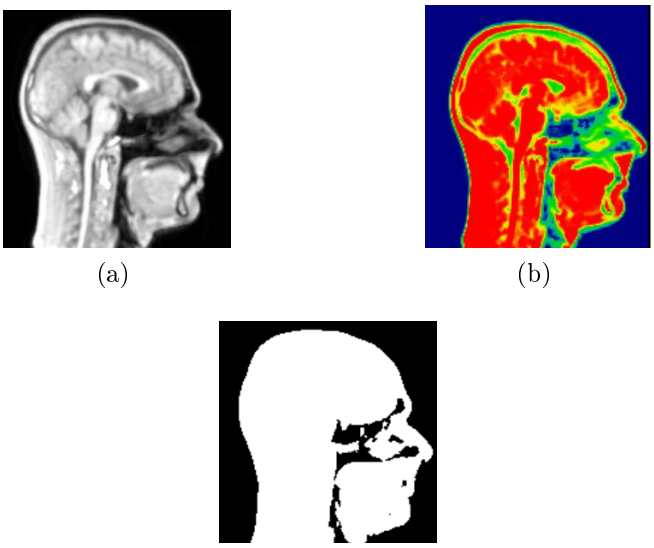

(a) (b)

(c)

Figure 3.4: Steps in air mask generation. (a) Voxelwise addition from UTE-TE1 and in-phase and opposed phases images. (b) Result of k-means classification. (c) Air mask obtained from connected component analysis. The regression model prediction can now be restricted to fat, water and cortical bone inside the air mask.

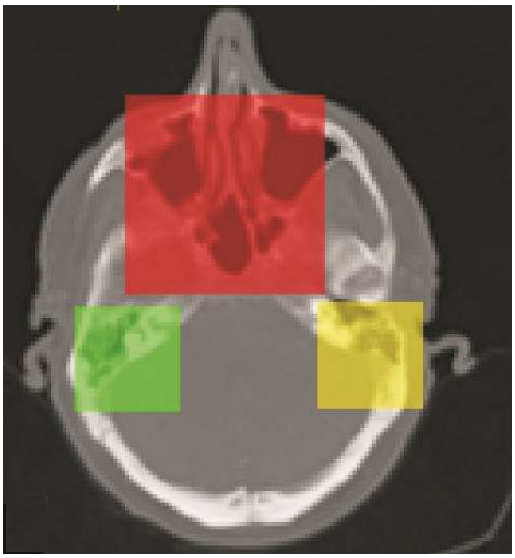

Figure 3.5: Sample placements of VOIs around air regions.

purpose [Smol 04], [Vapn 98]. In contrast to support vector classification, ϵ-SVR produces real valued estimates.

Hard-Margin

Given feature vectors $\mathcal{X} = \{\boldsymbol{x}_1, \boldsymbol{x}_2,....\boldsymbol{x}_N\}$ where $\boldsymbol{x}_i \in \mathbb{R}^d$ and their corresponding target responses $\{y_1, y_2,....y_N\}$, $y_i \in \mathbb{R}$, ϵ-SVR attempts to find a suitable mapping $f(\boldsymbol{x}_i)$ as close as possible to y_i with at most ϵ errors. This can be visualized as having a ϵ-insensitive tube around the target values y_i. For a data that can be modelled with a linear model, a regression function can determined in the input space with errors being tolerated within the ϵ tube. The goal is to determine an optimal regression hyperplane $f(\boldsymbol{x}_i)$ given the input feature vectors $\mathcal{X}$ [Smol 04]. The Equation of such a hyperplane is then given by

$$f(\boldsymbol{x}) = \boldsymbol{w}^T\boldsymbol{x}+b \tag{3.26}$$

where $\boldsymbol{w} \in \mathbb{R}^d$ and $b \in \mathbb{R}$. $\boldsymbol{w}$ is the normal vector to the hyperplane and b is the bias. The convex optimization problem that is minimized is given by

$$\min_{\boldsymbol{w}, b} \frac{1}{2}||\boldsymbol{w}||_2^2 \tag{3.27}$$

subject to

$$\begin{cases} y_i - (\boldsymbol{w}^T\boldsymbol{x}_i + b) \leq \epsilon \\ (\boldsymbol{w}^T\boldsymbol{x}_i + b) - y_i \leq \epsilon \quad \forall i \end{cases} \tag{3.28}$$

for $i = 1, 2...N$, where N is the number of training instances.

Soft-Margin

The above formulation does not allow for any slackness and hence may be unsuitable for data that cannot be fit with a linear regression model adequately. In the soft margin design, slackness parameters ξ and ξ^* are introduced, thus allowing for any errors beyond the ϵ-insensitive zone. For the values within a distance of ϵ, no errors are penalized in the objective function. However, the errors beyond the ϵ tolerance but within $[\xi, \xi^*]$, are penalized linearly. The constrained convex optimization problem is then given by [Shig 05]

$$\min_{\boldsymbol{w}, b, \boldsymbol{\xi}, \boldsymbol{\xi^*}} \frac{1}{2}||\boldsymbol{w}||_2^2 + C\sum_{i=1}^{N}(\xi_i + \xi_i^*) \tag{3.29}$$

subject to

$$\begin{cases} y_i - (\boldsymbol{w}^T \boldsymbol{x}_i + b) \leq \epsilon + \xi_i \\ (\boldsymbol{w}^T \boldsymbol{x}_i + b) - y_i \leq \epsilon + \xi_i^* \\ \xi_i, \xi_i^* \geq 0 \qquad\qquad \forall i \end{cases} \tag{3.30}$$

ξ_i, ξ^* represent slack variables that are 0 if the error is within ϵ range and non-zero otherwise. Here $\boldsymbol{\xi} = (\xi, ...\xi_N)^T$ and $\boldsymbol{\xi}^* = (\xi^*, ...\xi_N^*)^T$.

$$|\xi|_\epsilon = \begin{cases} 0 & \text{if } |\xi| \leq \epsilon \\ |\xi| - \epsilon & \text{otherwise} \end{cases}$$

The constant C is a trade-off factor that controls the flatness of the regression function and the tolerance deviations beyond ϵ [Smol 04]. We solve the constrained optimization problem in Equation 3.30 by maximizing the following Lagrangian formulation with $\alpha, \alpha^*, \tau, \tau^*$ being the Lagrange multipliers.

$$L_m(\boldsymbol{w}, b, \boldsymbol{\xi}, \boldsymbol{\xi}^*, \boldsymbol{\tau}, \boldsymbol{\tau}^*, \boldsymbol{\alpha}, \boldsymbol{\alpha}^*) = \frac{1}{2}||\boldsymbol{w}||_2^2 + C\textstyle\sum_{i=1}^N(\xi + \xi_i^*)$$

$$- \sum_{i=1}^N (\tau_i \xi_i + \tau_i^* \xi_i^*) - \sum_{i=1}^N \alpha_i(\epsilon + \xi_i - y_i + \boldsymbol{w}^T \boldsymbol{x}_i + b)$$

$$- \sum_{i=1}^N \alpha_i^*(\epsilon + \xi_i^* + y_i - \boldsymbol{w}^T \boldsymbol{x}_i - b) \tag{3.31}$$

subject to

$$\alpha, \alpha_i^*, \tau_i, \tau_i^* \geq 0 \ \forall i \tag{3.32}$$

Here, $\boldsymbol{\alpha} = (\alpha, ...\alpha_N)^T, \boldsymbol{\alpha}^* = (\alpha^*, ...\alpha_N^*)^T$, $\boldsymbol{\tau} = (\tau, ...\tau_N)^T$ and $\boldsymbol{\tau}^* = (\tau^*, ...\tau_N^*)^T$.

At the saddle point, the optimal solution is obtained by taking the derivative of Equation 3.31 with respect to $(\boldsymbol{w}, b, \boldsymbol{\xi}, \boldsymbol{\xi}^*)$ and setting it to zero.

$$\frac{\partial L_m(\boldsymbol{w}, b, \boldsymbol{\xi}, \boldsymbol{\xi}^*, \boldsymbol{\tau}, \boldsymbol{\tau}^*, \boldsymbol{\alpha}, \boldsymbol{\alpha}^*)}{\partial \boldsymbol{w}} = \boldsymbol{w} - \sum_{i=1}^N (\alpha_i - \alpha_i^*)\boldsymbol{x}_i = 0 \tag{3.33}$$

$$\Rightarrow \boldsymbol{w} = \sum_{i=1}^N (\alpha_i - \alpha_i^*)\boldsymbol{x}_i \tag{3.34}$$

$$\frac{\partial L_m(\boldsymbol{w}, b, \boldsymbol{\xi}, \boldsymbol{\xi}^*, \boldsymbol{\tau}, \boldsymbol{\tau}^*, \boldsymbol{\alpha}, \boldsymbol{\alpha}^*)}{\partial b} = \sum_{i=1}^{N}(\alpha_i^* - \alpha_i) = 0 \tag{3.35}$$

$$\frac{\partial L_m(\boldsymbol{w}, b, \boldsymbol{\xi}, \boldsymbol{\xi}^*, \boldsymbol{\tau}, \boldsymbol{\tau}^*, \boldsymbol{\alpha}, \boldsymbol{\alpha}^*)}{\partial \xi_i} = C - \alpha_i - \tau_i = 0 \tag{3.36}$$

$$\Rightarrow \tau_i = C - \alpha_i, \;\; \forall i, \;\; \alpha_i \in [0, C]$$

$$\frac{\partial L_m(\boldsymbol{w}, b, \boldsymbol{\xi}, \boldsymbol{\xi}^*, \boldsymbol{\tau}, \boldsymbol{\tau}^*, \boldsymbol{\alpha}, \boldsymbol{\alpha}^*)}{\partial \xi_i^*} = C - \alpha_i^* - \tau_i^* = 0 \tag{3.37}$$

$$\Rightarrow \tau_i^* = C - \alpha_i^*, \;\; \forall i, \;\; \alpha_i^* \in [0, C]$$

Substituting Equations 3.34, 3.35, 3.36, 3.37 into Equation 3.31 we get

$L_m(\boldsymbol{\xi}, \boldsymbol{\xi}^*, \boldsymbol{\alpha}, \boldsymbol{\alpha}^*)$

$$= \frac{1}{2}\sum_{i=1}^{N}\sum_{j=1}^{N}\boldsymbol{x}_i(\alpha_i - \alpha_i^*)\cdot\boldsymbol{x}_j(\alpha_j - \alpha_j^*) + C\sum_{i=1}^{N}(\xi_i + \xi_i^*)$$

$$-\sum_{i=1}^{N}((C - \alpha_i)\xi_i + (C - \alpha_i^*)\xi_i^*)$$

$$-\sum_{i=1}^{N}\alpha_i(\epsilon + \xi_i - y_i + \sum_{j=1}^{N}(\alpha_j - \alpha_j^*)\boldsymbol{x}_i^T\boldsymbol{x}_j + b)$$

$$-\sum_{i=1}^{N}\alpha_i^*(\epsilon + \xi_i^* + y_i - \sum_{j=1}^{N}(\alpha_j - \alpha_j^*)\boldsymbol{x}_i^T\boldsymbol{x}_j - b) \tag{3.38}$$

$L_m(\boldsymbol{\xi}, \boldsymbol{\xi}^*, \boldsymbol{\alpha}, \boldsymbol{\alpha}^*)$

$$= \frac{1}{2}\sum_{i=1}^{N}\sum_{j=1}^{N}(\alpha_i - \alpha_i^*)(\alpha_j - \alpha_j^*)\boldsymbol{x}_i^T\boldsymbol{x}_j + C\sum_{i=1}^{N}(\xi_i + \xi_i^*)$$

$$- C\sum_{i=1}^{N}(\xi_i + \xi_i^*) + \sum_{i=1}^{N}(\alpha_i\xi_i - \alpha_i^*\xi_i^*)$$

$$-\sum_{i=1}^{N}\sum_{j=1}^{N}\alpha_i\boldsymbol{x}_i^T\boldsymbol{x}_j(\alpha_j - \alpha_j^*) + \sum_{i=1}^{N}\sum_{j=1}^{N}\alpha_i^*\boldsymbol{x}_i^T\boldsymbol{x}_j(\alpha_j - \alpha_j^*)$$

$$+\sum_{i=1}^{N}\alpha_i y_i - \sum_{i=1}^{N}\alpha_i^* y_i - \sum_{i=1}^{N}\alpha_i\epsilon - \sum_{i=1}^{N}\alpha_i^*\epsilon$$

$$-\sum_{i=1}^{N}\alpha_i\xi_i - \sum_{i=1}^{N}\alpha_i^*\xi_i^* + b\sum_{i=1}^{N}(\alpha_i^* - \alpha_i) \tag{3.39}$$

By rearranging terms we get

$L_m(\boldsymbol{\xi}, \boldsymbol{\xi}^*, \boldsymbol{\alpha}, \boldsymbol{\alpha}^*)$

$$= \frac{1}{2}\sum_{i=1}^{N}\sum_{j=1}^{N}(\alpha_i - \alpha_i^*)(\alpha_j - \alpha_j^*)\boldsymbol{x}_i^T\boldsymbol{x}_j - \sum_{i=1}^{N}\sum_{j=1}^{N}(\alpha_i - \alpha_i^*)(\alpha_j - \alpha_j^*)\boldsymbol{x}_i^T\boldsymbol{x}_j$$

$$\sum_{i=1}^{N}(\alpha_i\xi_i - \alpha_i^*\xi_i^*) - \sum_{i=1}^{N}(\alpha_i\xi_i - \alpha_i^*\xi_i^*)$$

$$+\sum_{i=1}^{N}\alpha_i y_i - \sum_{i=1}^{N}\alpha_i^* y_i$$

$$-\sum_{i=1}^{N}\alpha_i\epsilon - \sum_{i=1}^{N}\alpha_i^*\epsilon \tag{3.40}$$

On canceling terms the Equation simplifies to

$$L_m(\boldsymbol{\xi}, \boldsymbol{\xi}^*, \boldsymbol{\alpha}, \boldsymbol{\alpha}^*)$$

$$= -\frac{1}{2}\sum_{i=1}^{N}\sum_{j=1}^{N} \boldsymbol{x}_i^T \boldsymbol{x}_j(\alpha_i - \alpha_i^*)(\alpha_j - \alpha_j^*) + \sum_{i=1}^{N} y_i(\alpha_i - \alpha_i^*) - \epsilon\sum_{i=1}^{N}(\alpha_i + \alpha_i^*)$$

This yields the following optimization problem in the dual form

$$\max_{\boldsymbol{\alpha}, \boldsymbol{\alpha}^*} -\frac{1}{2}\sum_{i=1}^{N}\sum_{j=1}^{N}(\alpha_i - \alpha_i^*)(\alpha_j - \alpha_j^*)\boldsymbol{x}_i^T\boldsymbol{x}_j - \epsilon\sum_{i=1}^{N}(\alpha_i + \alpha_i^*) + \sum_{i=1}^{N} y_i(\alpha_i - \alpha_i^*) \tag{3.41}$$

subject to

$$\begin{cases} \sum_{i=1}^{N}(\alpha_i - \alpha_i^*) = 0 \\ 0 \leq \alpha_i \leq C,\ 0 \leq \alpha_i^* \leq C \quad \forall i \end{cases} \tag{3.42}$$

Karush-Kuhn-Tucker (KKT) sufficiency conditions further need to be satisfied for an optimal solution. KKT complimentary conditions state that the product of the constraints and the dual variables must vanish at the point of solution [Smol 04]:

$$\tau_i\xi_i = (C - \alpha_i)\xi_i = 0\ \forall i \tag{3.43}$$

$$\tau_i^*\xi_i^* = (C - \alpha_i^*)\xi_i^* = 0\ \forall i \tag{3.44}$$

$$\alpha_i(\epsilon + \xi_i - y_i + \boldsymbol{w}^T\boldsymbol{x}_i + b) = 0\ \forall i \tag{3.45}$$

$$\alpha_i^*(\epsilon + \xi_i^* + y_i - \boldsymbol{w}^T\boldsymbol{x}_i - b) = 0\ \forall i \tag{3.46}$$

The following inferences can be deduced:

- We know from Equation 3.42 that $0 \leq \alpha_i, \alpha_i^* \leq C$. Further from Equations 3.43 and 3.44 we infer that (ξ_i, ξ_i^*) are non-zero only when $\alpha_i = C$ or $\alpha_i^* = C$. These correspond to data points that lie beyond the ϵ-insensitive tube. Consequently, terms in parenthesis in Equations 3.45 or 3.46 become zero and the values of ξ_i or ξ_i^* are thus given by

$$\epsilon + \xi_i - y_i + \boldsymbol{w}^T \boldsymbol{x}_i + b = 0 \tag{3.47}$$

$$\Rightarrow \xi_i = y_i - f(\boldsymbol{x}_i) - \epsilon \ \forall i \tag{3.48}$$

$$\epsilon + \xi_i^* + y_i - \boldsymbol{w}^T \boldsymbol{x}_i - b = 0 \tag{3.49}$$

$$\Rightarrow \xi_i^* = f(\boldsymbol{x}_i) - \epsilon - y_i \ \forall i \tag{3.50}$$

- When $\xi_i = 0$ or $\xi_i^* = 0$, it follows from Equations 3.43 and 3.44 that $0 < \alpha_i < C$ or $0 < \alpha_i^* < C$. Then either of the Equations below hold true:

$$\epsilon - y_i + \boldsymbol{w}^T \boldsymbol{x}_i + b = 0 \tag{3.51}$$

$$\epsilon + y_i - \boldsymbol{w}^T \boldsymbol{x}_i - b = 0 \tag{3.52}$$

This signifies that those data points satisfying $y_i - f(\boldsymbol{x}) = +\epsilon$, $0 < \alpha_i < C$ holds good and likewise for $y_i - f(\boldsymbol{x}) = -\epsilon$, $0 < \alpha_i^* < C$.

- When both α_i and α_i^* are zero, then $|y_i - f(\boldsymbol{x})| < \epsilon$ meaning the data points are inside the ϵ tube. As a result, these points do not contribute to the design of the function. On the other hand, data points that satisfy $|y_i - f(\boldsymbol{x})| \geq \epsilon$, have $0 < \alpha_i \leq C$ and $0 < \alpha_i^* \leq C$ and are called support vectors since they contribute to the design of the optimal function.

- Consequently, the parameter b can be estimated by averaging them across all the support vectors whose $\boldsymbol{w}$ and $\boldsymbol{x}_i$ satisfy the following Equations

$$b = y_i - \boldsymbol{w}^T \boldsymbol{x_i} - \epsilon \ \text{ for } 0 < \alpha_i < C \tag{3.53}$$

$$b = y_i - \boldsymbol{w}^T \boldsymbol{x_i} + \epsilon \ \text{ for } 0 < \alpha_i^* < C \tag{3.54}$$

- The regression function can determined by substituting the value for $\boldsymbol{w}$ in Equation 3.26

$$f(\boldsymbol{x}) = \sum_{i=1}^{N} (\alpha_i - \alpha_i^*)(\boldsymbol{x}_i^T \boldsymbol{x}) + b \tag{3.55}$$

Kernel-Trick

A non-linear function is required in cases where a linear regression function does not fit all the training data. In order to find a regression function that best fit the input data, an optimal hyperplane is found in a feature space of a higher dimension $\mathcal{F}$ than the original input space $\mathcal{X}$. The transform that does the mapping of the input data $\boldsymbol{x}_i$ to this higher dimensional feature space is called a kernel $\phi : \mathcal{X} \rightarrow \mathcal{F}$. The kernel mapping offers the possibility to determine a linear regression function in $\mathcal{F}$. Thus, the kernel mapping is much effective across data that are complex and that cannot be easily approximated by a linear regression model in the input space $\mathcal{X}$. The convex optimization problem is then given by

$$\min_{\boldsymbol{w}, b, \boldsymbol{\xi}, \boldsymbol{\xi}^*} \frac{1}{2}||\boldsymbol{w}||_2^2 + C\sum_{i=1}^{N}(\xi_i + \xi_i^*) \tag{3.56}$$

subject to

$$\begin{cases} y_i - (\boldsymbol{w}^T\phi(\boldsymbol{x}) + b) \leq \epsilon + \xi_i \\ \boldsymbol{w}^T\phi(\boldsymbol{x}) + b - y_i \leq \epsilon + \xi_i^* \\ \xi_i, \xi_i^* \geq 0 \qquad\qquad \forall i \end{cases} \tag{3.57}$$

$\boldsymbol{w}^T\phi(\boldsymbol{x})$ represents the dot product in the feature space $\mathcal{F}$ and $\boldsymbol{w} \in \mathcal{F}$.

A kernel function $K(\boldsymbol{x}_i, \boldsymbol{x}_j) \in \mathbb{R}$ can be defined in terms of the mapping function $\phi(\boldsymbol{x})$ given by

$$K(\boldsymbol{x}_i, \boldsymbol{x}_j) = \phi^T(\boldsymbol{x}_i)\phi(\boldsymbol{x}_j) \tag{3.58}$$

With this formulation (Equation 3.58), the mapping of input vectors $\boldsymbol{x}$ to the feature space can be done implicitly via the kernel function. In other words, one need not compute explicitly the co-ordinates of $\phi(\boldsymbol{x})$ in $\mathcal{F}$. Only the dot product $K(\boldsymbol{x}_i, \boldsymbol{x}_j)$ that lives in $\mathcal{F}$ is needed here.

The optimization problem that needs to maximized is expressed using the Lagrange multipliers $\alpha, \alpha^*, \tau, \tau^*$ [Ma 03], [Smol 04].

$$L_m(\boldsymbol{w},b,\boldsymbol{\tau}, \boldsymbol{\xi}, \boldsymbol{\alpha}, \boldsymbol{\alpha}^*) = \frac{1}{2}||\boldsymbol{w}||_2^2 + C\textstyle\sum_{i=1}^{N}(\xi + \xi_i^*)$$

$$- \sum_{i=1}^{N}(\tau_i\xi_i + \tau_i^*\xi_i^*) - \sum_{i=1}^{N}\alpha_i(\epsilon + \xi_i - y_i + \boldsymbol{w}^T\phi(\boldsymbol{x}_i) + b) \tag{3.59}$$

$$-\sum_{i=1}^{N}\alpha_i^*(\epsilon+\xi_i^*+y_i-\boldsymbol{w}^T\phi(\boldsymbol{x}_i)-b)$$

subject to

$$\alpha,\alpha_i^*,\tau_i,\tau_i^*\geq 0\ \forall i$$

We perform a partial differentiation of Equation 3.59 with respect to $(\boldsymbol{w},b,\boldsymbol{\xi},\boldsymbol{\xi}^*)$. This yields the following optimal conditions

$$\frac{\partial L_m(\boldsymbol{w},b,\boldsymbol{\xi},\boldsymbol{\xi}^*,\boldsymbol{\tau},\boldsymbol{\tau}^*,\boldsymbol{\alpha},\boldsymbol{\alpha}^*)}{\partial \boldsymbol{w}}=\boldsymbol{w}-\sum_{i=1}^{N}(\alpha-\alpha_i^*)\phi(\boldsymbol{x}_i)=0 \tag{3.60}$$

$$\frac{\partial L_m(\boldsymbol{w},b,\boldsymbol{\xi},\boldsymbol{\xi}^*,\boldsymbol{\tau},\boldsymbol{\tau}^*,\boldsymbol{\alpha},\boldsymbol{\alpha}^*)}{\partial b}=\sum_{i=1}^{N}(\alpha_i^*-\alpha_i)=0 \tag{3.61}$$

$$\frac{\partial L_m(\boldsymbol{w},b,\boldsymbol{\xi},\boldsymbol{\xi}^*,\boldsymbol{\tau},\boldsymbol{\tau}^*,\boldsymbol{\alpha},\boldsymbol{\alpha}^*)}{\partial \xi_i}=C-\alpha_i-\tau_i=0 \tag{3.62}$$

$$\frac{\partial L_m(\boldsymbol{w},b,\boldsymbol{\xi},\boldsymbol{\xi}^*,\boldsymbol{\tau},\boldsymbol{\tau}^*,\boldsymbol{\alpha},\boldsymbol{\alpha}^*)}{\partial \xi_i^*}=C-\alpha_i^*-\tau_i^*=0 \tag{3.63}$$

Rearranging Equations 3.60,3.62 and 3.63 gives

$$\boldsymbol{w}=\sum_{i=1}^{N}(\alpha-\alpha_i^*)\phi(\boldsymbol{x}_i) \tag{3.64}$$

$$\tau_i=C-\alpha_i \tag{3.65}$$

$$\tau_i^*=C-\alpha_i^* \tag{3.66}$$

Similar to the soft margin scenario, we substitute the values of $(\boldsymbol{w},\tau_i,\tau_i^*)$ from Equations 3.64, 3.65 and 3.66 in Equation 3.59. This yields the following dual optimization problem that is maximized

$$\max_{\boldsymbol{\alpha},\boldsymbol{\alpha}^*}-\frac{1}{2}\sum_{i=1}^{N}\sum_{j=1}^{N}(\alpha_i-\alpha_i^*)(\alpha_j-\alpha_j^*)\phi^T(\boldsymbol{x}_i)\phi(\boldsymbol{x}_j)-\epsilon\sum_{i=1}^{N}(\alpha_i+\alpha_i^*)+\sum_{i=1}^{N}y_i(\alpha_i-\alpha_i^*) \tag{3.67}$$

subject to

$$\begin{cases} \sum_{i=1}^{N}(\alpha_i - \alpha_i^*) = 0 \\ 0 \leq \alpha_i \leq C,\ 0 \leq \alpha_i^* \leq C \quad \forall i \end{cases} \tag{3.68}$$

A radial basis kernel (RBF) $K(\boldsymbol{x}_i, \boldsymbol{x}_j)$ was chosen to project the training data to a higher dimensional feature space.

$$K(\boldsymbol{x}_i, \boldsymbol{x}_j) = e^{-\gamma||\boldsymbol{x}_i - \boldsymbol{x}_j||^2} \tag{3.69}$$

γ is the width of the RBF kernel. The regression function for a new feature vector $\boldsymbol{x}$ can be formulated as

$$f(\boldsymbol{x}) = \sum_{i=1}^{N}(\alpha_i - \alpha_i^*)K(\boldsymbol{x}_i, \boldsymbol{x}) + b \tag{3.70}$$

The optimal function for soft margin case, given by Equation 3.55 contains the dot products between the feature vectors in the input space. Using the kernel, we compute the dot products between the transformed feature vectors that exist in a higher dimensional space. However, Equation 3.70 suggests that we need to determine only dot products $K(\boldsymbol{x}_i, \boldsymbol{x})$ implicitly. As such it is considered useful for problems having lower number of input features. In our case, the extracted features include mean, median, variance, maximum and minimum values across a 3×3×3 local neighborhood from 3-D Dixon fat, 3-D Dixon water and difference map volumes (derived from UTE-TE1 and UTE-TE2). Thus for a new patient, the same features are extracted and from the function that is learnt, an HU estimate $f(\boldsymbol{x})$ that models as close as possible the target value (Real CT) (y_i) is determined. A soft-margin was used with slackness constraints ξ, ξ^* that allowed errors beyond the ε-insensitive tube, while at the same time penalizing the cost function. ϵ-SVR with kernel allows to project the input data to a higher dimensional feature space. Overall, the number of features is less than the number of instances. That is an 18-dimensional feature vector was at hand. Therefore for such problem, a linear kernel method may not be suitable [Chan 11]. An RBF kernel is therefore necessary for separating the features in the feature space. This forms the basis for using ϵ-SVR for this particular problem. Altogether five quadruplets of images were used for training and validation. A higher number of feature instances are obtained since the training is done directly on the voxel intensities. At the resolution of the 3-D Dixon-VIBE 2.6×2.6×2.23 mm^3 for each patient dataset, a total of $3{\cdot}10^5$ feature instances were produced. Therefore, the training set contains $15{\cdot}10^5$ such instances. A random subset was extracted from the training samples and a subsequent grid search was performed to determine optimal parameters of ($C = 8$, $\gamma = 1$, $\epsilon = 0.0625$) through a 5-fold cross validation method to avoid overfitting. All pattern recognition processing was done using LIBSVM [Chan 11].

Patient	Correct air classification (%)
P1	81.73
P2	84.57
P3	73.28
P4	63.63
P5	77.96
Mean	**76.23**

Table 3.1: Patient specific air classification rate (%).

3.2.5 Generation of Continuous Valued μ-Maps for Patients not Included in the Training Process

For a new patient not in the training set, an air mask is generated and features across 3×3×3 voxel neighborhood are extracted from MR images: difference map, 3-D Dixon fat and 3-D Dixon water images. The trained ϵ-SVR is then used to predict HU on a continuous scale for bone, fat and water classes inside of the air mask.

3.3 Results

3.3.1 Air Mask Evaluation

The overall air classification rate per patient is enlisted in Table 3.1. The mean correctly classified air rate was 76.23% across all patients for the drawn ROI's. Most deviations were observed in the air-soft tissue and bone-soft tissue interfaces where MR susceptibility artifacts limit a precise segmentation.

3.3.2 PseudoCTs

While the effect these pseudoCTs have in comparison to the patient CT for PET-AC is investigated in the next chapter, in the current section, we perform a qualitative assessment of the generated pseudoCTs. Figure 3.6 shows a comparison of the generated MR-based attenuation maps together with CT-based attenuation maps for 5 patients. Visually, the pseudoCTs look similar to the patient CTs, except the regions near the ear and nose where there exist a mixture of thin bone and air regions. The air mask

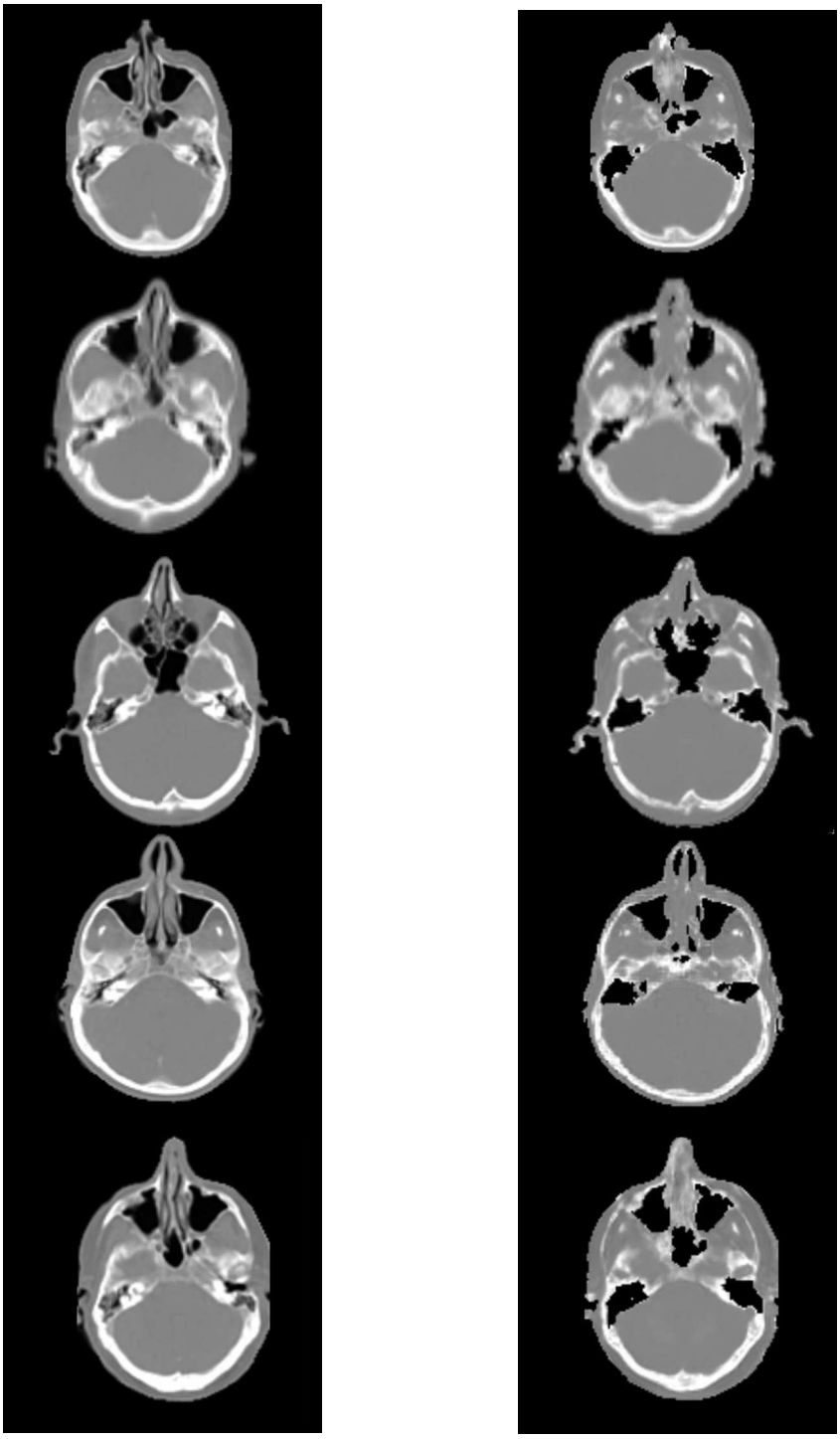

(a) (b)

Figure 3.6: Exemplar transaxial slices from the patient CT (left column) and the corresponding slice from the generated pseudoCTs. Visually, the pseudoCTs emulate the CT, except for the air-bone mixture regions where the segmentation algorithms assign air.

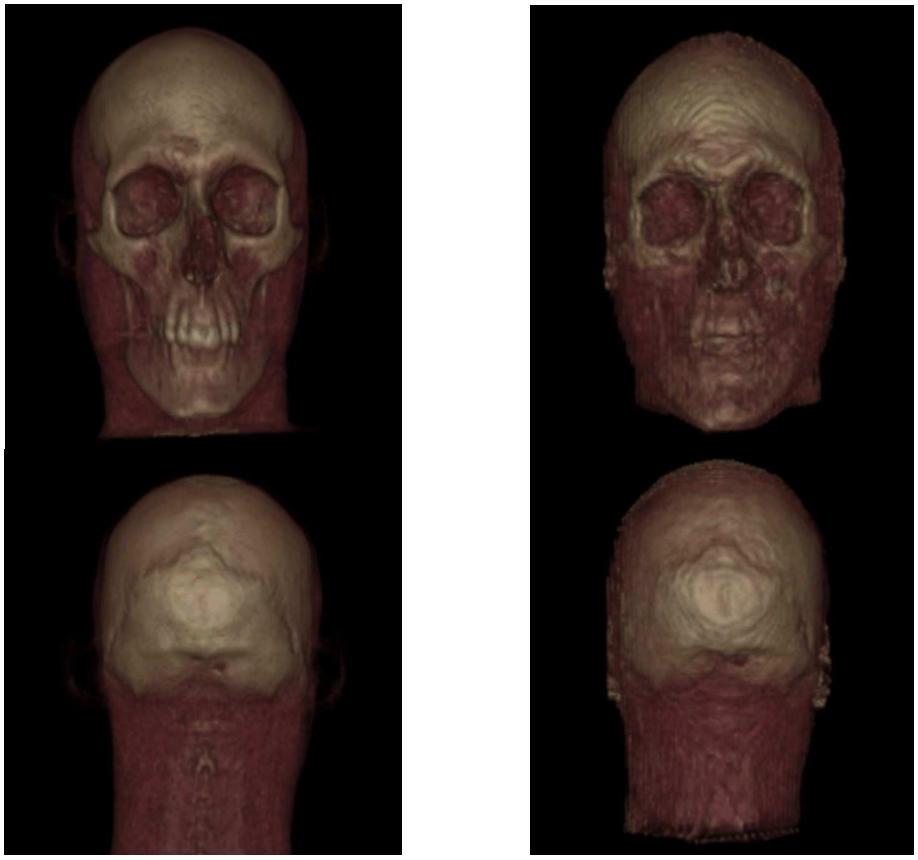

(a) (b)

Figure 3.7: (a) Skull renderings of the CT and (b) the corresponding pseudoCT for the same patient for both the front and back side of the head. The pseudoCTs bear a good similarity to the CT for most part of the head, except for dental regions where there was an absence of sufficient signal in UTE-TE1.

omitted such regions and consequently these were labeled as air. Overall, the pseudoCTs emulate the patient CTs especially in regions comprising of soft-tissue and cortical bone. However, at very challenging areas in the head, such as the ear and nasal regions, an accurate HU was not predicted. This is because the very fine bone structures in the ear and nasal regions are classified as air during air mask derivation. Figure 3.7 shows a comparison of skull renderings of the CT and the pseudoCT for the same patient. The pseudoCT was successful in capturing the hard cortical bone structures in most parts of the head and bore a high similarity to the CT.

3.3.3 Whole-body attenuation maps

An accurate MR to CT mapping is a prerequisite for optimal model training. This is not straightforward to achieve even for an intra-patient whole-body scenario due to inherent physiological motion and different patient configurations (arms up in PET/CT, arms down in PET/MR). To circumvent this problem, we reuse the model generated for head studies on other stations, assuming that the classifier generalization holds good.

First, a manual thresholding procedure was used for creating an initial mask followed by a morphological closing operation to generate an air mask. The voxels inside the mask were assigned continuous HU values calculated by the ϵ-SVR. The volunteers were scanned using the same acquisition protocols as described for head studies with no acquired emission data. The estimated pseudoCT is shown in Figure 3.8. However, a drawback with the UTE sequence used here, is the limited FOV: 300×300 mm^2. In voxels beyond these regions, where there is an absence of UTE signal, the model predicts water/fat intensities from the 3-D Dixon sequence. This setting allows to assign cortical bone LACs when possible or at least water/fat otherwise.

3.4 Discussion

A method to generate pseudoCTs via ϵ -SVR is presented. The approach used two MR sequences, UTE sequences that are capable of visualizing cortical bone and 3-D Dixon-VIBE sequences that contain fat and water information. After establishing a voxel-to-voxel correspondence between the reference CT and MR datasets through image registration, the regression model was trained to learn the intensity mapping between the two modalities. For any new patient MR data, the algorithm framework performs an air mask segmentation followed by a prediction of fat, water and cortical bone intensities on a continuous scale within this mask. In that sense, the

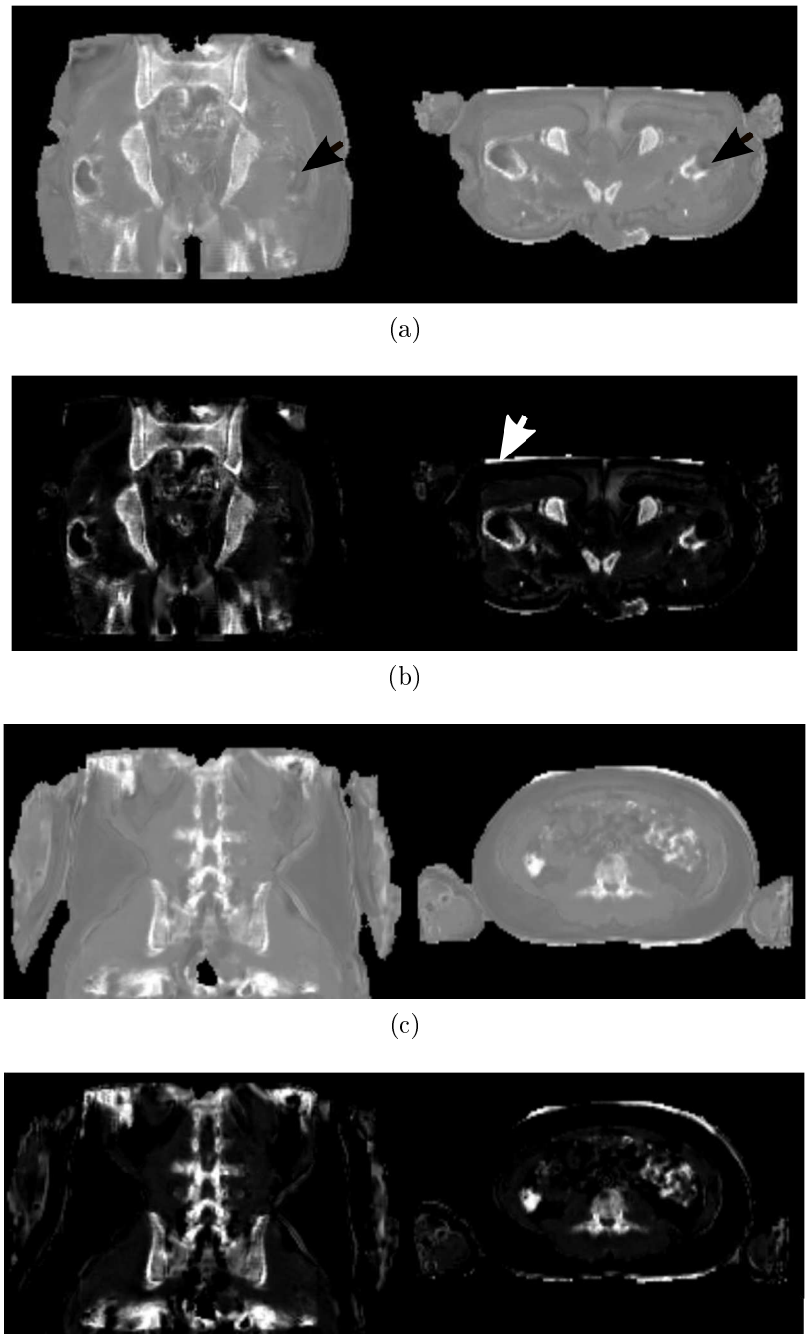

(a)

(b)

(c)

(d)

Figure 3.8: (a, c) Coronal and transaxial views of MR predicted CT using the same model in thorax and pelvis as for brain studies. (b, d) Window/level adjusted views for the same volunteer. The regression model predicts cortical bone where both UTE and 3-D Dixon information is available or simply water/fat in the absence of UTE intensities (black arrows). Some voxels were misclassified as bone due to oversegmentation by the masking procedure (white arrow).

proposed framework is beneficial for predicting pseudoCTs for patients that do not have a pre-acquired CT.

76.23% of the air voxels were found to correctly classified in the air regions bounded by the VOIs. An accurate air classification was limited to the following reasons. The UTE-TE1 contains high noise. This is because the FID is sampled right after the RF excitation as described in Section 2.3. Also, the susceptibility artifacts become predominant at the air- soft tissue interfaces. Nevertheless, a high degree of similarity was observed in regions consisting of hard cortical bone. This can be appreciated from Figure 3.7.

Besides the use in PET, the pseudoCTs can motivate investigation for replacing CT for attenuation correction in hybrid imaging systems such as SPECT/CT wherein imaging multiple radiopharmaceuticals like Technetium-99 (Tc-99m) or Iodine-131 (^{131}I) are prevalent. While initial results in SPECT/MR technical integration have already been reported, certainly an MR based pseudoCT generation for AC seems promising [Hama 10].

Lastly, the generated model can be reused on other body regions. Figure 3.8 shows initial results where the pelvic and spinal bone discrimination is seen and could be of potential benefit for whole-body PET AC. However, in the current study, a limitation of the UTE sequences was the reduced FOV of 300×300 mm^2 . Extending the FOV and thereby ensuring acceptable image quality would therefore be beneficial in moving forward MR-based pseudoCTs for whole-body applications.

3.5 Conclusion

In this study, the feasibility of generating continuous valued CT-like attenuation maps from UTE and 3-D Dixon sequences has been demonstrated. A less than two minute acquisition time makes the proposed approach promising for PET-AC in hybrid PET/MR imaging.

Chapter 4

Evaluation of MR based PET Attenuation Correction

Parts of this chapter contains work and results published in the following article Bharath. K. Navalpakkam, Harald Braun, Torsten Kuwert and Harald H. Quick "Magnetic resonance-based attenuation correction for PET/MR hybrid imaging using continuous valued attenuation maps", Investigative Radiology, Vol. 48, No. 5, pp. 323–32, May 2013.

4.1 Introduction

Accurate PET quantification is important from a clinical perspective. There exist many data corrections that are applied starting from recording the emission sinogram to reconstructing the final PET image. At each stage, uncertainties in restoring true PET activities may be introduced due to various approximations in above mentioned corrections. As discussed in Chapter 2, attenuation and scatter form two main sources of errors that may degrade the PET activities, if not adequately addressed. With this objective, it was demonstrated in the previous chapter that a realistic CT-like attenuation map generation is feasible from MR data alone. The goal of this chapter is to evaluate these attenuation maps for PET-AC. Within the PET/MR community, many of the proposed attenuation correction algorithms have been evaluated against a segmented CT for studies of the head. The inherent drawback of such an assumption is that cortical bone being a hard medium requires several classes for an adequate representation. Thus, a secondary goal of this study is to investigate if this assumption is adequate. This is achieved by comparing the PET volumes reconstructed with segmented CT

versions with the continuous valued CT attenuation maps that were introduced in the previous chapter.

4.2 Material and Methods

The patient data addressed in the previous chapter is used here. In short, ten patients were included in this study and all of these patients had ^{18}F-FDG injected as a radiotracer. In this chapter, the remaining patients that were allocated for model testing purposes are utilized. These were originally left out in the training step. For each of the five patients, a pseudoCT is generated using the introduced pipeline and this is then compared against different variants of attenuation maps.

4.2.1 Attenuation Maps Compared

Four μ-maps were generated:

- Patient CT (μ-map$_{\mathrm{CT}}$)
- ϵ-SVR predicted CT (μ-map$_{\mathrm{MR}}$)
- Three class segmented CT (μ-map$_{\mathrm{bone}}$)
- Three class Dixon like μ-map from CT (μ-map$_{\mathrm{nobone}}$).

The first two (μ-map$_{\mathrm{CT}}$ and μ-map$_{\mathrm{MR}}$) were converted to PET energy (511 keV) by hybrid scaling and the third (μ-map$_{\mathrm{bone}}$) was threshold-ed into air (HU$<$-300), soft tissue (-300$\leq$HU$<$300) and bone (HU$\geq$300) and LACs of 0 cm^{-1}, 0.100 cm^{-1} and 0.151 cm^{-1} were assigned respectively. μ-map$_{\mathrm{bone}}$ was constructed by assigning 0 cm^{-1} , 0.0854 cm^{-1} and 0.100 cm^{-1} from thresholding CT into air (HU$<$-300), fat (-300$\leq$HU$<$0) and water (HU$\geq$0), respectively [Kina 03]. Figure 4.2 shows the different μ-maps used for comparison.

The rationale behind performing a comparison against the above mentioned μ-maps is as follows:

1. μ-map$_{\mathrm{CT}}$ consists of continuous HU for air, cortical bone, fat and soft-tissue regions. Transmission scans are considered as a reference for PET-AC, but in the absence of which, a scaled CT to PET energy has been widely accepted as a reference. Also, the current generation of PET/CT hybrid imaging systems routinely employ a CT based AC via a bilinear scaling strategy to attenuation correct the PET data.

From this standpoint, μ-map$_{\mathrm{CT}}$ can be considered an ideal standard for comparison.

2. μ-map$_{\mathrm{MR}}$ closely emulates μ-map$_{\mathrm{CT}}$ and we derive them from MR sequences alone, as described previously. These contain continuous HU for cortical bone, fat and soft-tissue. Three main reasons for considering continuous HU are as follows.

   - The histogram for the cortical bone class in a patient CT occupies a wide range on the HU scale (300-2000 HU). Translated to 511 keV they occupy (0.131-0.171 cm^{-1}). These variation must therefore be carefully accounted for.

   - The grey matter is very closely surrounded by the cortical bone shell. Incorrect bone HU may therefore bias activities close to this region.

   - Tumors are but abnormal growth and therefore appear in the fat/soft-tissue class. A realistic approach would require continuous LACs for these classes. Also, any calcification present in the brain regions may be inaccurately misclassified as a soft-tissue. This in turn biases the PET quantification.

3. μ-map$_{\mathrm{bone}}$ consists of four different LAC values in total for air, cortical bone, fat and soft-tissue. As already pointed out previously, such attenuation maps are considered as the silver standard.

4. μ-map$_{\mathrm{nobone}}$ is included to analyze the effect of ignoring cortical bone in the attenuation map. This is motivated from the fact that, the current manufacturers' implementations of μ-maps that are used regularly in the clinical routine in most of the current PET/MR hybrid imaging systems utilize this variant for PET-AC. Therefore, the μ-map$_{\mathrm{nobone}}$ is considered in order to emulate the current product μ-maps.

The Table 4.1 shows an overview on the attenuation maps compared. The complete PET-AC pipeline is shown in Figure 4.1

4.3 Evaluation

4.3.1 Reconstruction Parameters and Evaluation of Quantification

Attenuation corrected PET data reconstructed from the above mentioned μ-maps will be referred to as PET$_{\mathrm{CTAC}}$, PET$_{\mathrm{MRAC}}$, PET$_{\mathrm{boneAC}}$ and PET$_{\mathrm{noboneAC}}$

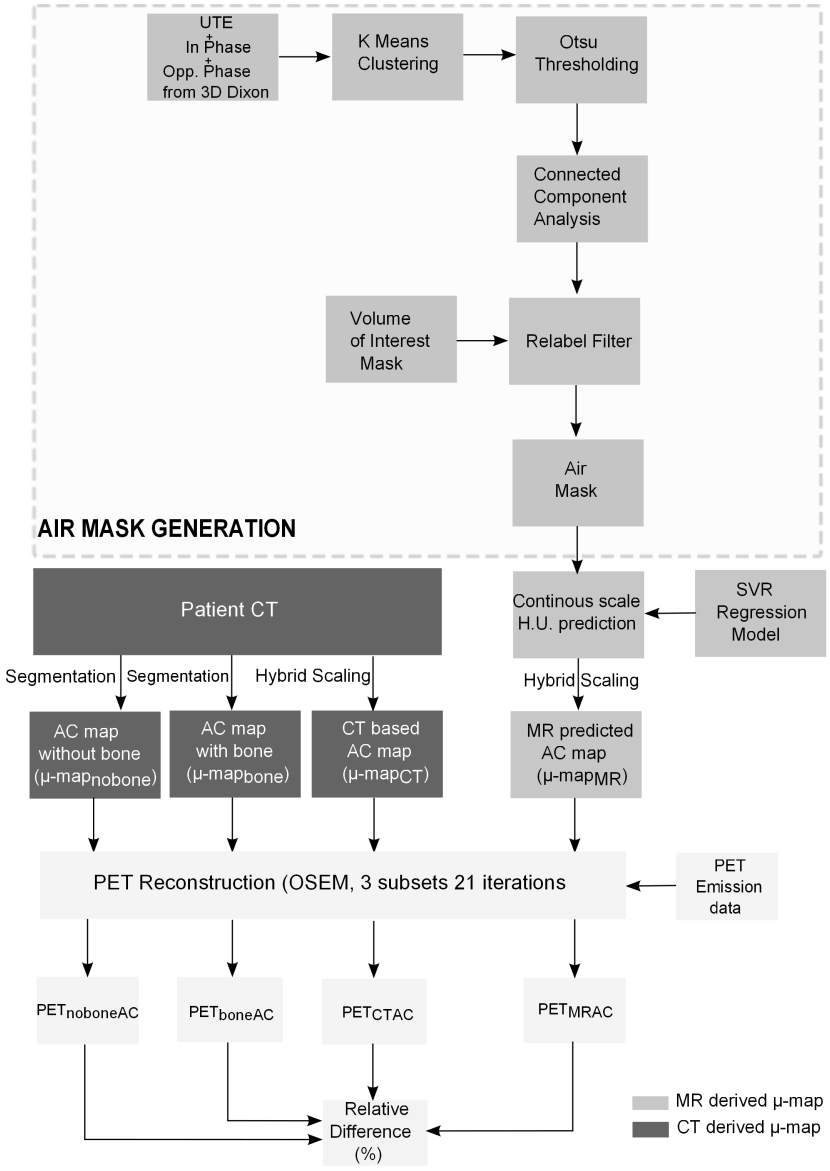

Figure 4.1: PET attenuation correction pipeline. μ-map$_{\mathrm{MR}}$ is derived from MR sequences. From the patient CT, three sets of μ-maps are derived μ-map$_{\mathrm{CT}}$, μ-map$_{\mathrm{bone}}$ and μ-map$_{\mathrm{nobone}}$. The corresponding PET reconstructions are PET$_{\mathrm{CTAC}}$, PET$_{\mathrm{boneAC}}$, PET$_{\mathrm{noboneAC}}$. PET$_{\mathrm{MRAC}}$ is obtained from μ-map$_{\mathrm{MR}}$. For each reconstruction, a relative difference image is calculated against PET$_{\mathrm{CTAC}}$ as the reference. The patient CT is only used for model training and evaluation and is not needed when predicting continuous valued μ-maps for a new patient.

Modality	Abbreviation	Number of Classes	LACs (cm^{-1})
CT	μ-map$_{\mathrm{CT}}$	continuous	0-0.1700
MR	μ-map$_{\mathrm{MR}}$	continuous	0-0.1700
CT	μ-map$_{\mathrm{bone}}$	4	0, 0.0854, 0.1000, 0.1510
CT	μ-map$_{\mathrm{nobone}}$	3	0, 0.0854, 0.1000

Table 4.1: Overview of different attenuation maps and their assigned LAC coefficients at 511 keV [Cata 10]

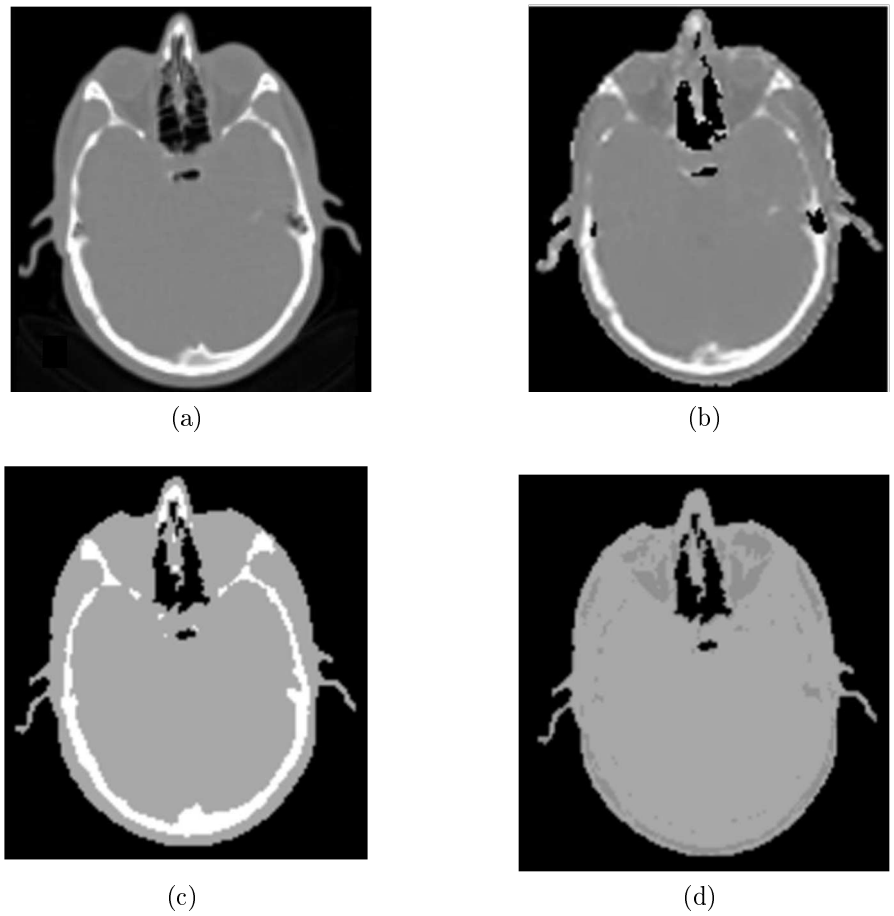

(a) (b) (c) (d)

Figure 4.2: Different attenuation maps used for comparison for PET-AC. Transaxial slices of patient P3 (A) Patient CT: μ-map$_{\mathrm{CT}}$ (B) MR predicted CT: μ-map$_{\mathrm{MR}}$ (C) Four class segmented CT: μ-map$_{\mathrm{bone}}$ (D) Three class Dixon like CT: μ-map$_{\mathrm{nobone}}$

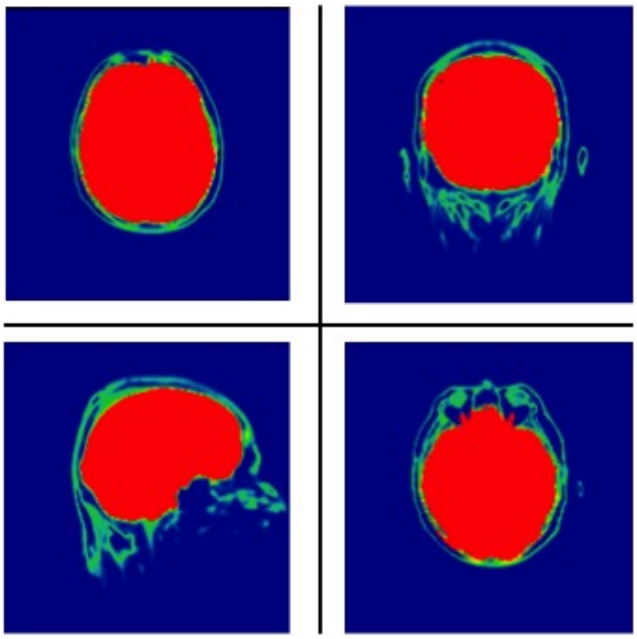

Figure 4.3: Segmentation of the complete brain (regions in red) from 3-D Dixon-VIBE images. This served as the basis for evaluating global PET differences reconstructed from the different μ-map variants for PET-AC.

respectively. All reconstructions were performed on the Biograph mMR console with standard settings: Ordered Subset Expectation Maximization with 3 subsets, 21 iterations, post smoothed with a 4 mm full width at half maximum Gaussian low pass filter with enabled scatter correction. Two kinds of evaluations were performed to analyze the impact of the μ-maps on the PET-AC reconstructions. These are as follows:

- **Global analysis**: The complete brain was segmented from UTE-TE2 and 3-D Dixon-VIBE opposed-phase images for the purpose of analyzing global PET quantification differences between the reconstructed results. The result of a whole brain segmentation is shown for a sample patient in Figure 4.3.

- **Local analysis**: In order to analyze local PET uptake differences across PET-AC from different μ-maps, thirteen landmarks close to the cortical bone were segmented on the basis of GM regions. All segmentations were performed using the software IBASPM [Alem 06].

Furthermore, relative difference (RD) images between PET reconstructions from different μ-maps against the gold standard PET_{CTAC} were calculated using the following relation

$$\alpha(x,y,z) = 100 \times \frac{PET_i(x,y,z) - PET_{CTAC}(x,y,z)}{PET_{CTAC}(x,y,z)} \tag{4.1}$$

Here i represents different μ-maps i.e μ-map$_{\mathrm{CT}}$, μ-map$_{\mathrm{MR}}$, μ-map$_{\mathrm{bone}}$ and μ-map$_{\mathrm{nobone}}$. Besides, a linear regression analysis with the following relation $y = mx+c$ was performed, where x and y denote the activities from PET$_{\mathrm{CTAC}}$ and PET$_{\mathrm{MRAC}}$, PET$_{\mathrm{boneAC}}$ and PET$_{\mathrm{noboneAC}}$ respectively.

4.4 Results

4.4.1 Global and Local PET analysis

Exemplary transaxial slices of the RD volumes for PET reconstructions are shown in Figure 4.4. From a qualitative standpoint, both PET$_{\mathrm{MRAC}}$ and PET$_{\mathrm{CTAC}}$ are in good agreement. No misleading or artifactual uptake spots were introduced by the algorithm. Quantitatively, a constant underestimation is observed for PET$_{\mathrm{noboneAC}}$ for all patients (red coloration) due to cortical bone omission. For 3 out of 5 patients, PET$_{\mathrm{boneAC}}$ resulted in small underestimations within 3% (light red coloration) due to the lower LAC for water 0.1000 cm^{-1} in μ-map$_{\mathrm{bone}}$ in contrast to μ-map$_{\mathrm{CT}}$.

The global error difference on PET due to different attenuation maps is seen in Table 4.2. Table 4.3 shows the results of PET quantification for regions close to cortical bone for all reconstructions. The exclusion of cortical bone resulted in noticeable underestimations for PET$_{\mathrm{noboneAC}}$ that produced a global error of $10.15 \pm 3.31\%$ and $11.03 \pm 2.26\%$ error close to cortical bone. On the other hand, the overestimations due to constant LAC for cortical bone in μ-map$_{\mathrm{bone}}$ translated to a local overestimation error of $4.22 \pm 3.91\%$ close to bone but had no severe global impact ($3.64 \pm 3.71\%$) as the nature of these local errors decreased with increasing distance from the soft tissue and cortical bone interface. PET$_{\mathrm{MRAC}}$ was able to estimate PET activities with an error of $2.40 \pm 3.69\%$ for the brain regions and $2.16 \pm 1.77\%$ for regions close to cortical bone. A large mean and standard deviation for PET$_{\mathrm{boneAC}}$ for the segmented landmarks in Table 4.3 demonstrate the variability in the LAC assignment close to skull. Errors reported were averaged across all patients and are in absolute units.

Considering the proximity of GM to the skull, the effect of segmented μ-maps on PET quantification and the benefit of using continuous density assignments can be seen in Figure 4.5. The proposed method minimizes these estimation errors at the skull periphery in contrast to over 10% errors for PET$_{\mathrm{noboneAC}}$ and 4% errors for PET$_{\mathrm{boneAC}}$. The overestimation errors can

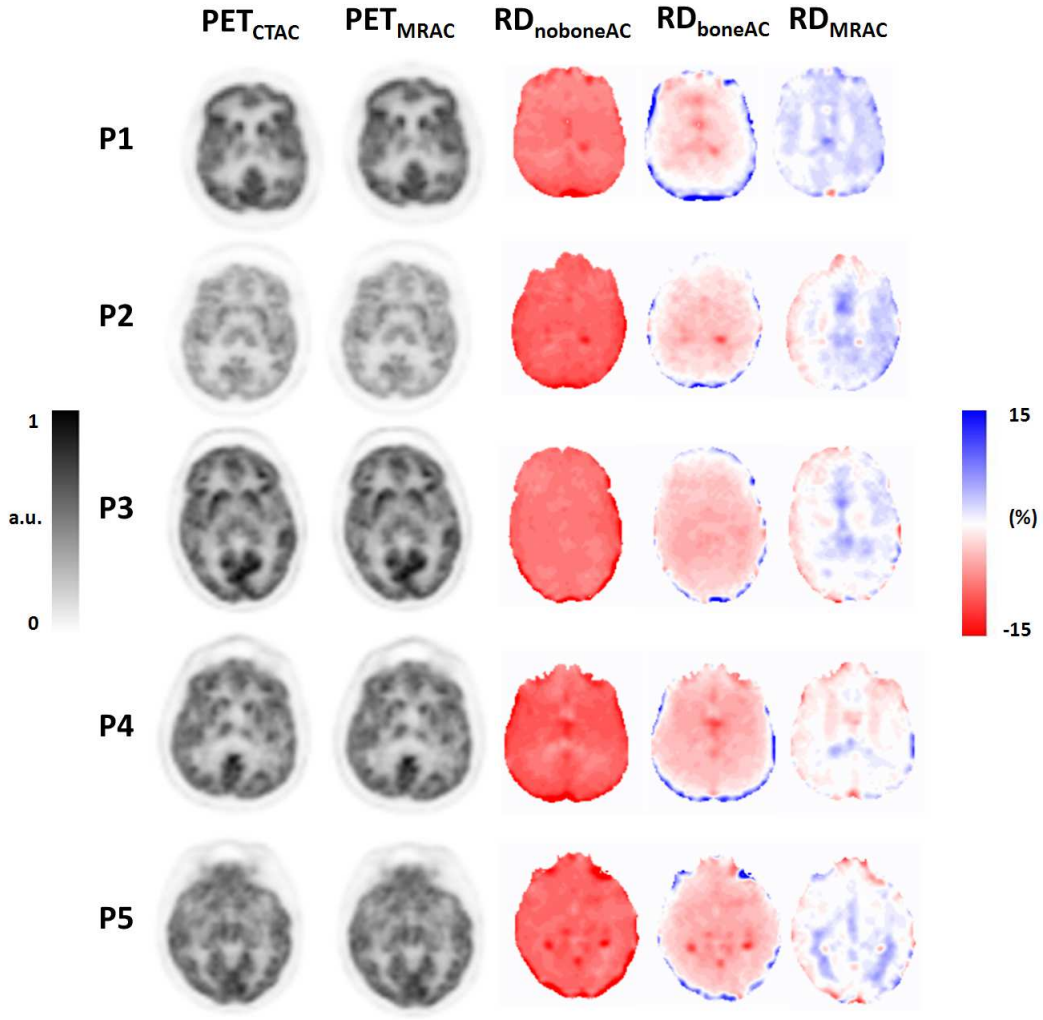

Figure 4.4: PET volumes and their respective relative difference maps reconstructed from different attenuation maps. Visually, $\mathrm{PET}_{\mathrm{MRAC}}$ compares well with $\mathrm{PET}_{\mathrm{CTAC}}$. $\mathrm{PET}_{\mathrm{MRAC}}$ compares with $\mathrm{PET}_{\mathrm{CTAC}}$ with an error of 2.40 $\pm$ 3.69% for the entire brain and 2.16 $\pm$ 1.77% for regions close to cortical bone. Red and blue colorations indicate under- and overestimation errors respectively.

Patients	RD_{MRAC} (mean ± stdev)	$RD_{noboneAC}$ (mean ± stdev)	RD_{boneAC} (mean ± stdev)
P1	2.84 ± 4.18	10.25 ± 3.62	4.22 ± 3.62
P2	2.18 ± 3.29	10.48 ± 4.02	4.43 ± 4.60
P3	2.42 ± 3.21	10.75 ± 2.84	3.57 ± 4.00
P4	2.26 ± 4.29	9.22 ± 3.08	3.56 ± 2.82
P5	2.28 ± 3.48	10.05 ± 2.98	4.03 ± 3.44
Mean	2.40 ± 3.69	10.15 ± 3.31	3.64 ± 3.71

Table 4.2: PET quantification differences on the complete brain for all five patients. All values are in percent (%)

be thought of bone intra-class misclassifications where the assigned LAC is offset by a large degree compared to the actual value in the CT.

A scatter plot of PET activities with calculated regression lines for all the voxels encompassed by the segmented landmarks is shown in Figure 4.6. PET_{MRAC} has a near perfect unity slope (1.012) compared to $PET_{noboneAC}$ (0.918) or PET_{boneAC} (0.961) indicating that the proposed method has the potential to estimate PET activities accurately with respect to the gold standard. Table 4.4 shows the corresponding coefficient of determination (R^2) and regression coefficients.

As a side note, for a patient not included in this study due to a different injected tracer, the proposed approach was able to predict calcifications in the brain regions. Figure 4.7 shows the comparison between MR predicted CT and the patient CT.

Figure 4.8 shows the fusion of an ^{18}F-FDG PET_{MRAC} overlaid on an anatomical T_2-Turbo Spin Echo. The conjunction of high soft tissue contrast from the MR is seen with functional information from PET.

4.5 Discussion

In this work, the pseudoCTs introduced in the previous chapter were evaluated for PET AC. The evaluation was done for the μ-map_{MR} against different attenuation maps comprising of scaled CT (μ-map_{CT}), segmented CT with cortical bone (μ-map_{bone}), and segmented CT without cortical bone (μ-map_{nobone}). PET_{MRAC} compare well both qualitatively and quantitatively to the other approaches (Figure 4.4). Figure 4.6 suggests that a continuous valued pseudoCT generation from MR sequences is feasible for head studies and is in better agreement to the gold standard μ-map_{bone} than the 3-class approach that is used in the current generation of PET/MR systems.

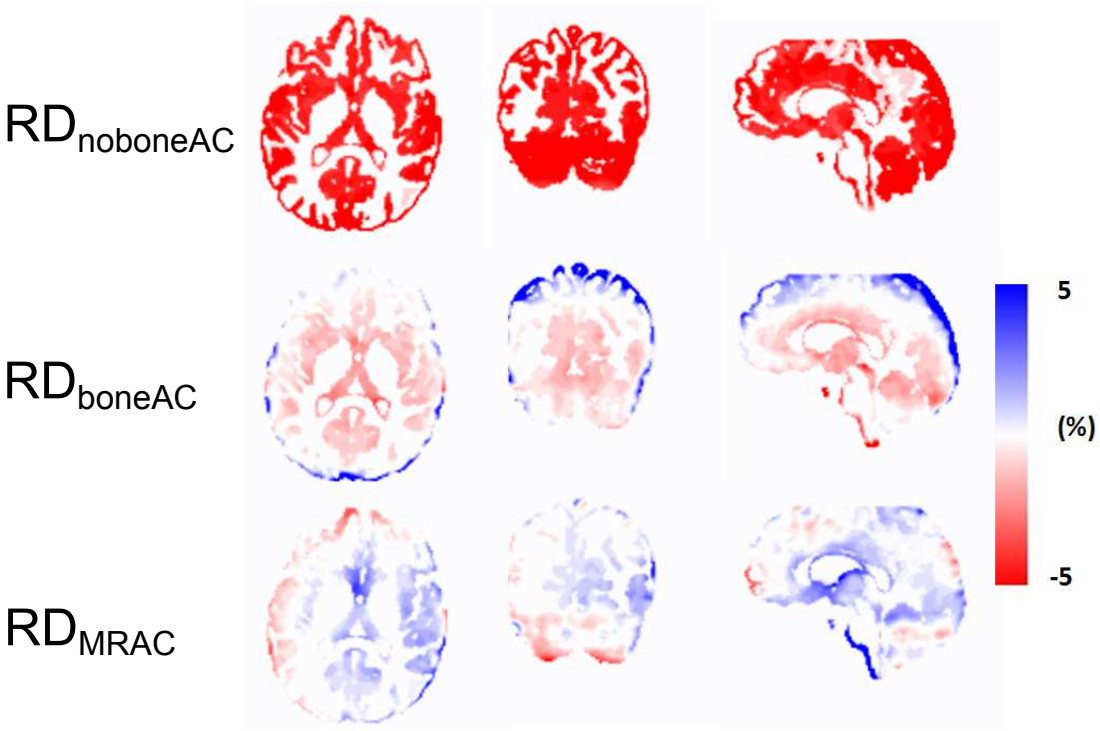

Figure 4.5: Effect of segmentation based attenuation maps on PET-AC for patient P2. Illustration shows the relative difference maps on GM regions (compared to gold standard) from (top row): $\mathrm{PET}_{\mathrm{noboneAC}}$, (middle row): $\mathrm{PET}_{\mathrm{boneAC}}$ and (bottom row) $\mathrm{PET}_{\mathrm{MRAC}}$. A consistent error $> 11\%$ (underestimation) at the periphery of the skull in $\mathrm{PET}_{\mathrm{noboneAC}}$ and $> 4\%$ (overestimation) in $\mathrm{PET}_{\mathrm{boneAC}}$ has been improved in $\mathrm{PET}_{\mathrm{MRAC}}$ due to continuous bone density prediction. Red and blue colorations indicate under- and overestimation errors respectively.

Landmarks	RD_{MRAC} mean ± stdev	$RD_{noboneAC}$ mean ± stdev	RD_{boneAC} mean ± stdev
Angular gyrus LR	2.35 ± 1.97	10.88 ± 2.28	4.79 ± 4.65
Cuneus LR	2.49 ± 1.17	11.17 ± 2.86	4.07 ± 4.21
Inferior frontal gyrus	2.25 ± 1.94	9.97 ± 2.14	3.80 ± 4.35
Middle frontal gyrus LR	1.84 ± 1.50	10.28 ± 1.60	3.88 ± 3.45
Middle occipital gyrus LR	2.24 ± 1.73	12.13 ± 2.70	4.72 ± 3.65
Occipital lobe LR	3.45 ± 2.64	15.10 ± 3.20	6.07 ± 4.65
Postcentral gyrus LR	1.97 ± 1.61	10.59 ± 2.00	4.43 ± 4.35
Precentral gyrus LR	2.19 ± 1.70	10.17 ± 2.12	3.85 ± 4.55
Superior frontal gyrus LR	1.55 ± 1.19	9.78 ± 1.55	3.66 ± 2.19
Superior occipital gyrus LR	1.83 ± 1.43	12.58 ± 3.04	5.38 ± 5.37
Superior parietal lobule LR	1.32 ± 1.16	10.81 ± 2.42	3.72 ± 3.86
Superior temporal gyrus LR	2.30 ± 1.72	9.84 ± 1.57	2.87 ± 1.79
Supramarginal gyrus LR	2.63 ± 2.67	10.09 ± 1.80	3.61 ± 3.71
Mean	**2.16 ± 1.77**	**11.03 ± 2.26**	**4.22 ± 3.91**

Table 4.3: Summary of PET activity differences on segmented regions across all patients and for all PET reconstructions. In general, PET_{MRAC} estimates PET activities more accurately to PET_{CTAC} than any other method. All values are in percent (%). LR here indicates the left and right orientations.

Coefficients	PET_{MRAC}	$PET_{noboneAC}$	PET_{boneAC}
m	1.012	0.918	0.961
c	-0.062 ± 0.002	-0.193 ± 0.003	0.0324 ± 0.004
R^2	0.994 ± 0.218	0.972 ± 0.425	0.961 ± 0.527

Table 4.4: Results of linear regression analysis on PET activities from the investigated attenuation maps. All values are in mean ± stderr.

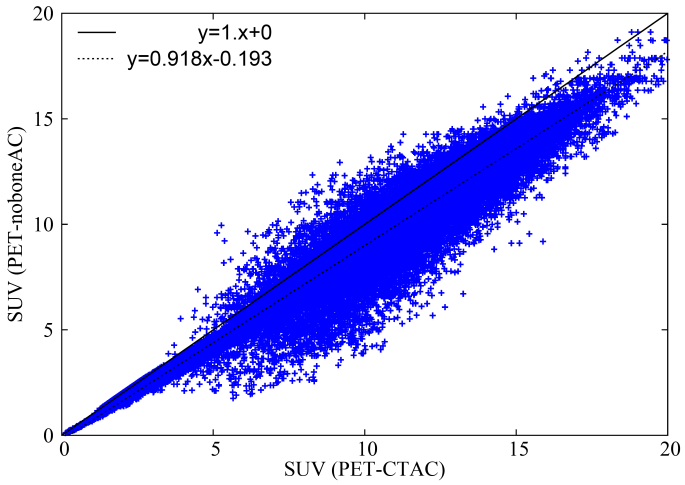

(a)

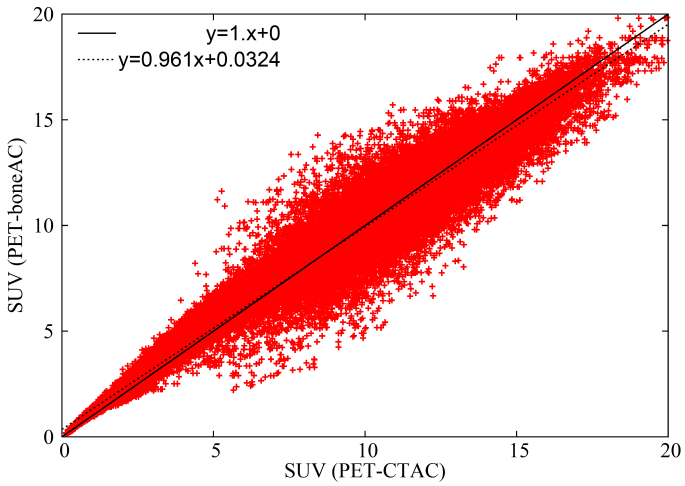

(b)

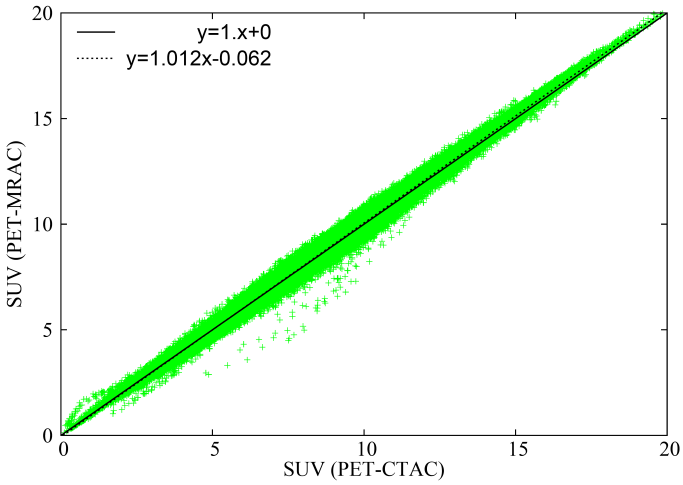

(c)

Figure 4.6: Scatter plots from $\mathrm{PET}_{\mathrm{noboneAC}}$, $\mathrm{PET}_{\mathrm{boneAC}}$, $\mathrm{PET}_{\mathrm{MRAC}}$ with respect to $\mathrm{PET}_{\mathrm{CTAC}}$ as reference for all patients. Comparatively, $\mathrm{PET}_{\mathrm{MRAC}}$ has a closer to identity slope than any other method.

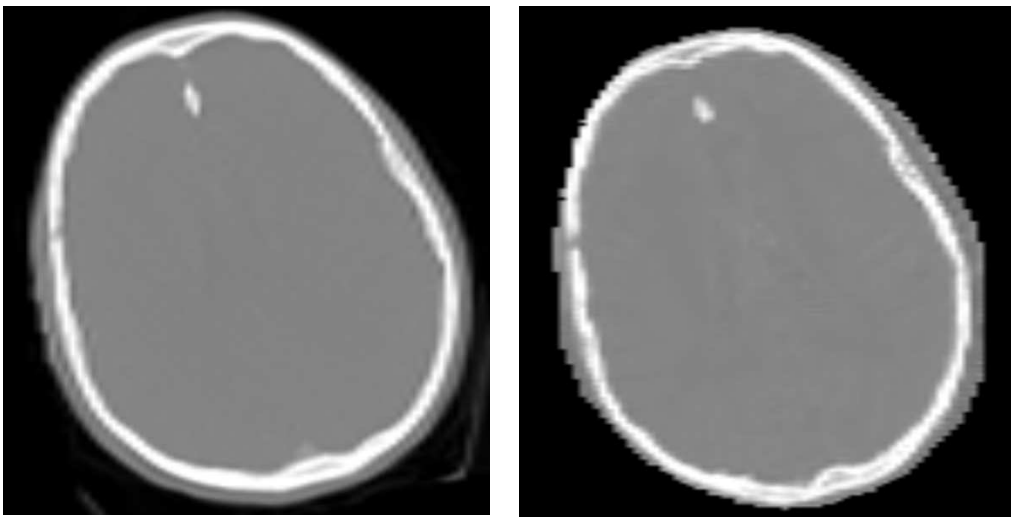

(a) (b)

Figure 4.7: MR predicted CT (A) is able to identify calcifications in the brain (black arrow) in comparison to patient CT (B).

Since head is a more compact region and cortical bone is a highly attenuating medium, it requires a careful LAC assignment for accurate PET quantification. In this context, UTE sequences have already been used for the purpose of attenuation correction. Keereman et al. and Catana et al. propose segmentation based approaches based on UTE for PET-AC and compare their results to a segmented CT [Cata 10], [Keer 10]. While μ-map$_{\text{bone}}$ has no significant global influence on PET quantification, it yields regionally increased uptakes close to the skull periphery (Figure 4.5). μ-map$_{\text{MR}}$ minimizes this bias. However, a classifier training across a larger patient collective would be useful for obtaining accurate results.

Similarly, for both small and large VOIs, PET$_{\text{noboneAC}}$ underestimated activities by at least 10% consistently across all patients. This decrease is also in agreement with errors 10%-15% underestimation reported by Schramm et al. [Schr 13], Samarin et. al. [Sama 12] and Catana et al. [Cata 10], reiterating the inclusion of a cortical bone class when deriving μ-maps. Although, cortical bone exclusion can be generally accepted for whole body studies, its application has limitations towards neurological studies [Schu 11], [Mart 09].

The following limitations were observed while deriving the attenuation maps. During mask generation, the air mask omitted fine structures at the ethmoid sinus and parts of the middle ear cavities (mastoid air cells and tympanic cavities). Although no global impact was observed, the effect of this

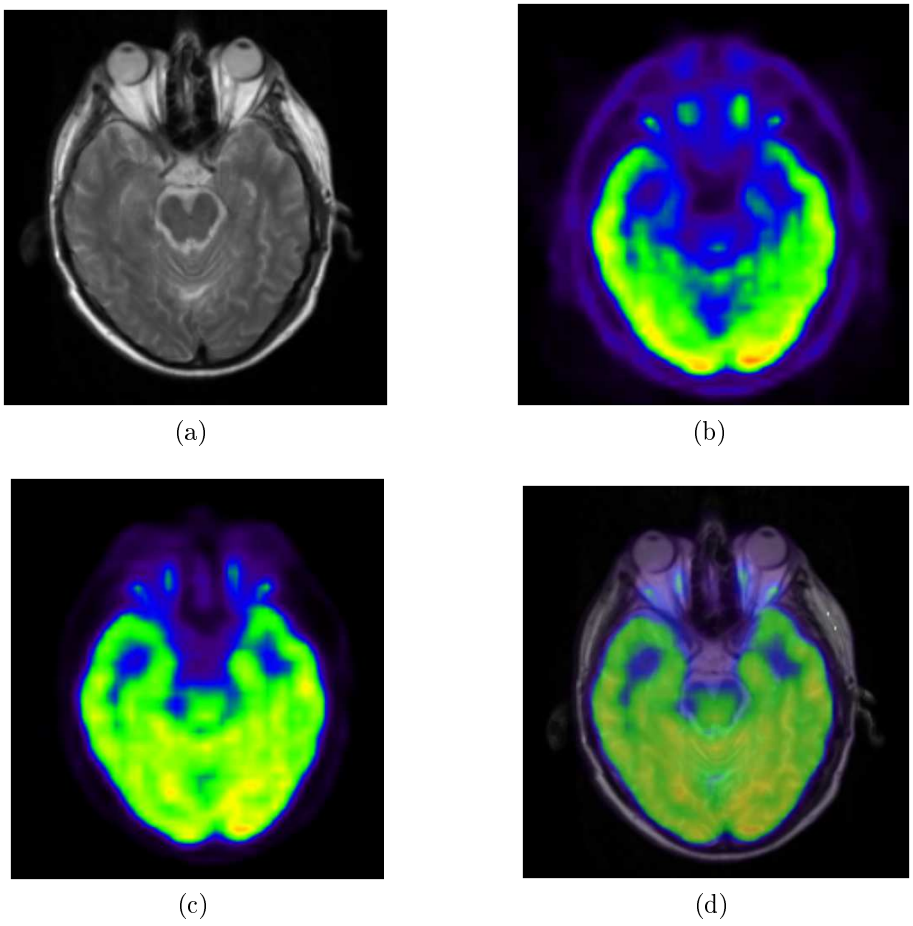

(a) (b)

(c) (d)

Figure 4.8: (a) Anatomical T_2-Turbo Spin Echo sequence, (b) non-attenuation corrected PET, (c) PET_{MRAC}, (d) fused PET/MR (c) overlaid on (a)

misclassification led to error variations of up to 30% in the adjacent structures. As an improvement, multiple UTE sequences with different acquisition parameters (e.g. flip angle, TE) can also be used [Joha 11]. This could give more T_2^* information per voxel that could result in better model generalization. However, with this approach it is not clear as to which HU would the classifier predict for very fine tissues, given the susceptibility artifacts. Also, patient acquisition times and motion are its biggest limitations.

Not included in this study were also regions below the nose where we expect high uncertainties due to e.g.. differences in tongue, swallowing and uvula positions. This may introduce a potential bias for PET comparisons. Also ignored were the dental regions and implants where a CT is unlikely to serve as a sufficient reference due to metal streak artifacts.

For older patients, local spots of under-estimation were observed due to calcifications in the brain, for $\mathrm{PET}_{\mathrm{boneAC}}$ reconstruction. This resulted in RD of 5%-10% due to its local assignment as a soft tissue (0.1000 cm^{-1}) in $\mu\text{-map}_{\mathrm{bone}}$. The proposed method underestimated PET activities with the same error range, as the regression model estimated soft-tissue HU for these regions. This was because, in patient P4, the UTE sequence was not sensitive enough to image the small calcifications. In the patient CT, this region corresponded to less than 200 HU. However, in another patient, not included in this study, the calcifications were predicted by the model and also their corresponding intensities were greater than 500 HU in the patient CT. This can be seen in Figure 4.7.

4.6 Conclusion

In this chapter, we evaluated the accuracy of different μ-maps for PET-AC. The proposed MR-based μ-map estimates PET activities better than any segmentation based approach. Excluding cortical bone for PET-AC leads to an underestimation effect in the order of 10% error range.

Chapter 5

Impact of MR-based Attenuation Correction Methods on Patients with ^{18}FDG-PET Brain Hypometabolism

5.1 Introduction

In oncologic whole-body imaging applications, numerous initial clinical studies have shown that the diagnostic potential of PET/MR is at least comparable to that of PET/CT hybrid imaging [Wies 13], [Drze 12], [Quic 13]. It is foreseen that the field of neurology and, in particular, the diagnosis of dementia and Alzheimer's disease (AD) would benefit significantly from simultaneous PET/MR hybrid imaging [Cata 12] especially when targeted radiotracers are used [Beck 13], [Bart 11], [Fris 13], [Duka 11]. For these patients, indications of PET hypometabolism in relevant anatomical brain sections assist in differentiating AD from non-AD patients. In this context, achieving an accurate PET quantification in specific brain regions plays an important role in AD diagnosis and MR imaging may provide additional anatomical and functional brain tissue information [Beck 13], [Duka 11].

Several MR-based AC methods were discussed in the Chapters 3 and 4. A clinical adoption of the proposed MR-based AC methods, however, requires an evaluation on patients with a neurological indication. Numerous research groups have investigated PET activity differences on healthy brain volunteers resulting from the MR-based and their corresponding CT-based μ-maps [Cata 10], [Schr 13], [Malo 11], [Nava 13c]. Only a limited number

of groups have evaluated their MR-based AC methods on specific patient groups with neurological indications [Keer 10], [Hofm 08], [Lars 13].

Two objectives are thus addressed in this study. First, an evaluation of current standard MR-based μ-maps on PET quantification accuracy for ^{18}F-FDG hypometabolic patients is performed. Second, the PET quantification improvement achieved using the proposed UTE and 3-D Dixon-VIBE sequence based regression method that incorporates continuous cortical bone LACs for PET-AC is investigated. For both evaluations, the CT-based AC available for all patients was considered as the standard of reference.

5.2 Material and Methods

The data used in this study were acquired on an integrated PET/MR system (Biograph mMR, Siemens AG, Healthcare Sector, Erlangen, Germany). The hybrid system allows for simultaneous PET and MR measurements. A detailed technical description of the system is provided in [Dels 11] and is discussed in Section 2.4.1.

5.2.1 Patient Examination

Sixteen patients (six females, ten males) with a mean age of 54.3 $\pm$ 15.7 years (range: 18-78 years) and mean weight of 74.8 $\pm$ 14.8kg (range: 54-112 kg), were included in this study. All of them were injected with ^{18}F-FDG as radiotracer. This also includes the patient population that were utilized in the previous chapter for training the SVM regressor. This regression model was obtained from the PET/CT and PET/MR data pairs from ten out of the sixteen patients that were referred to hybrid imaging because of a non-neurological oncologic whole-body examination. These patients are referred to as the training group. These are referred to as "hypometabolism" group and had a mean ^{18}F-FDG dose for these patients was 202.3 $\pm$ 10.6 MBq. The remaining six out of the sixteen patients were examined for ^{18}F-FDG PET hypometabolism indications in the brain and received a higher ^{18}F-FDG dose. They had a mean dose of 368.4 $\pm$ 21.5 MBq. The PET findings for these six patients is shown in Table 5.1. Four of six patients had a clinical history of objective memory problems, one had a suspected cerebritis and the other patient had a progressive cognitive impairment. The PET findings for the six patients indicated ^{18}F-FDG hypometabolism. All 16 patients were examined on a PET/CT scanner followed by a PET/MR examination. Patients from the training group were examined on a Siemens Biograph Truepoint 64 PET/CT scanner (Siemens AG, Healthcare Sector, Erlangen, Germany)

while the hypometabolic group underwent a PET/CT scan on a Siemens Biograph mCT 40 (Siemens AG, Healthcare Sector, Erlangen, Germany). For the CT acquisition, the X-ray tube current was 165 mA, peak tube voltage of 120 kVp, 512 x 512 image matrix size and a H19s convolution kernel. The PET/MR examination for both patient groups was performed on a Siemens Biograph mMR (Siemens AG, Healthcare Sector, Erlangen, Germany) approximately two hours post injection. No MR-contrast agents were injected for any of the patients. An approval from the Institutional Review and Ethical Board was obtained for patient examinations. All patients were informed of the scientific study and they gave their written consent.

5.2.2 CT-based Attenuation Map

Since, the CT and MR volumes were acquired on two different scanners, they need to be brought to the same geometrical space. This is done by registering the CT dataset to the UTE-TE1 volume using a rigid transform. The mutual information similarity metric was maximized and a cubic B-spline function was used to interpolate intensity values at non-integer voxel positions. As optimizer, a gradient descent approach was selected. The background intensities in the transformed CT images were assigned a value of -1024 HU during image resampling. Further, a head mask was obtained by applying a morphological closing kernel on the UTE-TE1 volume. The head mask covered regions from the tip of the head to the neck but was then cropped to the nose. This way, the artifacts caused due to dental implants that were visible on the MR images and the corresponding AC maps were partially eliminated from consideration. The cropped mask was then resampled to match the UTE volume resolution. In order to remove patient head holder, foam and other aids present in the CT image, the cropped mask was multiplied voxelwise with the CT dataset. The resulting CT image was transformed to 511 keV energy using the hybrid scaling approach [Kina 03]. The CT-based AC map (ACmapCT) was then used as a reference for PET comparisons.

5.2.3 MR-based Attenuation Maps

Two MR-based AC maps were compared; 1) The current 3-D Dixon-VIBE sequence derived μ-map - ACmapDix and 2) The AC map generated from UTE and 3-D Dixon-VIBE sequences.

Patients	PET examination findings	Age (years)	Sex	Height (m)	Weight (kgs)	Activity injected (MBq)	Body Mass Index (kg/m^2)
P1	Severe PET hypometabolism in bilateral frontal, temporal and parietal regions. Relatively sparing hypometabolism in basal ganglia	66	M	1.82	95	365	28.68
P2	Mild PET hypometabolism in bilateral anteromedial temporal lobes. Very mild parietal hypometabolism	61	F	1.67	61	359	21.87
P3	Progressive cognitive impairment	78	M	1.82	81	366	24.25
P4	Clinically suspected cerebritis, moderate occipital lobe hypometabolism, mild bilateral parietal, medial temporal lobe hypometabolism	18	F	1.67	54	370	20.43
P5	Hypometabolism in bilateral frontal lobes, caudate nuclei, bilateral parietal, temporal lobes, anterior and posterior cingulate gyrus	66	M	1.72	112	370	37.85
P6	Hypometabolism in bilateral temporal and parietal lobes	72	M	1.75	68	379	25.90

Table 5.1: Patient demographics and PET examination outcomes.

ACmapDix

The standard Dixon-VIBE derived ACmapDix was generated from the 3-D Dixon-VIBE sequences by the PET/MR system software "VB18" version. The MR acquisition parameters for this sequence are described in Section 4.2. ACmapDix contained LACs of 0 cm^{-1}, 0.1000 cm^{-1} and 0.0854 cm^{-1} for air, water/soft tissue and fat classes, respectively. Most importantly cortical bone class was ignored and was replaced with the LAC value for soft tissue (0.1000 cm^{-1}). The ACmapDix used here is different from the one described in Chapter 4, in which case it was derived directly from the patient CT.

ACmapUTEDix

The pseudoCT generation procedure for this work is similar to the one described in Chapter 3 [Nava 13c]. However, a difference to the former is that a model training/validation is performed on a larger patient collective (n=10) for this study. A five-fold cross validation procedure is carried out to estimate the kernel parameters. The pseudoCTs are then converted to 511 keV AC maps (ACmapUTEDix) using a hybrid scaling mapping [Kina 03] and contain continuous LACs for fat, water and cortical bone classes.

5.2.4 PET Reconstruction and Evaluation

The PET reconstructions were performed using e7-tools (Siemens Molecular Imaging, USA). For all AC maps the RF head/neck coil based AC map was added retrospectively to the generated human AC maps by the reconstruction software. Following this, the ACmaps were downsampled to PET resolution and subsequently Gaussian filtered. The PET emission data acquired from the PET/MR imaging system was reconstructed three times for each of the six patients using 1) ACmapCT 2) ACmapDix and 3) ACmapUTEDix to yield PET_{CTAC}, PET_{DixAC} and $PET_{UTEDixAC}$ and volumes respectively. A 3-D OP-OSEM maximization algorithm with 3 iterations, 21 subsets was used for all PET reconstructions with scatter correction. The reconstructed PET images had an image size of 172×172×127 with a resolution 4.173×4.173×2.031 mm^3 and were smoothed with a Gaussian filter using a 4 mm kernel at full width at half maximum.

A similar evaluation procedure as in Chapter 3 is followed here. For the brain analysis, the 3-D Dixon-water data for all patients was segmented into three separate brain structures; GM, WM and CSF using the software IBASPM [Alem 06]. The three images were then added and an empirical threshold was selected to yield a binary segmented brain volume. The idea

Patients	PET_{DixAC} (mean ± std dev)	$PET_{UTEDixAC}$ (mean ± std dev)
P1	18.83 ± 6.32	3.50 ± 4.70
P2	13.46 ± 4.23	3.17 ± 3.02
P3	8.18 ± 3.78	4.25 ± 4.50
P4	28.49 ± 4.97	3.20 ± 3.62
P5	12.26 ± 7.62	7.14 ± 11.12
P6	14.32 ± 4.53	5.13 ± 4.97
Mean	**15.92 ± 5.24**	**4.39 ± 5.32**

Table 5.2: Absolute relative errors for the whole brain for PET reconstructed using ACmapDix and ACmapUTEDix compared against ACmapCT. All values are in percent (%)

behind using a binary segmented brain was to include all the voxels inside of this mask for PET evaluation. In order to measure PET activity differences in hypometabolic brain regions from the resulting ACmapDix and ACmapUTEDix reconstructions, the 3-D Dixon-water data was further segmented into 28 anatomical structures using a T_1-weighted atlas MR image. The clinical report for the patients indicated ^{18}F-FDG hypometabolism in either frontal, temporal, parietal, occipital or basal ganglia regions. Therefore, depending on their location, the anatomical structures were grouped into mentioned five brain regions and PET quantification differences were evaluated based on them. Further, relative differences (RD) to PET_{CTAC} were computed for both PET_{DixAC} and $PET_{UTEDixAC}$.

RD images indicate deviations in PET activities in PET_{DixAC}, $PET_{UTEDixAC}$ against ground truth PET_{CTAC}. Besides that in order, to analyze the differences in activity distributions resulting from different AC map based PET reconstructions, two kinds of histograms calculated from the RD images were generated for regions 1) inside of the segmented binary brain data and 2) segmented anatomical brain regions.

5.3 Results

16 patients referred to PET/CT and subsequent to PET/MR hybrid imaging in this study, 10 PET/CT and PET/MR data doublets of patients not showing ^{18}F-FDG hypometabolism in the brain were used for training of the method for MR-based AC map generation. The method was then applied to the PET/MR datasets of 6 out of 16 patients that had a clinical indication for Alzheimer's disease or other dementia disease and showed ^{18}F-FDG hy-

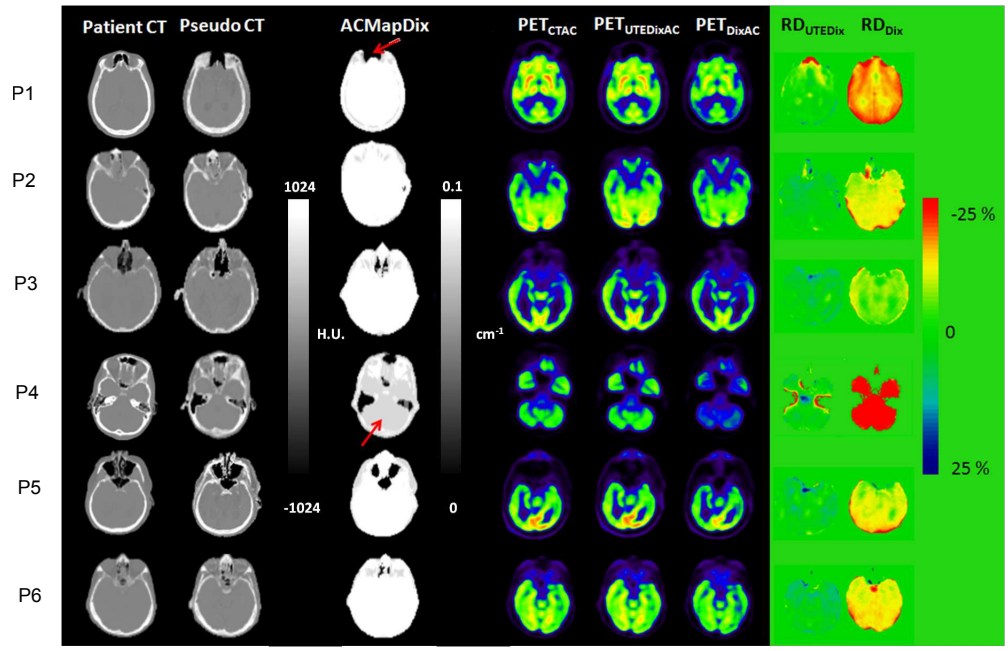

Figure 5.1: Representative slices from patient CT, pseudoCT prior to AC map conversion, ACmapDix, their respective PET reconstructions and relative difference images across all six patients. Generally, $\mathrm{PET}_{\mathrm{UTEDixAC}}$ outperforms $\mathrm{PET}_{\mathrm{DixAC}}$ based results and this can be confirmed from the $\mathrm{RD}_{\mathrm{UTEDix}}$ and $\mathrm{RD}_{\mathrm{Dix}}$ images. AC maps for two patients were suboptimal (red arrows). In patient P1, due to partial volume effect, the complete head is not segmented in ACmapDix. This translated to 18% underestimation errors for P1. Maximum deviation in quantification over 25% was observed for a patient P4 that had fat LAC (0.0854 cm^{-1}) assigned for water voxels and vice-versa ($\mathrm{RD}_{\mathrm{Dix}}$ in fourth row).

pometabolism. The corresponding patient CT, pseudoCT, ACmapDix, their respective PET reconstructions and RD slices in axial orientation for all six patients are shown in Figure 5.1.

The $\mathrm{RD}_{\mathrm{Dix}}$ images suggest that $\mathrm{PET}_{\mathrm{DixAC}}$ considerably underestimates activities compared to $\mathrm{PET}_{\mathrm{UTEDixAC}}$. A quantitative evaluation of PET radiotracer activity differences for the complete brain for both ACmapDix and ACmapUTEDix is presented in Table 5.2. A large mean absolute error of 15.92% $\pm$ 5.24% across all patients for ACmapDix based PET reconstructions was noted. This was mainly because of the absence of cortical bone in ACmapDix based PET reconstructions. In contrast, when cortical bone was estimated from UTE and 3-D Dixon-VIBE sequences, the errors were reduced to 4.39% $\pm$ 5.32% .

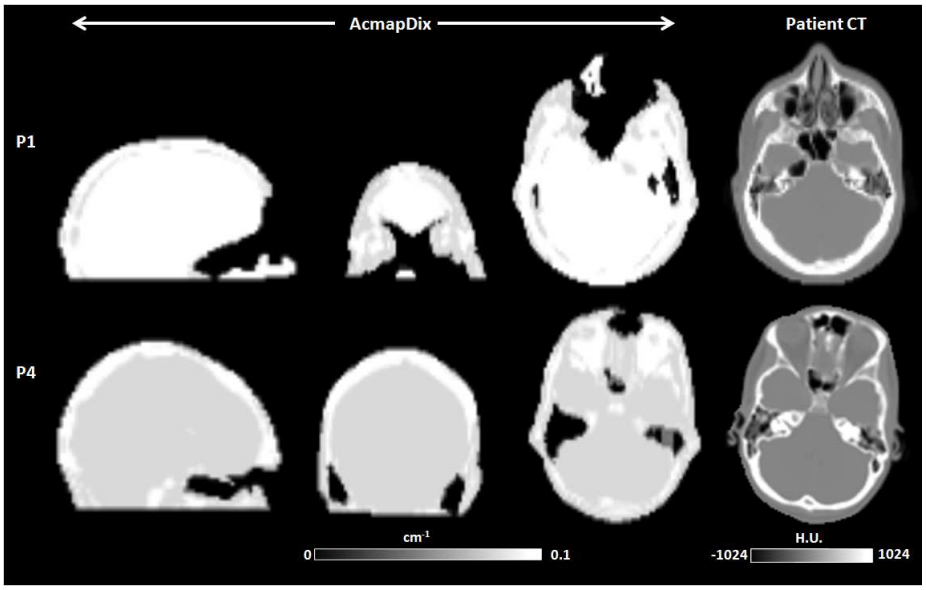

Figure 5.2: Anomalies in AC map generation for two patients shown in sagittal, coronal and axial orientations alongside patient CT. In patient P1, a dental implant caused severe local signal degradation that propagated onto the corresponding AC map. ACmapDix in patient P4 had inverted water/fat LAC values (water: 0.1000 cm^{-1}, fat: 0.0854 cm^{-1}).

The AC maps for two out of the six patients showed noteworthy anomalies, indicated by relatively large errors in the resulting difference images as shown in Figure 5.1.

Patient P1 had a metallic dental implant that resulted in MR signal loss around the dental/nasal region. In the corresponding ACmapDix, soft tissues in this region were substituted as air. Despite image cropping, the AC map appeared incomplete in this patient. For a different patient P4, the LAC values for water and fat were flipped in the standard AC maps based on the Dixon only sequence. Figure 5.2 shows the AC maps for these two patients in detail.

The ACmapDix for patient P4 consequently had incorrect LAC assignments for fat and water voxels and the LAC for fat (0.0854 cm^{-1}) is lower than that of water (0.1000 cm^{-1}) at 511 keV. Therefore, a combined effect of cortical bone omission and fat/water LACs flipping led to a severe underestimation of 28.49% $\pm$ 4.97% for this specific patient (Figure 5.2).

Anatomical Brain Regions	Frontal Lobe (mean ± std dev)	Temporal Lobe (mean ± std dev)	Occipital Lobe (mean ± std dev)	Parietal Lobe (mean ± std dev)	Basal Ganglia (mean ± std dev)
P1	20.98% ± 4.89%	20.89% ± 5.04%	19.76% ± 4.36%	19.50% ± 3.00%	17.41% ± 2.47%
P2	13.99% ± 3.01%	13.30% ± 5.20%	14.49% ± 4.52%	15.01% ± 2.60%	11.14% ± 0.65%
P3	8.53% ± 2.39%	9.40% ± 2.98%	7.24% ± 2.08%	6.98% ± 2.27%	8.42% ± 0.69%
P4	26.50% ± 2.98%	28.73% ± 3.96%	25.63% ± 3.07%	26.19% ± 2.96%	32.34% ± 1.33%
P5	12.86% ± 5.01%	11.38% ± 3.57%	12.11% ± 4.98%	13.67% ± 2.29%	8.17% ± 1.21%
P6	15.79% ± 3.15%	13.72% ± 2.97%	14.32% ± 2.45%	14.89% ± 2.23%	12.13% ± 0.80%
Mean	**16.44% ± 4.09%**	**16.23% ± 3.95%**	**15.59% ± 3.57%**	**16.04% ± 2.55%**	**14.93% ± 1.91%**

Table 5.3: Absolute relative errors for $\text{PET}_{\text{DixAC}}$ for anatomical brain regions.

Anatomical Brain Regions	Frontal Lobe (mean ± std dev)	Temporal Lobe (mean ±std dev)	Occipital Lobe (mean ± std dev)	Parietal Lobe (mean ± std dev)	Basal Ganglia (mean ± std dev)
P1	4.25% ± 4.61%	3.71% ± 4.09%	2.89% ± 2.89%	2.16% ± 2.16%	5.43% ± 2.91%
P2	2.26% ± 1.88%	4.47% ± 5.56%	2.42% ± 2.14%	2.48% ± 1.57%	4.37% ± 0.89%
P3	4.05% ± 2.36%	3.82% ± 3.81%	2.43% ± 1.96%	3.89% ± 2.18%	3.13% ± 1.35%
P4	1.96% ± 1.80%	2.87% ± 2.97%	2.26% ± 1.84%	2.31% ± 2.23%	2.47% ± 1.41%
P5	3.31% ± 2.74%	4.21% ± 4.34%	3.27% ± 3.64%	2.50% ± 2.02%	2.82% ± 2.50%
P6	3.34% ± 3.06%	4.87% ± 2.87%	3.52% ± 1.87%	3.56% ± 2.11%	5.26% ± 2.02
Mean	**3.19% ± 2.74%**	**3.99% ± 3.96%**	**2.46% ± 2.39%**	**2.79% ± 2.04%**	**3.91% ± 1.84%**

Table 5.4: Absolute relative errors for $\text{PET}_{\text{UTEDixAC}}$ for anatomical brain regions.

The distribution of the relative difference errors for the brain region for all reconstructions for both PET_{DixAC} and $PET_{UTEDixAC}$ is shown in Figure 5.3. The histograms in conjunction with Figure 5.1 and Table 5.2 visually and quantitatively further confirm the underestimation effect in PET activity estimation when cortical bone is ignored (PET_{DixAC}). Comparatively, the inclusion of continuous cortical bone intensities results in reduced PET activity errors that are less than a 10% mean error ($PET_{UTEDixAC}$).

Six out of 16 patients analyzed in this study exhibited radiotracer hypometabolism in either frontal, temporal, parietal, occipital lobes or basal ganglia regions. The relative difference errors for these five anatomical brain regions observed in PET_{DixAC} is shown in Table 5.3, while the corresponding results for $PET_{UTEDixAC}$ is shown in Table 5.4. For PET_{DixAC}, the mean absolute relative difference errors across all brain regions was found to be 16%. Similar to the errors in the complete brain, the effect of flipping fat/water LACs in case of patient P4 led to over 25% errors for all the segmented anatomical brain regions. For the same regions, $PET_{UTEDixAC}$ was able to reconstruct PET activities with an error of only 3.26% $\pm$ 2.59 % when compared to CT-based AC as standard of reference. The histograms for RD_{Dix} and RD_{UTEDix} for the anatomical brain regions for all patients is illustrated in Figure 5.4A and Figure 5.4B, respectively. The means and standard deviations for all the histogram distributions for RD_{UTEDix} are well within $\pm$10%, thereby demonstrating the improved PET quantification accuracy for hypometabolic brain regions compared to RD_{Dix}.

The impact of the three different AC map variants on PET reconstructions for a sample ^{18}F-FDG hypometabolic patient P6 is illustrated in Figure 5.5. Visually, PET_{DixAC} shows a significant global reduction in radiotracer distribution within the brain. As a consequence, this underestimation effect is also reflected on the bilateral temporal and parietal hypometabolic regions for this patient that may hamper diagnosis in a clinical setting.

5.4 Discussion

In this PET/MR hybrid imaging study, the impact of three different attenuation correction methods on neurological patients that showed ^{18}F-FDG hypometabolism in the brain was evaluated. The first AC map was a product based standard MR-based AC map that ignored cortical bone in PET/MR imaging of the head. The second MR-based AC map included continuous LACs for cortical bone by means of an epsilon-insensitive support vector regression method from a combination of 3-D Dixon-VIBE and UTE sequences.

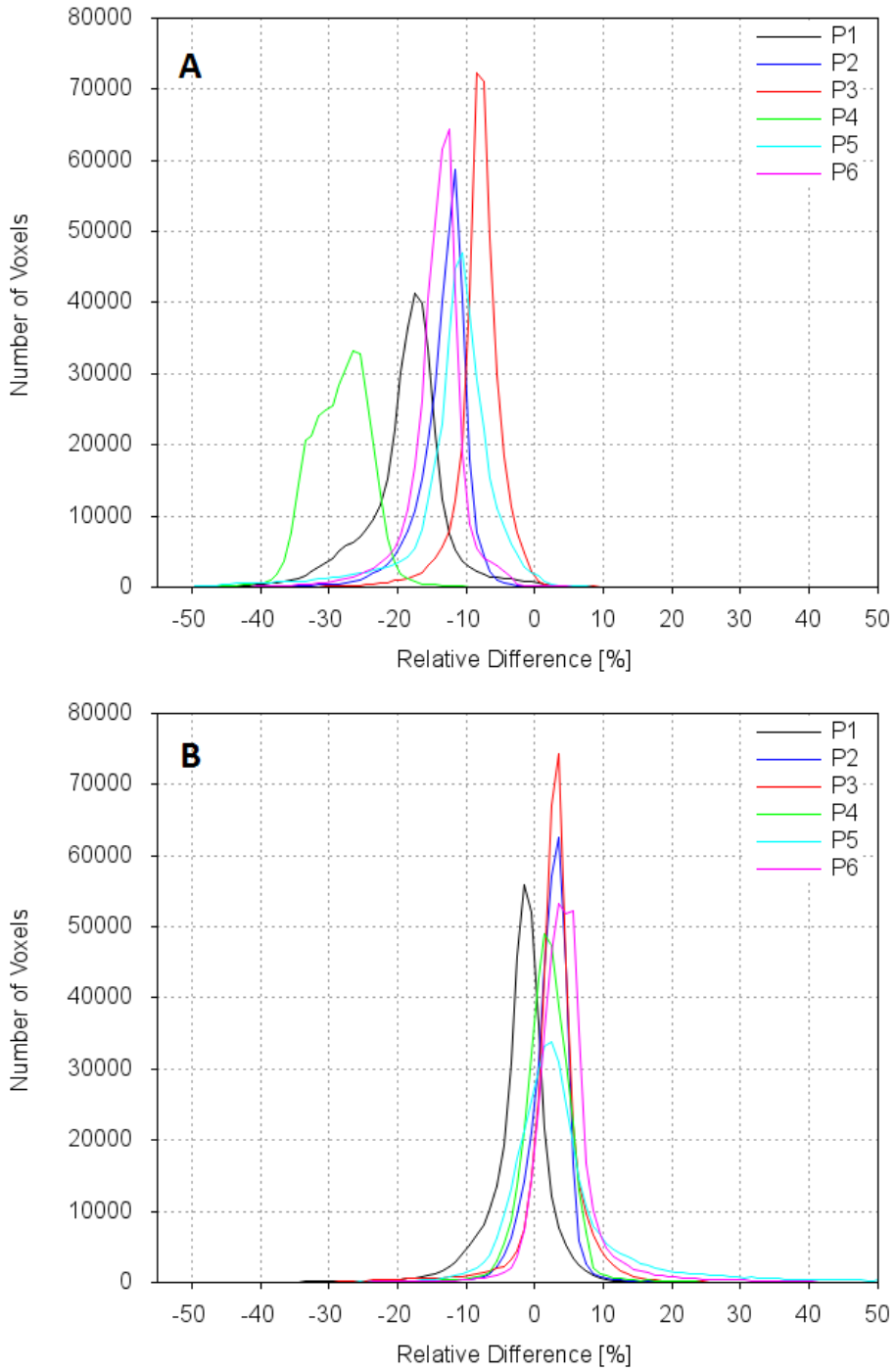

Figure 5.3: Histograms of relative difference errors for the complete brain for A) $\mathrm{PET}_{\mathrm{DixAC}}$ and B) $\mathrm{PET}_{\mathrm{UTEDixAC}}$ when compared to the standard of reference. Note the bias in ACmapDix based PET reconstructions in A). These errors are reduced when continuous cortical bone LACs are incorporated in B). Consequently, the histograms of all patients in $\mathrm{PET}_{\mathrm{UTEDixAC}}$ B) are much closer to the 0% relative difference line than for $\mathrm{PET}_{\mathrm{DixAC}}$ illustrated in A).

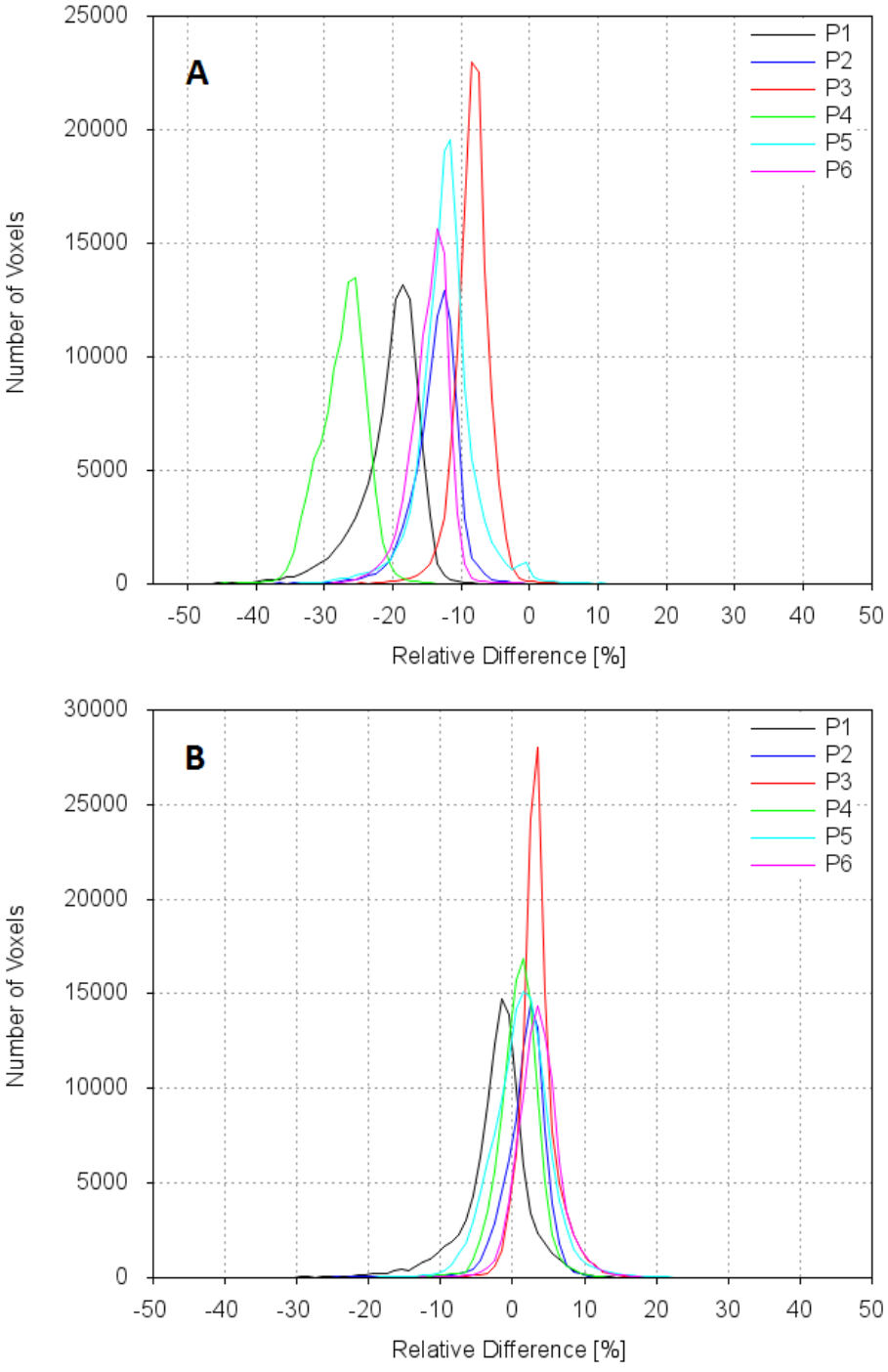

Figure 5.4: Histograms of relative difference errors for the segmented anatomical brain regions (frontal, temporal, occipital, parietal, basal ganglia regions) for A) $\mathrm{PET}_{\mathrm{DixAC}}$ and B) $\mathrm{PET}_{\mathrm{UTEDixAC}}$.

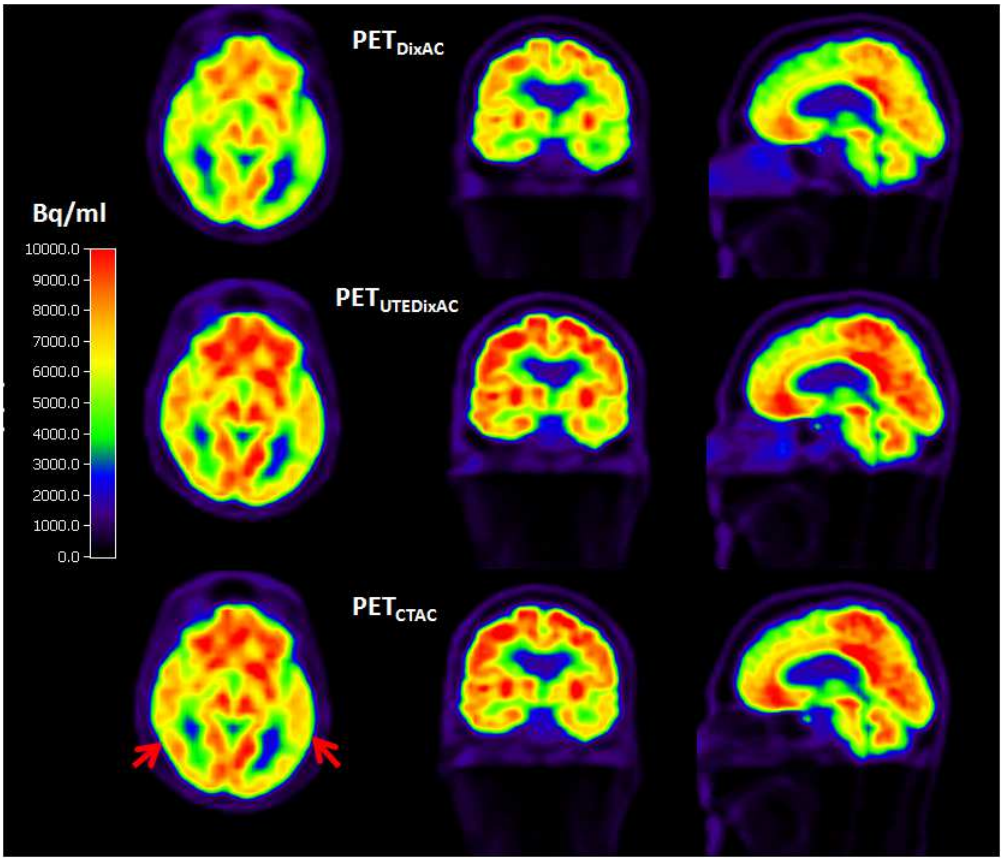

Figure 5.5: Illustration of PET hypometabolism for patient P6 in the bilateral temporal lobes (red arrows) and the effect of PET reconstructions from ACmapDix, ACmapUTEDix and ACmapCT. Note the significant reduction in PET activities in $\mathrm{PET_{DixAC}}$ due to cortical bone exclusion in ACmapDix compared to $\mathrm{PET_{UTEDixAC}}$ and $\mathrm{PET_{CTAC}}$, while $\mathrm{PET_{UTEDixAC}}$ and $\mathrm{PET_{CTAC}}$ as standard of reference visually show very good correlation.

The third AC map was derived from patient CT and was therefore considered as the reference standard.

Quantitative evaluation of PET data reconstruction with all three AC maps revealed a consistent underestimation in PET activities up to an average of 16% when using the ACmapDix for AC. ACmapUTEDix based PET reconstructions were able to estimate PET uptake values with an error of less than 5% (4.39% ± 5.32%) when averaged across all patients and when compared to the CT-based AC as reference standard. The relative difference images in Figure 5.1 and Table 4.4 demonstrate the improved PET accuracy achieved by using ACmapUTEDix over ACmapDix, suggesting that a threefold increase in PET quantification accuracy can be achieved when incorporating cortical bone information.

When considering specific hypometabolic brain regions instead of the whole brain volume, the effect of ignoring cortical bone across all patients also produced a 16% average error across frontal (16.44% ± 4.09%), temporal (16.23% ± 3.95%), occipital (15.59% ± 3.57%), parietal (16.04% ± 2.55%) and basal ganglia regions (14.93% ± 1.91%). In contrast, when cortical bone was included, the error reduced to a mean error of 3.26% ± 2.59% across all anatomical brain regions and all patients.

The effect of excluding cortical bone from the AC map on PET depends largely on the thickness of the cortical bone tissue that the 511 keV photons have to traverse. Recently, Anderson et al. reported 10% to 15% deviations in PET activities when excluding cortical bone for head studies [Ande 14]. The values reported were for patients that underwent a PET/CT examination prior to a PET/MR scan. Under similar patient examination conditions, our own previous study also confirms a 10% underestimation error in patients that had no brain abnormalities [Nava 13c]. Relative difference images from Catana et al. and Samarin et al. also suggest error values in the same range (10%-15%) [Cata 10] [Sama 12].

In order to ensure a fair comparison, a head mask from a high resolution UTE-TE1 (isotropic resolution: 1.56 mm^3) was used to define the volume of interest for all three AC maps. However, the MR-based segmentation in ACmapDix is prone to partial volume effects since it is based on a segmentation method into 4 different tissue classes from a low resolution 3-D Dixon-VIBE sequence (2.6 x 2.6 x 3.12 mm^3). The effect was pronounced in patient P1, where soft-tissue to air misclassification was observed circumferentially around the head. As a result the head mask appeared under-segmented compared to ACmapCT and ACmapUTEDix. This contributed to a mean 19% error for PET_{DixAC} for both complete brain and segmented anatomical regions for patient P1. This explains the reason for a higher error value for PET_{DixAC} for patient P1 in Table 4.4 and Table 5.3.

For the same patient P1, local signal degradation around the nasal/dental regions was noticed in both 3-D Dixon-VIBE and UTE sequences due to the presence of dental implants. Hence, both ACmapUTEDix and ACmapDix suffered from soft tissue to air misclassifications. As a result over 25% errors were observed in the frontal lobe close to the misclassified regions for both $\mathrm{PET_{UTEDixAC}}$ and $\mathrm{PET_{DixAC}}$. This can be seen in $\mathrm{RD_{UTEDix}}$ and $\mathrm{RD_{Dix}}$ slices in Figure 5.2. An atlas comprising of potential artifact affected regions using a combination of MR sequences with short echo times could aid in restoring LACs in implant affected regions [Bezr 13].

In ACmapDix, for patient P4 the LACs for fat (0.0854 $\mathrm{cm^{-1}}$) and water (0.1000 $\mathrm{cm^{-1}}$) were interchanged. A severe underestimation effect >25% was hence observed in the complete brain and segmented anatomical regions. A global loss in counts in $\mathrm{PET_{DixAC}}$ in temporal hypometabolic regions can be seen in Figure 5. Comparatively, $\mathrm{PET_{UTEDixAC}}$ shows potential in restoring PET activities closer to the reference standard $\mathrm{PET_{CTAC}}$. Since a clinical diagnosis for AD is based on accurate ^{18}F-FDG activities in hypometabolic brain regions, anomalies such as water/fat LACs flipping in AC maps (Figure 5.1 and Figure 5.2) should be rectified prior to a clinical interpretation of the reconstructed PET images. One way of doing this is by ensuring that water class is the largest connected component in the generated ACmapDix. If this condition is not met, then an incorrect LAC assignment can be identified and a correct AC map can be obtained by interchanging the fat/water LACs.

5.5 Conclusion

An MR-based method that predicts continuous cortical bone intensities from UTE and 3-D Dixon-VIBE sequences in the context of PET/MR hybrid imaging was evaluated on dementia patients with ^{18}F-FDG hypometabolism in the brain. While the absence of a continuous cortical bone class in current MR-based AC maps amounts to 16% mean errors in the whole brain volume and in radiotracer hypometabolic regions, ACmapUTEDix can accurately restore PET activities with less than 5% mean error in comparison with CT-based AC as standard of reference. This method to improve MR-based AC maps may have impact in clinical PET/MR studies where global and local brain radiotracer activity quantification is of importance such as in Alzheimer's and dementia patients.

Chapter 6

Summary and Outlook

PET/MR hybrid scanners are a relatively new imaging modality. Apart from overcoming the technical challenges in bringing both MR and PET components within each other's vicinity, the question of how to perform PET attenuation correction remains to be carefully addressed. To the PET signal, there exist two main challenges that pose difficulties, namely the attenuation due to hardware and human tissue components. Both these materials, attenuate the PET 511 keV photons differently and hence require suitable correction strategies. Their corrections are equally important for achieving accurate radiotracer quantification. Hardware attenuation correction of rigid MR coils is performed by use of pre-defined CT templates. While, the tissue attenuation correction requires an attenuation map that is as close as possible to the reference standard, which is the patient CT. One way of extracting this information is by using either the PET or MR data. PET, suffers from the problem of having a poor image resolution and limited anatomical information and thus cannot be completely relied upon for this purpose. MR on the other hand seems to be a viable alternative for performing PET attenuation correction, since it provides the possibility of imaging structures with both high soft-tissue contrast and image resolution. Two of the most important tissue classes that require substantial representation in the attenuation maps are cortical bone and air. Standard MR imaging sequences fail to distinguish both of these classes and consequently they appear dark in their respective images.

In this dissertation, we propose a novel framework to generate MR-based attenuation maps for PET attenuation correction. To achieve this purpose, we make use of specialized MR sequences with ultrashort echo times. The so-called UTE sequences thus allow the imaging of tissues with short T_2^* relaxation such as cortical bone. The UTE sequences contain images acquired at two different echo times. In the first echo, the cortical bone and other short

T_2^* structures are visible. These are absent in the second echo image. Thus, both these images aid in distinguishing cortical bone from other tissue types. A conventional approach of embedding this information is by performing a simple segmentation of cortical bone, air and soft-tissue types. The average LACs specific to these tissue classes are then assigned and are used for PET attenuation correction. These attenuation maps are insufficient, because the cortical bone region being the most attenuation structure in the human body, cannot be represented with a single LAC value.

The proposed framework allows for the derivation of continuous valued attenuation maps that include cortical bone as against a limited tissue representation for cortical bone, fat and water classes. Besides using these attenuation maps for PET attenuation correction, a thorough evaluation is performed with respect to the CT-based attenuation correction considered as the reference standard. In addition to this, a comparison of evaluation is performed against segmentation based attenuation maps that either ignore cortical bone (fat, water and air) or include them retrospectively. The first part of the evaluation was carried out on patients that had no clinical indication in the brain but were examined for an abnormality in the rest of the body. The proposed method requires less than 2 minutes for the MR acquisition and does not prolong the overall PET acquisition time of 10 minutes per bed position.

Another drawback with the existing product version based attenuation maps is that they ignore cortical bone. In spite of this shortcoming, they are routinely used in all the clinical installations worldwide for PET reconstruction. In the second part of this thesis, we extend the evaluation of the proposed attenuation maps towards patients having neurological abnormalities. All patients had an known ^{18}FDG PET hypometabolism in the brain region as a clinical question. The evaluation results suggest that the proposed method outperforms the current product standard and the achieved results are found to be in agreement with those in published in the literature.

Several limitations of this study are foreseen. One such is the training of the pseudoCTs on a larger data set which could ensure better model generalization and subsequently assign accurate HU that aid in tissue characterization. Additionally, more sophisticated yet promising features such as Haar features that could be computed in constant time is worth investigating into for generating attenuation maps [Viol 01].

Also, instead of HU, the regression model can be trained to learn the LACs directly. Such a step could bypass the mapping procedure from CT HU to 511 keV.

A high potential for UTE sequences is envisaged for solving myriad of problems related to attenuation correction. Currently, metallic implants such

as dental implants, hip prosthesis and stents pose problems with MR imaging. UTE sequences with its short echo time could aid in near-metal imaging and could assist in MR-based attenuation correction. Besides, the extension of the proposed method towards whole-body attenuation correction with UTE sequences seem promising. This requires ensuring the absence of off-resonance artifacts while extending the UTE FOV. More research is needed in optimizing the sequence in this direction.

List of Figures

List of Tables

List of Acronyms

AC Attenuation Correction

ACF Attenuation Correction Factor

APD Avalanche Photo Diodes

CSF Cerebrospinal Fluid

CT Computed Tomography

FBP Filtered Back Projection

FID Free Induction Decay

FOV Field of View

GM Gray Matter

HU Hounsfield Units

LAC Linear Attenuation Coefficient

LOR Line of Response

LSO Lutetium Oxyorthosilicate

MR Magnetic Resonance Imaging

NAC non-attenuation corrected

PET Position Emission Tomography

PET-AC Positron Emission Tomography-Attenuation Correction

RF Radio Frequency

SPECT Single-Photon Emission Computed Tomography

SUV Standardized Uptake Value

TE Echo Time

TSE Turbo Spin Echo

UTE Ultrashort Echo Time

VOI Volume of Interest

WM White Matter

Bibliography

[Aich 13] A. Aichert, M. Manhart, B. Navalpakkam, R. Grimm, J. Hutter, A. Maier, J. Hornegger, and A. Doerfler. "A Realistic Digital Phantom for Perfusion C-arm CT based on MRI Data". In: *Proc. IEEE NSS MIC*, pp. 1–2, October 2013.

[Akla 13] B. Aklan, D. H. Paulus, E. Wenkel, H. Braun, B. K. Navalpakkam, S. Ziegler, C. Geppert, E. E. Sigmund, A. Melsaether, and H. H. Quick. "Toward simultaneous PET/MR breast imaging: systematic evaluation and integration of a radiofrequency breast coil". *Medical Physics*, Vol. 40, No. 2, p. 024301, February 2013.

[Alem 06] Y. Alemán-Gómez, L. Melie-García, and P. Valdés-Hernandez. "IBASPM: Toolbox for automatic parcellation of brain structures". *Paper presented at the 12th Annual Meeting of the Organization for Human Brain Mapping Florence, Italy. Available on CD-Rom in NeuroImage*, Vol. 27, No. 1, June 2006.

[Ales 06] A. Alessio and P. Kinahan. *PET Image Reconstruction*. Nuclear Medicine. Henkin et al., Philadelphia, Elsevier, second Ed., 2006.

[Ande 14] F. L. Andersen, C. N. Ladefoged, T. Beyer, S. H. Keller, A. E. Hansen, L. Højgaard, A. Kjær, I. Law, and S. Holm. "Combined PET/MR imaging in neurology: MR-based attenuation correction implies a strong spatial bias when ignoring bone". *Neuroimage*, Vol. 84, pp. 206–216, January 2014.

[Avri 00] N. Avril, C. A. Rosé, M. Schelling, J. Dose, W. Kuhn, S. Bense, W. Weber, S. Ziegler, H. Graeff, and M. Schwaiger. "Breast imaging with positron emission tomography and fluorine-18 fluorodeoxyglucose: use and limitations". *Journal of Clinical Oncology*, Vol. 18, No. 20, pp. 3495–3502, October 2000.

[Bai 03] C. Bai, P. E. Kinahan, D. Brasse, C. Comtat, D. W. Townsend, C. C. Meltzer, V. Villemagne, M. Charron, and M. Defrise. "An analytic study of the effects of attenuation on tumor detection in whole-body PET oncology imaging". *Journal of Nuclear Medicine*, Vol. 44, No. 11, pp. 1855–1861, November 2003.

[Bart 11] H. Barthel, J. Luthardt, G. Becker, M. Patt, E. Hammerstein, K. Hartwig, B. Eggers, B. Sattler, A. Schildan, S. Hesse, P. M. Meyer, H. Wolf, T. Zimmermann, J. Reischl, B. Rohde, H. J. Gertz, C. Reininger, and O. Sabri. "Individualized quantification of brain β-amyloid burden: results of a proof of mechanism phase 0 florbetaben PET trial in patients with Alzheimer's disease and healthy controls". *European Journal of Nuclear Medicine and Molecular Imaging*, Vol. 38, No. 9, pp. 1702–1714, September 2011.

[Beck 13] G. A. Becker, M. Ichise, H. Barthel, J. Luthardt, M. Patt, A. Seese, M. Schultze-Mosgau, B. Rohde, H. J. Gertz, C. Reininger, and O. Sabri. "PET quantification of 18F-florbetaben binding to β-amyloid deposits in human brains". *Journal of Nuclear Medicine*, Vol. 54, No. 5, pp. 723–731, May 2013.

[Beet 94] G. Beets, F. Penninckx, C. Schiepers, L. Filez, L. Mortelmans, R. Kerremans, R. Aerts, and M. De Roo. "Clinical value of whole-body positron emission tomography with [18F]fluorodeoxyglucose". *British Journal of Surgery*, Vol. 81, No. 11, pp. 1666–1670, November 1994.

[Beng 97] F. M. Bengel, S. I. Ziegler, N. Avril, W. Weber, C. Laubenbacher, and M. Schwaiger. "Whole-body positron emission tomography in clinical oncology: comparison between attenuation-corrected and uncorrected images". *European Journal of Nuclear Medicine and Molecular Imaging*, Vol. 24, No. 9, pp. 1091–1098, September 1997.

[Berk 12] Y. Berker, J. Franke, A. Salomon, M. Palmowski, H. C. W. Donker, Y. Temur, F. M. Mottaghy, C. Kuhl, D. Izquierdo-Garcia, Z. A. Fayad, F. Kiessling, and V. Schulz. "MRI-based attenuation correction for hybrid PET/MRI systems: A 4-class tissue segmentation technique using a combined ultrashort-echo-time/Dixon MRI sequence". *Journal of Nuclear Medicine*, Vol. 53, No. 5, pp. 796–804, April 2012.

[Bern 04] M. A. Bernstein, K. F. King, and X. J. Zhou. *Handbook of MRI pulse sequences*. Elsevier Academic Press, Amsterdam, first Ed., 2004.

[Beye 00] T. Beyer, D. W. Townsend, T. Brun, P. E. Kinahan, M. Charron, R. Roddy, J. Jerin, J. Young, L. Byars, and R. Nutt. "A combined PET/CT scanner for clinical oncology". *Journal of Nuclear Medicine*, Vol. 41, No. 8, pp. 1369–1379, August 2000.

[Bezr 13] I. Bezrukov, H. Schmidt, F. Mantlik, N. Schwenzer, C. Brendle, B. Schölkopf, and B. J. Pichler. "MR-based attenuation correction methods for improved PET quantification in lesions within bone

and susceptibility artifact regions". *Journal of Nuclear Medicine*, Vol. 54, No. 10, pp. 1768–1774, October 2013.

[Blaf 12] T. Blaffert, S. Renisch, J. Tang, M. Narayanan, and Z. Hu. "Comparison of threshold-based and watershed-based segmentation for the truncation compensation of PET/MR images". In: *Progress in Biomedical Optics and Imaging - Proceedings of SPIE, San Diego, CA, USA*, pp. 1–12, August 2012.

[Blum 12] J. O. Blumhagen. "Going beyond the Borders : Field-of-View Extension in MR / PET Hybrid Imaging". *PhD Thesis, University of Basel, Faculty of Science*, 2012.

[Bott 84] P. A. Bottomley, T. H. Foster, R. E. Argersinger, and L. M. Pfeifer. "A review of normal tissue NMR relaxation times and relaxation mechanisms from 1 to 100 MHz: dependence on tissue type, NMR frequency, temperature, species, excision, and age". *Medical Physics*, Vol. 11, No. 4, pp. 425–448, July-August 1984.

[Brad 09] W. Bradley. "MR-guided focused ultrasound: a potentially disruptive technology". *Journal of the American College of Radiology*, Vol. 6, No. 7, pp. 510–513, July 2009.

[Brau 12] H. Braun, S. Ziegler, D. H. Paulus, and H. H. Quick. "Hybrid PET/MRI imaging with continuous table motion". *Medical Physics*, Vol. 39, No. 5, pp. 2735–2745, May 2012.

[Brow 03] M. A. Brown and R. C. Semelka. *MRI: Basic Principles and Applications*. Wiley-Liss, New Jersey, third Ed., 2003.

[Buck 08] A. K. Buck, S. Nekolla, S. Ziegler, A. Beer, B. J. Krause, K. Herrmann, K. Scheidhauer, H.-J. Wester, E. J. Rummeny, M. Schwaiger, and A. Drzezga. "SPECT/CT". *Journal of Nuclear Medicine*, Vol. 49, No. 8, pp. 1305–1319, August 2008.

[Burg 02] C. Burger, G. Goerres, S. Schoenes, A. Buck, H. Lonn, A, and G. K. Von Schulthess. "PET attenuation coefficients from CT images: experimental evaluation of the transformation of CT into PET 511-keV attenuation coefficients". *European Jounal of Nuclear Medicine and Molecular Imaging*, Vol. 29, No. 7, pp. 922–927, July 2002.

[Bush 02] J. T. Bushberg, J. A. Seibert, E. M. Jr Leidholdt, and J. M. Boone. *The Essential Physics of Medical Imaging*. Lippincott Williams & Wilkins, second Ed., 2002.

[Butt 30] S. Butterworth. "On the Theory of Filter Amplifiers". *Experimental Wireless*, Vol. 7, No. 6, pp. 536–541, October 1930.

[Cata 06] C. Catana, Y. Wu, M. S. Judenhofer, J. Qi, B. J. Pichler, and S. R. Cherry. "Simultaneous acquisition of multislice PET and MR images: initial results with a MR-compatible PET scanner". *Journal of Nuclear Medicine*, Vol. 47, No. 12, pp. 1968–1976, December 2006.

[Cata 10] C. Catana, A. van der Kouwe, T. Benner, C. J. Michel, M. Hamm, M. Fenchel, B. Fischl, B. Rosen, M. Schmand, and A. G. Sorensen. "Toward implementing an MRI-based PET attenuation-correction method for neurologic studies on the MR-PET brain prototype". *Journal of Nuclear Medicine*, Vol. 51, No. 9, pp. 1431–1438, September 2010.

[Cata 12] C. Catana, A. Drzezga, W. D. Heiss, and B. R. Rosen. "PET/MRI for neurologic applications". *Journal of Nuclear Medicine*, Vol. 53, No. 12, pp. 1916–1925, December 2012.

[Chan 01] W. L. Chan, J. Freund, N. A. Pocock, E. Szeto, F. Chan, B. J. Sorensen, and B. McBride. "Coincidence detection FDG PET in the management of oncological patients: attenuation correction versus non-attenuation correction". *Nuclear Medicine Communications*, Vol. 22, No. 11, pp. 1185–1192, September 2001.

[Chan 11] C.-C. Chang and C.-J. Lin. "LIBSVM : A Library for Support Vector Machines". *ACM Transactions on Intelligent Systems and Technology*, Vol. 2, No. 3, pp. 1–27, April 2011.

[Cher 06] S. R. Cherry and M. Dahlbom. *PET: Physics, Instrumentation, and Scanners*. Springer, New York, first Ed., 2006.

[Dels 09] G. Delso and S. Ziegler. "PET/MRI system design". *European Jounal of Nuclear Medicine and Molecular Imaging*, Vol. 36, No. 1, pp. 86–92, March 2009.

[Dels 10] G. Delso, A. Martinez-Möller, R. A. Bundschuh, R. Ladebeck, Y. Candidus, D. Faul, and S. I. Ziegler. "Evaluation of the attenuation properties of MR equipment for its use in a whole-body PET/MR scanner". *Physics in Medicine and Biology*, Vol. 55, No. 15, pp. 4361–4374, August 2010.

[Dels 11] G. Delso, S. Fürst, B. Jakoby, R. Ladebeck, C. Ganter, S. G. Nekolla, M. Schwaiger, and S. I. Ziegler. "Performance measurements of the Siemens mMR integrated whole-body PET/MR scanner". *Journal of Nuclear Medicine*, Vol. 52, No. 12, pp. 1914–1922, December 2011.

[Dixo 84] W. T. Dixon. "Simple proton spectroscopic imaging". *Radiology*, Vol. 153, No. 1, pp. 189–194, October 1984.

[Drze 12] A. Drzezga, M. Souvatzoglou, M. Eiber, A. J. Beer, S. Fürst, A. Martinez-Möller, S. G. Nekolla, S. Ziegler, C. Ganter, E. J. Rummeny, and M. Schwaiger. "First clinical experience with integrated whole-body PET/MR: comparison to PET/CT in patients with oncologic diagnoses". *Journal of Nuclear Medicine*, Vol. 53, No. 6, pp. 845–855, June 2012.

[Du 11] J. Du, M. Bydder, A. M. Takahashi, M. Carl, C. B. Chung, and G. M. Bydder. "Short T2 contrast with three-dimensional ultrashort echo time imaging". *Magnetic Resonance Imaging*, Vol. 29, No. 4, pp. 470–482, May 2011.

[Duka 11] J. Dukart, K. Mueller, A. Horstmann, H. Barthel, H. E. Möller, A. Villringer, O. Sabri, and M. L. Schroeter. "Combined evaluation of FDG-PET and MRI improves detection and differentiation of dementia". *PLoS One*, Vol. 6, No. 3, p. e18111, March 2011.

[Eibe 11] M. Eiber, A. Martinez-Möller, M. Souvatzoglou, K. Holzapfel, A. Pickhard, D. Löffelbein, I. Santi, E. J. Rummeny, S. Ziegler, M. Schwaiger, S. G. Nekolla, and A. J. Beer. "Value of a Dixon-based MR/PET attenuation correction sequence for the localization and evaluation of PET-positive lesions". *European Jounal of Nuclear Medicine and Molecular Imaging*, Vol. 38, No. 9, pp. 1691–1701, September 2011.

[Even 09] E. Even-Sapir, Z. Keidar, and B.-S. R. "Hybrid imaging (SPECT/CT and PET/CT)-improving the diagnostic accuracy of functional/metabolic and anatomic imaging". *Seminars in Nuclear Medicine*, Vol. 39, No. 4, pp. 264–275, July 2009.

[Fei 12] B. Fei, X. Yang, J. A. Nye, J. N. Aarsvold, N. Raghunath, M. Cervo, R. Stark, C. C. Meltzer, and J. R. Votaw. "MR/PET quantification tools: registration, segmentation, classification, and MR-based attenuation correction". *Medical Physics*, Vol. 39, No. 10, pp. 6443–6454, October 2012.

[Fisc 09] B. Fischer, U. Lassen, J. Mortensen, S. Larsen, A. Loft, A. Bertelsen, J. Ravn, P. Clementsen, A. Høgholm, K. Larsen, T. Rasmussen, S. Keiding, A. Dirksen, O. Gerke, B. Skov, I. Steffensen, H. Hansen, P. Vilmann, G. Jacobsen, V. Backer, N. Maltbaek, J. Pedersen, H. Madsen, H. Nielsen, and L. Højgaard. "Preoperative staging of lung cancer with combined PET-CT". *The New England Journal of Medicine*, Vol. 361, No. 1, pp. 32–39, July 2009.

[Fris 13] S. Frisch, J. Dukart, B. Vogt, A. Horstmann, G. Becker, A. Villringer, H. Barthel, O. Sabri, K. Müller, and M. L. Schroeter. "Dissociating memory networks in early Alzheimer's disease and frontotemporal lobar degeneration - a combined study of hypometabolism and atrophy". *PLoS One*, Vol. 8, No. 2, p. e55251, 2013.

[Fuku 90] K. Fukunage. *Introduction to Statistical Pattern Recognition.* Boston: Academic Press, second Ed., 1990.

[Gari 13] V. Garibotto, S. Heinzer, S. Vulliemoz, R. Guignard, M. Wissmeyer, M. Seeck, K.-O. Lovblad, H. Zaidi, O. Ratib, and M.-I. Vargas. "Clinical Applications of Hybrid PET/MRI in Neuroimaging". *Clinical Nuclear Medicine*, Vol. 38, No. 1, pp. 13–18, January 2013.

[Grit 93] L. S. Gritters, I. R. Francis, K. R. Zasadny, and R. L. Wahl. "Initial assessment of positron emission tomography using 2-fluorine-18-fluoro-2-deoxy-D-glucose in the imaging of malignant melanoma". *Journal of Nuclear Medicine*, Vol. 34, No. 9, pp. 1420–1427, September 1993.

[Grod 12] D. M. Grodzki, P. M. Jakob, and B. Heismann. "Ultrashort echo time imaging using pointwise encoding time reduction with radial acquisition (PETRA)". *Magnetic Resonance in Medicine*, Vol. 67, No. 2, pp. 510–518, February 2012.

[Hama 10] M. J. Hamamura, S. Ha, W. W. Roeck, L. T. Muftuler, D. J. Wagenaar, D. Meier, B. E. Patt, and O. Nalcioglu. "Development of an MR-compatible SPECT system (MRSPECT) for simultaneous data acquisition". *Physics in Medicine and Biology*, Vol. 55, No. 6, pp. 1563–1575, March 2010.

[Hofm 08] M. Hofmann, F. Steinke, V. Scheel, G. Charpiat, J. Farquhar, P. Aschoff, M. Brady, B. Schölkopf, and B. J. Pichler. "MRI-based attenuation correction for PET/MRI: a novel approach combining pattern recognition and atlas registration". *Journal of Nuclear Medicine*, Vol. 49, No. 11, pp. 1875–1883, November 2008.

[Hofm 09] M. Hofmann, B. Pichler, B. Schölkopf, and T. Beyer. "Towards quantitative PET/MRI: a review of MR-based attenuation correction techniques". *European Jounal of Nuclear Medicine and Molecular Imaging*, Vol. 36, Suppl. 1, pp. 93–104, March 2009.

[Hofm 11] M. Hofmann, I. Bezrukov, F. Mantlik, P. Aschoff, F. Steinke, T. Beyer, B. J. Pichler, and B. Schölkopf. "MRI-based attenuation correction for whole-body PET/MRI: quantitative evaluation of segmentation and atlas-based methods". *Journal of Nuclear Medicine*, Vol. 52, No. 9, pp. 1392–1399, September 2011.

[Hous 09] M. Houseni, W. Chamroonrat, S. Basu, G. Bural, A. Mavi, R. Kumar, and A. Alavi. "Usefulness of non attenuation corrected 18F-FDG-PET images for optimal assessment of disease activity in patients with lymphoma". *Hellenic Journal of Nuclear Medicine*, Vol. 12, No. 1, pp. 5–9, March 2009.

[Hu 10] Z. Hu, S. Renisch, B. Schweizer, T. Blaffert, N. Ojha, T. Guo, J. Tang, C. Tung, J. Kaste, V. Schulz, I. Torres, and L. Shao.

"MR-based attenuation correction for whole-body PET/MR system". *IEEE Nuclear Science Symposuim & Medical Imaging Conference*, pp. 2119–2122, Knoxville, Tennessee, USA, October 2010.

[Huds 94] H. M. Hudson and R. S. Larkin. "Ordered Subsets of Projection Data". *IEEE Transactions on Medical Imaging*, Vol. 13, No. 4, pp. 601–609, December 1994.

[Iban 05] L. Ibanez, W. Schroeder, L. Ng, and J. Cates. *The ITK Software Guide*. Kitware, Inc., http://www.itk.org/ItkSoftwareGuide.pdf, second Ed., 2005.

[Joha 11] A. Johansson, M. Karlsson, and T. Nyholm. "CT substitute derived from MRI sequences with ultrashort echo time". *Medical Physics*, Vol. 38, No. 5, pp. 2708–2714, May 2011.

[Joha 12] A. Johansson and M. Karlsson. "Voxel-wise uncertainty in CT substitute derived from MRI". *Medical Physics*, Vol. 39, No. 6, pp. 3283–3290, June 2012.

[Jude 08] M. S. Judenhofer, H. F. Wehrl, D. F. Newport, C. Catana, S. B. Siegel, M. Becker, A. Thielscher, M. Kneilling, M. P. Lichy, M. Eichner, K. Klingel, G. Reischl, S. Widmaier, M. Röcken, R. E. Nutt, H.-J. Machulla, K. Uludag, S. R. Cherry, C. D. Claussen, and B. J. Pichler. "Simultaneous PET-MRI: a new approach for functional and morphological imaging". *Nature Medicine*, Vol. 14, No. 4, pp. 459–465, April 2008.

[Jude 13] M. S. Judenhofer and S. R. Cherry. "Applications for Preclinical PET/MRI". *Seminars in Nuclear Medicine*, Vol. 43, No. 1, pp. 19–29, January 2013.

[Kale 13] A. Kalemis, B. M. A. Delattre, and S. Heinzer. "Sequential whole-body PET/MR scanner: concept, clinical use, and optimisation after two ears in the clinic. The manufacturer's perspective". *Magnetic Resonance Materials in Physics, Biology and Medicine*, Vol. 26, No. 1, pp. 5–23, February 2013.

[Kame 02] E. Kamel, T. Hany, C. Burger, V. Treyer, A. Lonn, G. von Schulthess, and A. Buck. "CT vs 68 Ge attenuation correction in a combined PET/CT system: evaluation of the effect of lowering the CT tube current". *European Journal of Nuclear Medicine and Molecular Imaging*, Vol. 29, No. 3, pp. 346–350, March 2002.

[Kapo 04] V. Kapoor, B. M. McCook, and F. S. Torok. "An introduction to PET-CT imaging". *Radiographics*, Vol. 24, No. 2, pp. 523–543, 2004.

[Karp 91] J. Karp, M. Daube-Witherspoon, E. Hoffman, T. Lewellen, J. Links, W. Wong, R. Hichwa, M. Casey, J. Colsher, and R. Hitchens. "Performance standards in positron emission tomography". *Journal of Nuclear Medicine*, Vol. 32, No. 12, pp. 2342–2350, December 1991.

[Kart 13] R. Kartmann, D. Paulus, H. Braun, B. Aklan, S. Ziegler, B. Navalpakkam, M. Lentschig, and H. Quick. "Integrated PET/MR imaging: Automatic attenuation correction of flexible RF coils". *Medical Physics*, Vol. 40, No. 8, p. 082301, August 2013.

[Keer 10] V. Keereman, Y. Fierens, T. Broux, Y. De Deene, M. Lonneux, and S. Vandenberghe. "MRI-based attenuation correction for PET/MRI using ultrashort echo time sequences". *Journal of Nuclear Medicine*, Vol. 51, No. 5, pp. 812–818, May 2010.

[Keer 11] V. Keereman, R. V. Holen, P. Mollet, and S. Vandenberghe. "The effect of errors in segmented attenuation maps on PET quantification". *Medical Physics*, Vol. 38, No. 11, pp. 6010–6019, November 2011.

[Kina 03] P. E. Kinahan, B. H. Hasegawa, and T. Beyer. "X-ray-based attenuation correction for positron emission tomography/computed tomography scanners". *Seminars in Nuclear Medicine*, Vol. 33, No. 3, pp. 166–179, July 2003.

[Kina 98] P. E. Kinahan, D. W. Townsend, T. Beyer, and D. Sashin. "Attenuation correction for a combined 3D PET / CT scanner". *Medical Physics*, Vol. 25, No. 10, pp. 2046–2053, October 1998.

[Klei 10] S. Klein, M. Staring, K. Murphy, M. Viergever, and J. Pluim. "elastix: a toolbox for intensity based medical image registration". *IEEE Transactions on Medical Imaging*, Vol. 29, No. 1, pp. 196–205, January 2010.

[Lade 13] C. Ladefoged, F. Andersen, S. Keller, J. Löfgren, A. Hansen, S. Holm, L. Højgaard, and T. Beyer. "PET/MR imaging of the pelvis in the presence of endoprostheses: reducing image artifacts and increasing accuracy through inpainting". *European Jounal of Nuclear Medicine and Molecular Imaging*, Vol. 40, No. 4, pp. 594–601, April 2013.

[Lang 84] K. Lange and R. Carson. "EM reconstruction algorithms for emission and transmission tomography". *Journal of Computer Assisted Tomography*, Vol. 8, No. 2, pp. 306–316, April 1984.

[Lars 13] A. Larsson, A. Johansson, J. Axelsson, T. Nyholm, T. Asklund, K. Riklund, and M. Karlsson. "Evaluation of an attenuation correction method for PET/MR imaging of the head based on substitute CT images". *Magnetic Resonance Materials in Physics, Biology and Medicine*, Vol. 26, No. 1, pp. 127–136, February 2013.

[Ma 03] J. Ma, J. Theiler, and S. Perkins. "Accurate On-line Support Vector Regression". *Neural Computation*, Vol. 15, No. 11, pp. 2683–2703, November 2003.

[MacD 11] L. R. MacDonald, S. Kohlmyer, C. Liu, T. K. Lewellen, and P. E. Kinahan. "Effects of MR surface coils on PET quantification". *Medical Physics*, Vol. 38, No. 6, pp. 2948–2956, June 2011.

[Macq 67] J. B. Macqueen. "Some Methods for classification and analysis of multivariate observations". In: *Procedings of the Fifth Berkeley Symposium on Math, Statistics, and Probability*, pp. 281–297, University of California Press, 1967.

[Malo 11] I. B. Malone, R. E. Ansorge, G. B. Williams, P. J. Nestor, T. A. Carpenter, and T. D. Fryer. "Attenuation correction methods suitable for brain imaging with a PET/MRI scanner: a comparison of tissue atlas and template attenuation map approaches". *Journal of Nuclear Medicine*, Vol. 52, No. 7, pp. 1142–1149, July 2011.

[Mant 11] F. Mantlik, M. Hofmann, M. K. Werner, A. Sauter, J. Kupferschläger, B. Schölkopf, B. J. Pichler, and T. Beyer. "The effect of patient positioning aids on PET quantification in PET/MR imaging". *European Jounal of Nuclear Medicine and Molecular Imaging*, Vol. 38, No. 5, pp. 920–929, May 2011.

[Mart 09] A. Martinez-Möller, M. Souvatzoglou, G. Delso, R. A. Bundschuh, C. Chefd'hotel, S. I. Ziegler, N. Navab, M. Schwaiger, and S. G. Nekolla. "Tissue classification as a potential approach for attenuation correction in whole-body PET/MRI: evaluation with PET/CT data". *Journal of Nuclear Medicine*, Vol. 50, No. 4, pp. 520–526, April 2009.

[Naka 02] Y. Nakamoto, M. Osman, C. Cohade, L. T. Marshall, J. M. Links, S. Kohlmyer, and R. L. Wahl. "PET/CT: comparison of quantitative tracer uptake between germanium and CT transmission attenuation-corrected images". *Journal of Nuclear Medicine*, Vol. 43, No. 9, pp. 1137–1143, September 2002.

[Nava 12a] B. K. Navalpakkam, H. Braun, J. Hornegger, T. Kuwert, and H. H. Quick. "MR-based attenuation correction for PET/MRI hybrid imaging continuous valued attenuation maps". In: *Molekulare Bildgebung 2012, Erlangen*, September 2012.

[Nava 12b] B. K. Navalpakkam, H. Braun, S. Ziegler, J. Hornegger, H. H. Quick, and T. Kuwert. "Simultaneous PET/MR Hybrid Imaging: MR based continuous valued attenuation map generation and its effect on quantitative PET imaging". In: *International Society for Magnetic Resonance in Medicine, Melbourne*, p. 2717, May 2012.

[Nava 12c] B. K. Navalpakkam, M. Cachovan, H. H. Quick, J. Hornegger, and T. Kuwert. "MR Based Attenuation Correction for SPECT". In: *Nuclear Science Symposium and Medical Imaging Conference, Anaheim, USA*, pp. M15–19, November 2012.

[Nava 13a] B. K. Navalpakkam, H. Braun, J. Hornegger, T. Kuwert, and H. H. Quick. "MR based attenuation correction including cortical bone for PET/MR hybrid imaging". In: *PSMR 2013/4th Jülich MR-PET Workshop, Aachen*, May 2013.

[Nava 13b] B. K. Navalpakkam, H. Braun, J. Hornegger, T. Kuwert, and H. H. Quick. "MR-Based Attenuation Correction Including Cortical Bone for PET/MR Hybrid Imaging". In: *International Society for Magnetic Resonance in Medicine, Salt Lake City*, p. 2815, April 2013.

[Nava 13c] B. K. Navalpakkam, H. Braun, T. Kuwert, and H. H. Quick. "Magnetic resonance-based attenuation correction for PET/MR hybrid imaging using continuous valued attenuation maps". *Investigative Radiology*, Vol. 48, No. 5, pp. 323–332, May 2013.

[Nuyt 13] J. Nuyts, G. Bal, F. Kehren, M. Fenchel, C. Michel, and C. Watson. "Completion of a truncated attenuation image from the attenuated PET emission data". *IEEE Transactions on Medical Imaging*, Vol. 32, No. 2, pp. 237–246, February 2013.

[Otsu 79] N. Otsu. "A threshold selection method from grey level histograms". *IEEE Transactions on Systems, Man, and Cybernetics*, Vol. 9, No. 1, pp. 62–66, January 1979.

[Ott 06] K. Ott, W. Weber, and J. Siewert. "The importance of PET in the diagnosis and response evaluation of esophageal cancer". *Diseases of the Esophagus*, Vol. 19, No. 6, pp. 433–442, January 2006.

[Pal 09] D. Pal, N. Ojha, T. Guo, G. Muswick, and J. Kaste. "Attenuation correction for MR table and coils for a sequential PET/MR system". *IEEE Nuclear Science Symposium Conference Record (NSS/MIC)*, pp. 3303–3306, October 2009.

[Paul 11] D. H. Paulus, H. Braun, B. Aklan, and H. H. Quick. "Simultaneous PET / MR Hybrid Imaging: MR-based Attenuation Correction of Flexible Radiofrequency Surface Coils". *Medical Physics*, Vol. 39, No. 7, pp. 4306–4315, July 2011.

[Pich 06] B. J. Pichler, M. S. Judenhofer, C. Catana, J. H. Walton, M. Kneilling, R. E. Nutt, S. B. Siegel, C. D. Claussen, and S. R. Cherry. "Performance test of an LSO-APD detector in a 7-T MRI scanner for simultaneous PET/MRI". *Journal of Nuclear Medicine*, Vol. 47, No. 4, pp. 639–647, April 2006.

[Pich 08] B. J. Pichler, H. F. Wehrl, A. Kolb, and M. S. Judenhofer. "Positron emission tomography/magnetic resonance imaging: the next generation of multimodality imaging?". *Seminars in Nuclear Medicine*, Vol. 38, No. 3, pp. 199–208, May 2008.

[Pich 10] B. J. Pichler, A. Kolb, T. Nägele, and H.-P. Schlemmer. "PET/MRI: paving the way for the next generation of clinical multimodality imaging applications". *Journal of Nuclear Medicine*, Vol. 51, No. 3, pp. 333–336, March 2010.

[Quic 11] H. H. Quick, R. Ladebeck, and J.-C. Georgi. "Whole-Body MR/PET Hybrid Imaging: Technical Considerations, Clinical Workflow, and Initial Results". *Magnetom Flash*, Vol. 46, No. 1, pp. 88–100, 2011.

[Quic 13] H. H. Quick, C. von Gall, M. Zeilinger, M. Wiesmüller, H. Braun, S. Ziegler, T. Kuwert, M. Uder, A. Dörfler, W. A. Kalender, and M. Lell. "Integrated whole-body PET/MR hybrid imaging: clinical experience". *Investigative Radiology*, Vol. 48, No. 5, pp. 280–289, May 2013.

[Rahm 06] J. Rahmer, P. Boernert, J. Groen, and C. Bos. "Three-dimensional Radial Ultrashort Echo-time Imaging With T2 Adapted Sampling". *Magnetic Resonance in Medicine*, Vol. 55, No. 5, pp. 1075–1082, May 2006.

[Rank 13] C. M. Rank, C. Tremmel, N. Hünemohr, A. M. Nagel, O. Jäkel, and S. Greilich. "MRI-based treatment plan simulation and adaptation for ion radiotherapy using a classification-based approach". *Radiation Oncology*, Vol. 8, No. 51, pp. 1–13, March 2013.

[Robs 03] M. D. Robson, P. D. Gatehouse, M. Bydder, and G. M. Bydder. "Magnetic resonance: an introduction to ultrashort TE (UTE) imaging". *Journal of Computer Assisted Tomography*, Vol. 27, No. 6, pp. 825–846, November/December 2003.

[Salo 11] A. Salomon, A. Goedicke, B. Schweizer, T. Aach, and V. Schulz. "Simultaneous reconstruction of activity and attenuation for PET/MR". *IEEE Transactions on Medical Imaging*, Vol. 30, No. 3, pp. 804–813, March 2011.

[Sama 12] A. Samarin, C. Burger, S. D. Wollenweber, D. W. Crook, I. A. Burger, D. T. Schmid, G. K. V. Schulthess, and F. P. Kuhn. "PET / MR imaging of bone lesions - implications for PET quantification from imperfect attenuation correction". *European Jounal of Nuclear Medicine and Molecular Imaging*, Vol. 39, No. 7, pp. 1154–1160, July 2012.

[Schr 10] E. Schreibmann, J. A. Nye, D. M. Schuster, D. R. Martin, J. Votaw, and T. Fox. "MR-based attenuation correction for hybrid PET-MR brain imaging systems using deformable image

registration". *Medical Physics*, Vol. 37, No. 5, pp. 2101–2109, May 2010.

[Schr 13] G. Schramm, J. Langner, F. Hofheinz, J. Petr, B. Beuthien-Baumann, I. Platzek, J. Steinbach, J. Kotzerke, and J. van den Hoff. "Quantitative accuracy of attenuation correction in the Philips Ingenuity TF whole-body PET/MR system: a direct comparison with transmission-based attenuation correction". *Magnetic Resonance Materials in Physics, Biology and Medicine*, Vol. 26, No. 1, pp. 115–126, February 2013.

[Schu 11] V. Schulz, I. Torres-Espallardo, S. Renisch, Z. Hu, N. Ojha, P. Börnert, M. Perkuhn, T. Niendorf, W. M. Schäfer, H. Brockmann, T. Krohn, A. Buhl, R. W. Günther, F. M. Mottaghy, and G. A. Krombach. "Automatic, three-segment, MR-based attenuation correction for whole-body PET/MR data". *European Jounal of Nuclear Medicine and Molecular Imaging*, Vol. 38, No. 1, pp. 138–152, January 2011.

[Shao 97a] Y. Shao, S. R. Cherry, K. Farahani, K. Meadors, S. Siegel, R. W. Silverman, and P. K. Marsden. "Simultaneous PET and MR imaging". *Physics in Medicine and Biology*, Vol. 42, No. 10, pp. 1965–1970, October 1997.

[Shao 97b] Y. Shao, S. R. Cherry, K. Farahmi, R. Slates, R. W. Silverman, S. Member, K. Meadors, A. Bowery, S. Siegel, P. K. Marsden, and P. B. Garlick. "Development of a PET Detector System Compatible with MRI / NMR Systems". *IEEE Transactions on Nuclear Science*, Vol. 44, No. 3, pp. 1167–1171, June 1997.

[Shep 74] L. Shepp and B. Logan. "The Fourier reconstruction of a head section". *IEEE Transactions on Nuclear Science*, Vol. 21, No. 2, pp. 21–43, June 1974.

[Shep 82] L. Shepp and Y. Vardi. "Maximum likelihood reconstruction for emission tomography". *IEEE Transactions on Medical Imaging*, Vol. 1, No. 2, pp. 113–122, October 1982.

[Shig 05] A. Shigeo. *Support Vector Machines for Pattern Classification*. Springer-Verlag, London, first Ed., 2005.

[Smol 04] A. J. Smola and B. Schölkopf. "A tutorial on support vector regression". *Statistics and Computing*, Vol. 14, No. 3, pp. 199–222, August 2004.

[Stei 10] J. Steinberg, G. Jia, S. Sammet, J. Zhang, N. Hall, and M. V. Knopp. "Three-region MRI-based whole-body attenuation correction for automated PET reconstruction". *Nuclear Medicine and Biology*, Vol. 37, No. 2, pp. 227–235, February 2010.

[Tell 11] L. Tellmann, H. H. Quick, A. Bockisch, H. Herzog, and T. Beyer. "The effect of MR surface coils on PET quantification in whole-body PET/MR: Results from a pseudo-PET/MR phantom study". *Medical Physics*, Vol. 38, No. 5, pp. 2795–2805, May 2011.

[Vapn 98] V. N. Vapnik. *Statistical Learning Theory*. Wiley-Interscience, first Ed., October 1998.

[Viol 01] P. Viola and M. Jones. "Rapid object detection using a boosted cascade of simple features". In: *Proceedings of the 2001 IEEE Computer Society Conference on Computer Vision and Pattern Recognition*, pp. 511–518, IEEE, Kauai, USA, 2001.

[Wern 03] M. N. Wernick and J. N. Aarsvold. *Emission Tomography: The Fundamental of PET and SPECT*. Academic Press, first Ed., 2003.

[Wett 13] A. Wetter, C. Lipponer, F. Nensa, K. Beiderwellen, T. Olbricht, H. Rübben, A. Bockisch, T. Schlosser, T. a. Heusner, and T. C. Lauenstein. "Simultaneous 18F choline positron emission tomography/magnetic resonance imaging of the prostate: initial results". *Investigative Radiology*, Vol. 48, No. 5, pp. 256–262, May 2013.

[Wies 13] M. Wiesmüller, H. H. Quick, B. K. Navalpakkam, M. M. Lell, M. Uder, P. Ritt, D. Schmidt, M. Beck, T. Kuwert, and C. C. von Gall. "Comparison of lesion detection and quantitation of tracer uptake between PET from a simultaneously acquiring whole-body PET/MR hybrid scanner and PET from PET/CT". *European Jounal of Nuclear Medicine and Molecular Imaging*, Vol. 40, No. 1, pp. 12–21, January 2013.

[Wu 04] T.-H. Wu, Y.-H. Huang, J. J. S. Lee, S.-Y. Wang, S.-C. Wang, C.-T. Su, L.-K. Chen, and T.-C. Chu. "Radiation exposure during transmission measurements: comparison between CT- and germanium-based techniques with a current PET scanner". *European Jounal of Nuclear Medicine and Molecular Imaging*, Vol. 31, No. 1, pp. 38–43, January 2004.

[Zaid 03] H. Zaidi, M.-L. Montandon, and D. O. Slosman. "Magnetic resonance imaging-guided attenuation and scatter corrections in three-dimensional brain positron emission tomography". *Medical Physics*, Vol. 30, No. 5, pp. 937–948, May 2003.

[Zaid 11] H. Zaidi and A. Del Guerra. "An outlook on future design of hybrid PET/MRI systems". *Medical Physics*, Vol. 38, No. 10, pp. 5667–5689, October 2011.